**Charles University**

**Faculty of Science**

**Dissertation**

**2021** **Qiudi Yue**

**Charles University**

**Faculty of Science**

Study program: Physical chemistry

**MSc. Qiudi Yue**

# Labile elementosilicates as intermediates for design of novel materials

Doctoral thesis

Supervisor: Dr. Maksym Opanasenko

Advisor: Prof. Ing. Jiří Čejka, DrSc

Prague, 2021

**Univerzita Karlova**

**Přírodovědecká fakulta**

Studijní program: Fyzikální chemie

**MSc. Qiudi Yue**

# Labilní elementosilikáty jako meziprodukty pro přípravu nových materiálů

Disertační práce

Školitel: Dr. Maksym Opanasenko

Konzultant: Prof. Ing. Jiří Čejka, DrSc.

Praha, 2021

**Prohlášení**:

Dizertační práci jsem vypracoval na Přírodovědecké fakultě, Univerzity Karlovy.

Prohlašuji, že jsem závěrečnou práci zpracovala samostatně a že jsem uvedla všechny použité informační zdroje a literaturu. Tato práce ani její podstatná část nebyla předložena k získání jiného nebo stejného akademického titulu.

V Praze, 31.05.2021

Podpis ----------

# Acknowledgement

Tiefo → Mianyang → Chengdu → Hefei → Prague, it took 24 years. It is a great journey, not easy but deserved.

First of all, I would like to thank Prof. Jiří Čejka for giving me this opportunity to work in this great group to complete my PhD study. I am grateful for his advices and support in my work.

I would like to acknowledge my supervisor, Dr. Maksym Opanasenko, for his invaluable advices and support in these four years. He gives me enough freedom to explore the science in the way I like. His brilliant ideas inspire me, and correct me in the right time. It is very pleasant to work with him.

I would like to thank my colleagues and also collaborators in the lab for characterizing the samples, Dr. Michal Mazur and Ang Li for TEM measurement, Dr. Martin Kubů for gas adsorption/desorption and ICP-OES measurements, Dr. Mariya Shamzhy for FTIR, Jin Zhang for FTIR, NMR, UV-vis measurement and also the help with sample preparation, Dr. Yong Zhou for the help in the zeolites synthesis and insightful discussion. I would like to thank other members in our group for their kind assistance and support, Mgr. Milan Eliáš, Yuyan Zhang, Dr. Jan Přech, Dr. Valeryia Kasneryk, Dr. Mohamed Infas Haja Mohideen, Dr. Rani Poonam, Dr. Roman Barakov, Ondřej Veselý, Sarra Abdi, Anastasia Kurbanova, Dr. Kinga Gołąbek, and Dr. Juan Francisco Miñambres Redondo. I also would like to send my acknowledgement to the secretaries of department, Anna Knězů, Zuzana Hrabalová, and Hana Kábová for their kind assistance.

I would like to acknowledge my collaborators for their great work, Prof. Russell E. Morris, Dr. Paul S. Wheatley, and Daniel N. Rainer at University of St Andrews for the XRD measurement and refinement, Prof. Roman Bulánek and Jakub Halamek at University of Pardubice for the study of gas separation, Prof. Ehrenfried Zschech and Kristina Kutukova at Fraunhofer IKTS for X-ray tomography study, Prof. Zhenlin Luo and Jingtian Zhou at University of Science and Technology of China for the synchrotron XRD study, Dr. Peter Minárik at Charles University for the help and technical support of FIB and SEM measurement. I also want to thank my other collaborators for their great efforts, although their works are not presented in this thesis, namely, Prof. Petr Nachtigall, Dr. Christopher J. Heard, Dr. Lukáš Grajciar, and Dianwei Hou at Charles University, Prof. Toru Wakihara at University of Tokyo, Dr. Zhehao Huang at Stockholm University, Dr. Dario Ferreira Sanchez

at Paul Scherrer Institut, Dr. Veronika Pashkova at J. Heyrovsky Institute of Physical Chemistry.

Finally, I would like to thank my family and all my friends for their encouragement and belief during the whole PhD study.

Thank you all for your invaluable support.

# List of publications

The dissertation was completed based on the following publications:

**Q. Yue**, J. Zhang, M. Shamzhy, M. Opanasenko*. Seeded growth of isomorphously substituted chabazites in proton-form. **Microporous Mesoporous Mater.** 2019, 280, 331-336. (Q1, IF = 4.55)

V. Kasneryk, M. Shamzhy, J. Zhou, **Q. Yue**, M. Mazur, A. Mayoral, Z. Luo*, R. E. Morris, J. Čejka, M. Opanasenko*. Vapour-phase-transport rearrangement technique for the synthesis of new zeolites. **Nat. Commun.** 2019, 10, 5129. (Q1, IF = 12.11)

**Q. Yue**, K. Kutukova, E. Zschech, A. Li, J. Čejka, M. Opanasenko*. Controllable zeolite AST crystallization mechanism: between the classical and reversed crystal growth. *Submitted, under revision in Nat. Commun.*

**Q. Yue**, J. Halamek, D. Rainer, J. Zhang, R. Bulánek, R. E. Morris, J. Čejka*, M. Opanasenko*. Tuning the CHA framework composition by isomorphous substitution for separation of $CO_2/CH_4$. *Submitted, under revision in Chem. Eng. J.*

**Q. Yue**, V. Kasneryk, M. Shamzhy, M. Mazur, Y. Zhou, R. E. Morris, P. Wheatley, J. Čejka, M. Opanasenko*. ADORable zeolite with 12×8×8-ring pores derived from IWR germanosilicate. *Submitted*

Further publications

J. Zhang, **Q. Yue**, M. Mazur, M. Opanasenko, M. Shamzhy, J. Čejka. Selective recovery and recycling of germanium for the design of sustainable zeolite catalysts. **ACS Sustain. Chem. Eng.** 2020, 8, 8235-8246. (Q1, IF = 7.63)

# Abbreviations

| | |
|---|---|
| 1D | one-dimensional |
| 2D | two-dimensional |
| 3D | three-dimensional |
| ADOR | assembly-disassembly-organization-reassembly |
| $AlPO_4$ | aluminophosphate |
| BET | surface area according to Brunauer, Emmett and Teller theory |
| CBUs | composite building units |
| *d4r* | double four ring |
| DBU | 1,8-diazabicyclo[5.4.0]undec-7-ene |
| DEDMAOH | diethyldimethylammonium hydroxide |
| DMADH | (6R,10S)-6,10-dimethyl-5-azoniaspiro[4.5]decane hydroxide |
| DMDH | decamethonium dihydroxide |
| DR UV-vis | diffuse reflection ultraviolet-visible spectroscopy |
| EDX | energy dispersive X-ray analysis |
| FIB | focused ion beam |
| FTIR | Fourier transmission infrared spectroscopy |
| HRTEM | high resolution transmission electron microscopy |
| HMDH | hexamethonium dihydroxide |
| IAST | ideal adsorbed solution theory |
| IZA | International Zeolite Association |
| MAS NMR | magic angle spinning nuclear magnetic resonance |
| $MPP(OH)_2$ | 1,5-bis-(methylpyrrolidinium)pentane dihydroxide |
| XCT | X-ray computed tomography |
| OSDA | organic structure-directing agent |
| *s4r* | single four ring |

| | |
|---|---|
| SAPO | silicoaluminophosphate |
| SBUs | secondary building units |
| SDA | structure-directing agent |
| SEM | scanning electron microscopy |
| Si/Al | molar ratio of silicon to aluminum |
| Si/Ge | molar ratio of silicon to germanium |
| TEOS | tetraethyl orthosilicate |
| TMAdaOH | trimethyladamantylammonium hydroxide |
| $V_{micro}$ | micropore volume |
| VPT | vapor phase transport |
| $Q_{st}$ | heat of adsorption |
| XRD | X-ray diffraction |

# Abstract

Zeolites are crystalline microporous materials with three-dimensional frameworks built from corner-sharing $TO_4$ tetrahedra. Traditionally, zeolites are defined as aluminosilicates (T = Si and Al). Nowadays, the skeleton atoms have been expanded to other tri-/tetra-valent elements, including B, Ga, Ge, Ti, etc., due to the chemical flexibility of zeolites. Resulting materials are termed as elementosilicates for respective element-containing zeolites. Such materials exhibit fascinating properties due to the different nature of elements in the framework, *e.g.* structural flexibility and tunable acidity. Taking advantage of the unique properties of elementosilicate zeolites, their applications as the starting solids for the synthesis of new materials and as adsorbents for gas separation have made great progress. However, the complexity of the factors affecting the zeolite synthesis limits the possibility to control the key parameters of zeolites formation, *e.g.* crystallization mechanism, crystal growth rate, and phase selectivity. From the another side, for particular zeolite systems being perspective for gas separation, correlation between the chemical composition of designed structures and their adsorption performance is elusive.

Considering the above statements, this thesis was focused on the design of a series of elementosilicate zeolites with tunable properties (in particular, morphology, porosity, or acidity) either through controlling the crystallization mechanism or by manipulation with the zeolite structure and chemical composition.

The main achievements of this thesis are as follows:

A truly reversed crystal growth mechanism, in which crystallization starts at the surface of amorphous aggregates and then proceeds towards their centers, is demonstrated in zeolite synthesis systems for the first time. Using the zeolite **AST** as a representative structure, it was established that the concentration of structure-directing agent (SDA) in reaction mixture determines the facilitation of particular crystallization mechanism as it is responsible for driving the agglomeration of small particles into large amorphous aggregates at very early stages of the synthesis before crystallization starts. At low $x = SDA/SiO_2$ ratio ($0.3 \leq x \leq 0.4$) the crystal growth follows the classical route, while at high values ($0.5 \leq x \leq 0.7$) it switches to the reversed crystal growth mechanism. Besides, the F ions were revealed to govern the rate of crystal growth: a higher concentration of $F^-$ results in a greater growth rate.

Two new zeolites (IPC-17 and IPC-18) were prepared using the ADOR (*assembly-disassembly-organization-reassembly*) approach by taking advantage of the structural lability

of particular building units in the germanosilicate zeolites. For the realization of successful structural transformation, different strategies were applied for respective germanosilicates possessing unique chemical/structural properties. For the preparation of IPC-17, optimization of ADOR synthetic strategy was carried out through the control of the chemical composition of starting germanosilicate **IWR**. For the synthesis of IPC-18, the suppression of mass transport in the interlayer space of the products of germanosilicate **IWW** zeolite transformation was the core idea of the newly developed vapor-phase-transport rearrangement technique.

Direct synthesis of isomorphously substituted M-CHA (M = B, Al, Ga, and Ti) zeolites free of metal cations at ion-exchange positions was developed utilizing the assistance of pure siliceous Si-CHA as the crystal growth seeds. The synthesis time for respective M-CHA zeolites was significantly reduced compared with the previously known protocols. The introduction of heteroatoms to the framework of **CHA** zeolite was confirmed by the solid-state MAS NMR, UV-vis, and FTIR spectroscopies. It was established that the change in heteroatoms' nature alters the geometry of 8-ring in **CHA** structures and also influences the zeolite-$CO_2$ host-guest interaction and thus the zeolite performance in $CO_2/CH_4$ separation. The overall separation ability of M-CHA zeolites was found to follow the order Ti-CHA < Si-CHA ≈ B-CHA < Ga-CHA < Al-CHA.

# Abstrakt

Zeolity jsou krystalické mikroporézní materiály s trojrozměrnými mřížkami vytvořenými z tetraedrů se sdílenými vrcholy. Zeolity jsou tradičně definovány jako hlinitokřemičitany (T = Si a Al). V dnešní době byly mřížkové atomy rozšířeny na další tri-/tetravalentní prvky, včetně B, Ga, Ge, Ti atd., vzhledem k chemické flexibilitě zeolitů. Výsledné materiály se označují jako elementosilikáty pro příslušné zeolity obsahující výše uvedené prvky. Tyto materiály vykazují fascinující vlastnosti díky odlišné povaze prvků ve struktuře, např. strukturální flexibilitě a nastavitelné kyselosti. Využití jedinečných vlastností elementosilikátových zeolitů, jejich použití jako výchozích pevných látek pro syntézu nových materiálů a jako adsorbentů pro separaci plynů učinilo velký pokrok. Složitost faktorů ovlivňujících syntézu zeolitu však omezuje možnost kontroly klíčových parametrů tvorby zeolitu, např. krystalizačního mechanismu, rychlosti růstu krystalů a fázové selektivity. Na druhou stranu, pro konkrétní zeolitové systémy, které jsou perspektivní pro separaci plynů, korelace mezi chemickým složením navržených struktur a jejich adsorpčními vlastnostmi je těžko postižitelná.

S ohledem na výše uvedená fakta, byla tato práce zaměřena na návrh řady elementosilikátových zeolitů s laditelnými vlastnostmi (zejména morfologie, poréznost nebo kyselost) buď prostřednictvím kontroly krystalizačního mechanismu nebo manipulací se zeolitovou strukturou a chemickým složením.

Hlavní přínosy této práce jsou:

Skutečně obrácený mechanismus růstu krystalů, v němž krystalizace začíná na povrchu amorfních agregátů a poté pokračuje směrem k jejich centrům, je poprvé demonstrován v systémech syntézy zeolitu. S využitím zeolitu **AST** jako reprezentativní struktury bylo zjištěno, že koncentrace strukturu-určujícího činidla (SDA) v reakční směsi určuje usnadnění konkrétního krystalizačního mechanismu, protože je zodpovědný za nasměrování aglomerace malých částic do velkých amorfních agregátů ve velmi raných fázích syntézy před zahájením krystalizace. Při nízkém poměru $x = SDA/SiO_2$ ($0.3 \leq x \leq 0.4$) růst krystalů následuje klasickou cestu, zatímco při vysokých hodnotách ($0.5 \leq x \leq 0.7$) přechází na obrácený mechanismus růstu krystalů. Kromě toho bylo zjištěno, že F ionty řídí rychlost růstu krystalů: vyšší koncentrace $F^-$ má za následek vyšší rychlost růstu.

Dva nové zeolity (IPC-17 a IPC-18) byly připraveny metodou ADOR (assembly-disassembly-organisation-reassembly) s využitím strukturní lability konkrétních „stavebních jednotek“ v

germanosilikátových zeolitech. Pro realizaci úspěšné strukturální transformace byly použity různé strategie pro příslušné germanosilikáty s speciálními chemicko-strukturními vlastnostmi. Pro přípravu IPC-17 byla provedena optimalizace syntetické strategie ADOR prostřednictvím kontroly chemického složení počátečního germanosilikátu **IWR**. Pro syntézu IPC-18 bylo použiti omezení přenosu hmoty v mezivrstvém prostoru produktu transformace germanosilikátového zeolitu **IWW**, což byla základní myšlenka nově vyvinuté přeskupovací techniky s využitím přenosu v plynné fázi.

Přímá syntéza izomorfně substituovaných M-CHA (M = B, Al, Ga a Ti) zeolitů bez kovových kationtů na iontových výměnných pozicích byla vyvinuty s využitím čistě křemičitého Si-CHA jako krystalizačních zárodků. Ve srovnání s dříve známými postupy byla doba syntézy příslušných zeolitů M-CHA významně zkrácena. Zavedení heteroatomů do mřížky zeolitu **CHA** bylo potvrzeno použitím MAS NMR v pevné fázi, UV-vis a FTIR spektroskopie. Bylo zjištěno, že změna charakteru heteroatomů mění geometrii 8-četného kruhového otvoru v pórech **CHA** a také ovlivňuje interakci typu „host-guest“ mezi zeolitem a $CO_2$, a tím i zeolitovou výkonnost při separaci $CO_2/CH_4$. Bylo zjištěno, že celková separační schopnost zeolitů M-CHA odpovídá pořadí Ti-CHA < Si-CHA ≈ B-CHA < Ga-CHA < Al-CHA.

# Content

# 1. Aim of study

Revealing the key parameters in the zeolite synthesis and understanding the unique chemical/structural properties of zeolite frameworks provides better insight into the control of crystal growth, new zeolite synthesis, and the development of particular zeolites for gas separation. This thesis focuses on the study of the fundamental parameters of the determination of zeolite crystallization pathway, the synthesis of novel zeolite structures through structural transformation, and the preparation of elementosilicate zeolites with tunable properties (i.e. morphology, porosity, and acidity) for gas separation.

This thesis aimed to achieve the following specific goals:

- To reveal a unique zeolite crystallization model of zeolite **AST**, that is, reversed crystal growth in which crystallization starts at the surface of amorphous aggregates and then proceeds towards their centers.
- To determine the fundamental function of SDA and F ions on the determination of the crystallization mechanism, and thus for the control of crystallization pathway between the classical and reversed crystal growth.
- To synthesize new zeolites through structural transformation of germanosilicate zeolites.
- To design synthetic strategies to stabilize labile germanosilicate **IWR** frameworks for the realization of successful topotactic transformation.
- To develop a new technique, i.e. vapor-phase-transport rearrangement, for the control of mass transport within the interlayer of germanosilicate **IWW** zeolite.
- To prepare elementosilicate **CHA** zeolites in a direct hydrothermal synthesis by the seeding method.
- To correlate the influence of heteroatoms of isomorphously substituted **CHA** zeolites with their gas separation performance.

# 2. Introduction

## 2.1 Zeolites: definition, preparation and application

### 2.1.1 Brief introduction of zeolites

Traditionally, zeolites are defined as crystalline microporous aluminosilicates with three-dimensional framework built from corner-sharing $TO_4$ (T = Si and Al) tetrahedra. Nowadays, diverse zeolite-related microporous materials (zeotypes) have been reported. The framework elements of microporous zeotypes have expanded to $T^{III}$ (B, Ga), $T^{IV}$ (Ti, Sn, Zr, Ge), and $T^{V}$ (P) elements.

Zeolites were firstly discovered as natural minerals in 1756 [1], which were considered without any practical interest. The discovery of new zeolites was almost exclusively studied by mineralogists who were more interested in understanding the environments and the crystallization conditions of these phases than in their practical uses [2]. At present, 67 types of natural zeolites have been discovered according to the International Zeolite Association (IZA) database. Hereafter, the characteristics of natural zeolites and their potential applications in the field of ion exchange and adsorption were studied in 1900s. One of the breakthroughs was the development of artificial zeolites with high Al content, which were hydrothermally synthesized in 1940s through simulating the geothermal formation conditions for natural zeolites [3]. Henceforward, a lot of new zeolites with different chemical compositions and framework types have been prepared as a result of the fast development of synthetic methods. For example, zeolites A and X were synthesized using low-temperature hydrothermal techniques and related patents were filed in 1949 [3].

### 2.1.2 Structure of zeolites and its description

Up to now, 253 types of zeolites or zeotypes have been verified by the IZA Structure Committee including silicates, germanosilicates, aluminophosphates (AlPOs), silicoaluminophosphates (SAPOs), borosilicates, and so on. Each zeolite framework has a corresponding three-letter code. Specially, in some cases, a minus (–) sign is used to indicate interrupted frameworks (*e.g.* **–ITV** or **–SVR**), and an asterisk (*) for disordered frameworks (*e.g.* ***BEA** or ***SFV**), but a combination is also possible (*e.g.* ***–SSO** or ***–EWT**). The code only describes and defines the framework types while it does not contain any information about chemical composition, T-atom distribution, or cell dimension, etc.

### 2.1.2.1 Primary building units

Each T-atom of zeolites is tetrahedrally coordinated to 4 oxygen atoms, thus each oxygen atom bridges 2 T atoms (Figure 2.1). Different connections of $TO_4$ tetrahedra result in diverse zeolite frameworks. This basic structural building unit ($TO_4$ tetrahedra) is defined as primary building unit.

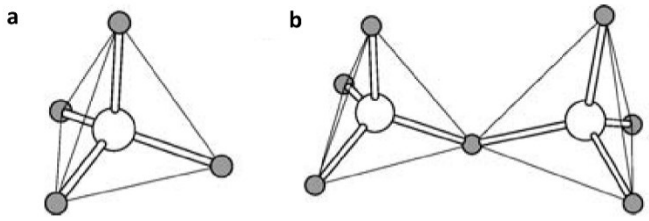


Figure 2.1 (**a**) $TO_4$ tetrahedron; (**b**) $TO_4$ tetrahedra bridged by oxygen vertex [4].

The aluminosilicate zeolite possesses an anionic framework because of the presence of $AlO_4$ tetrahedrons, and the negative charges are compensated by the extra-framework cations (*e.g.* $Li^+$, $Cs^+$, $K^+$, $NH_4^+$, $Na^+$, $Ca^{2+}$, etc.). Aluminophosphate is constructed by strict alternation of $AlO_4$ and $PO_4$ tetrahedra, thus its framework is electro neutral with no extra metal cations presented.

Diversity of connectivity of tetrahedra results in unique pore architecture of zeolites, i.e., pore size, pore volume, and pore topology. According to the number of T atoms limiting the pore entrance, zeolites are classified as small (8-ring); medium (10-ring); large (12-ring) and extra-large (> 12-ring) pore, while the number of pore opening rings less than 8 is regarded as nonporous (Figure 2.2) [5].

Zeolite structures obey the Löwenstein's rule avoiding Al–O–Al linkages because of the violation of framework charges [7]. Similarly, the P–O–P linkage appears to be unlikely in AlPOs. For this reason, almost every phosphate structure has an even number of rings in their frameworks, i.e., 4, 6, 8, 12 rings. Therefore, structures with odd numbered rings, are very rare for AlPOs or SAPOs families.

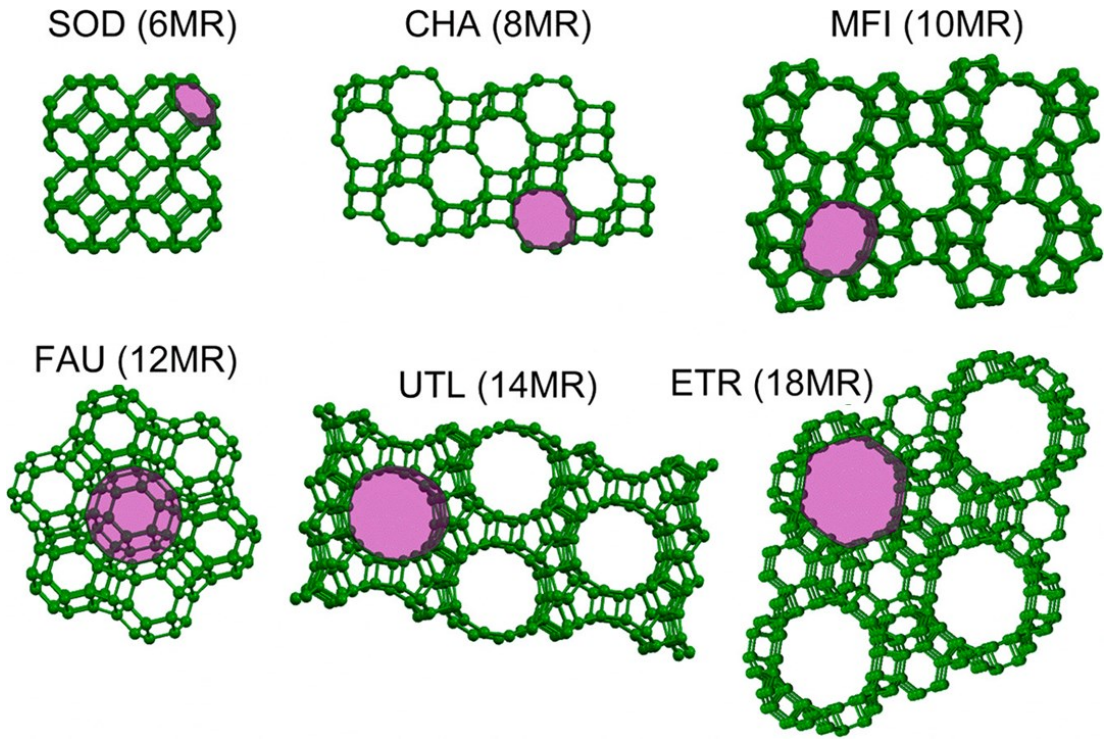


Figure 2.2 Zeolite frameworks with different pores: **SOD** with 6-ring pores of 2.8 Å; **CHA** 8-ring (3.8 Å); **MFI** 10-ring (~ 5.5 Å); **FAU** 12-ring (7.4 Å); **UTL** 14-ring (~ 9.5 Å); and **ETR** 18-ring (10.1 Å) [6].

### 2.1.2.2 Secondary building units

Zeolite frameworks can be considered as being composed of finite component units or infinite component unit-like chains and layers. Secondary building units (SBUs) were derived with the idea that an entire framework could be built using a single SBU [5]. SBUs are non-chiral units with up to 16 T-atoms. At present, 23 kinds of SBUs have been found, as shown in Figure 2.3. Each zeolite can possess one or more SBUs. For instance, **MFI** framework comprises only one type of SBU (5-1), while **LTA** contains five types of SBUs, including 6-2, 4-4, 4-2, 4, and 8 units.

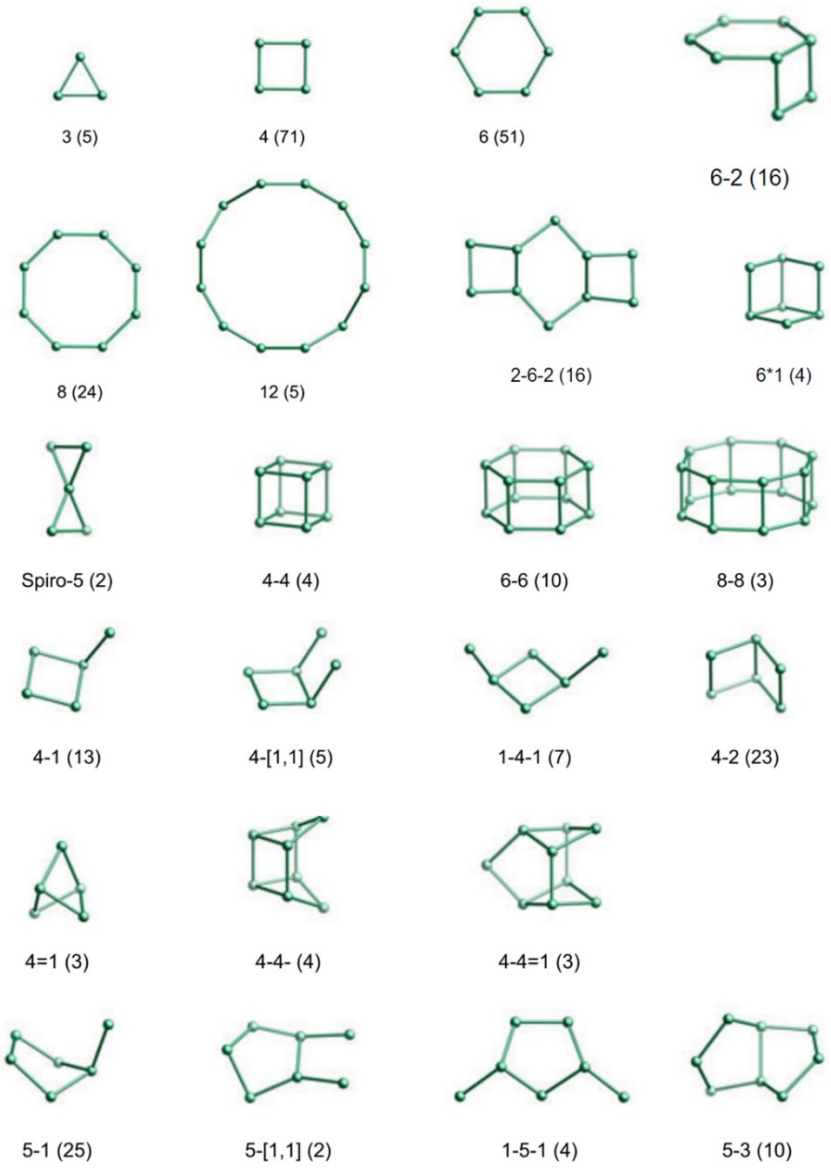


Figure 2.3 23 kinds of SBUs, adopted from IZA database.

### 2.1.2.3 Composite building units

Although each type of zeolite framework can be described by SBUs, the complexity increases with the increase in the number of new complicated structures. As a result, composite building units (CBUs) are often used to describe the zeolite structures [5]. Except for double 4-rings (*d4r*), double 6-rings (*d6r*), and double 8-rings (*d8r*), each CBU is assigned a lower case italic three-letter code, which is related to the type of framework they featured in. At present, 59 types of CBUs have been identified (Figure 2.4).

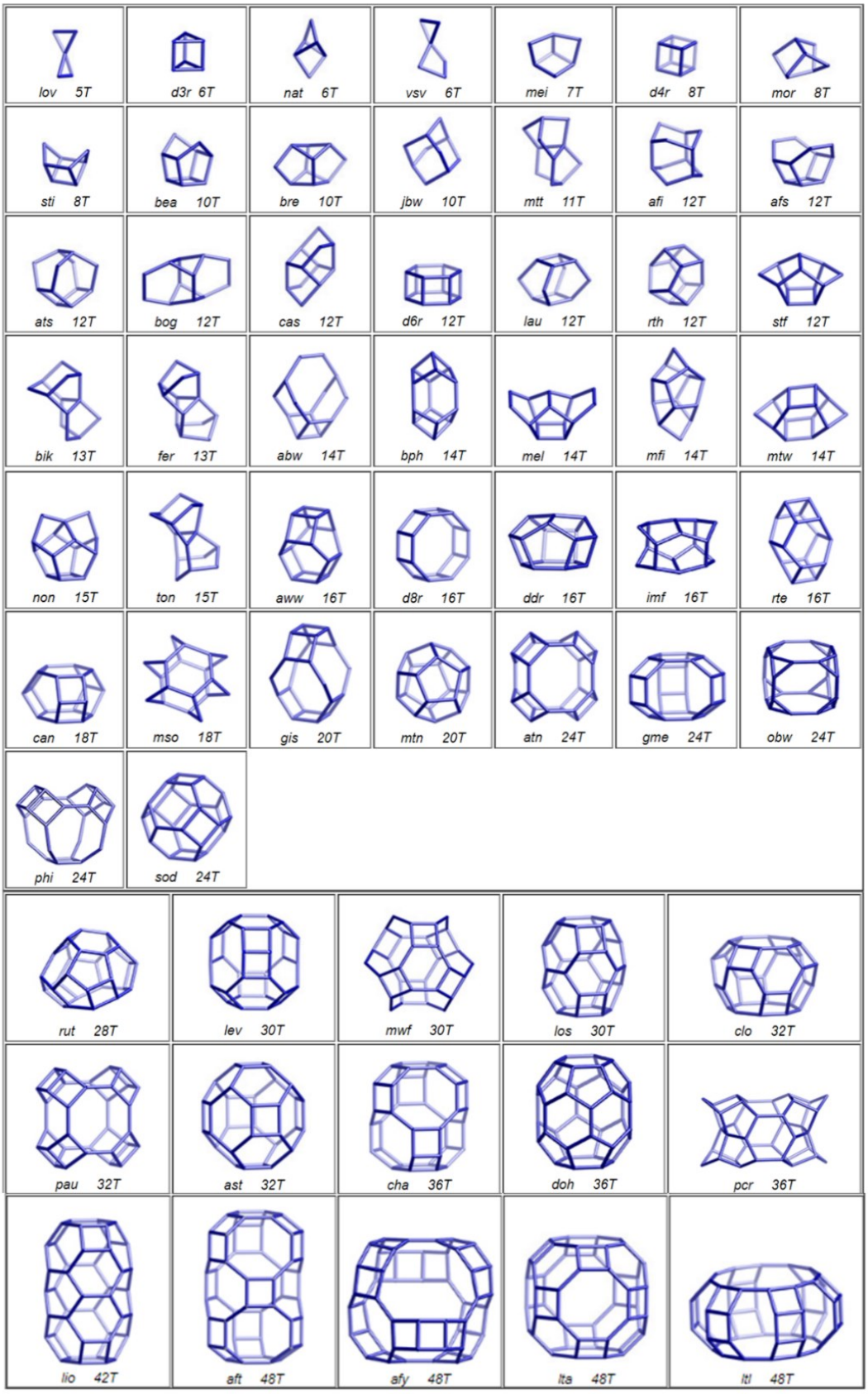


Figure 2.4 59 types of CBUs (*lov, d3r, d4r*, *d6r*, and *d8r* are also classified as SBU), adopted from IZA database.

### 2.1.2.4 Characteristic chain- and layer-building units.

Six chain units that frequently appeared in zeolite frameworks are shown in Figure 2.5, that is, *dzc*, *dsc*, *dcc*, *nsc*, *dnc* and pentasil chain [4, 5]. The *nsc* is more common in AlPO-based structures, while the pentasil chain composed of edge-sharing cages is a characteristic of high-Si zeolites (*e.g.* **MEL** and **MFI**).

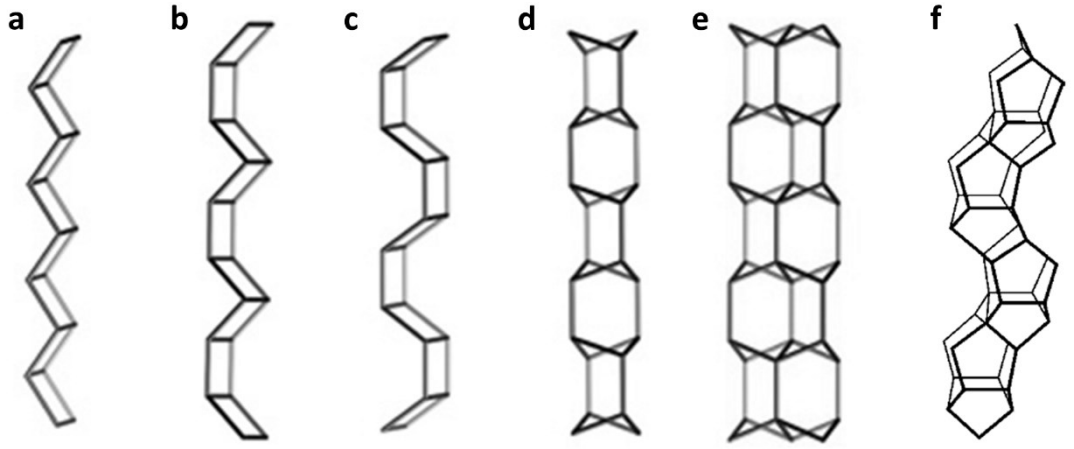


Figure 2.5 (**a**) Double zig-zag chain (*dzc*); (**b**) double sawtooth chain (*dsc*); (**c**) double crankshaft chain (*dcc*); (**d**) narsarsukite chain (*nsc*); (**e**) double narsarsukite chain (*dnc*); (**f**) pentasil chain.

Zeolite structures that can be described using the same 2D layer are considered as polytypes. Polytypes consist of identical layers, and differ only in the stacking sequence of these layers. For example, ***BEA** zeolite consists of three polymorphs, polymorph A, polymorph B, and polymorph C (Figure 2.6).

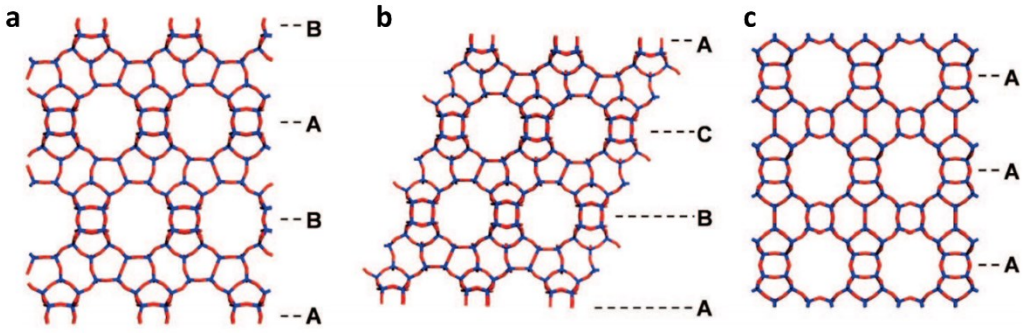


Figure 2.6 Zeolite ***BEA** in (**a**) polymorph A, (**b**) polymorph B, and (**c**) polymorph C, showing different stacking orders (**a**) ABAB, (**b**) ABCABC, and (**c**) AAA [8].

### 2.1.3 Synthetic chemistry of zeolites

Zeolites are generally prepared by hydrothermal synthesis in aqueous media where sources of T-elements (Si, Al, Ge, B, etc.), inorganic and/or organic cations are mixed together in basic or fluoride media. In the most cases, an organic compound acts as a SDA. The crystallization proceeds in a closed vessel (*e.g.* autoclave) at increased temperature (usually 100 – 240 °C) under autogenous pressure for a period from few hours to several months (Figure 2.7) [1, 9]. In the following subsections, the role of the reaction mixture components in the synthesis and the details of hydrothermal synthesis of zeolites are discussed.

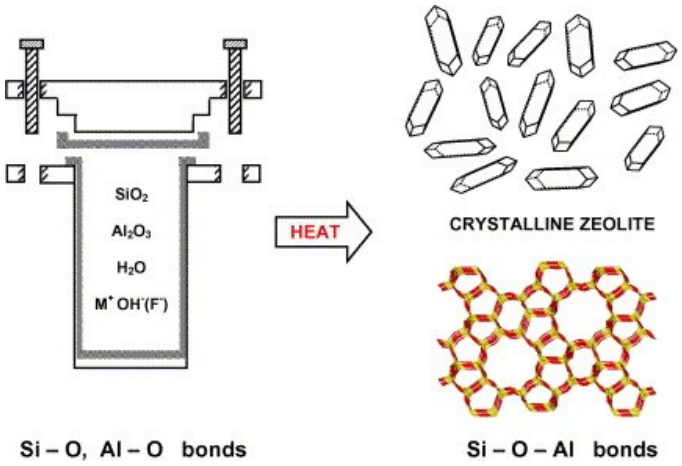


Figure 2.7 Hydrothermal synthesis of zeolites [9].

#### 2.1.3.1 Components of typical reaction media

**Reactants.** In general, the synthesis gel utilized for preparation of aluminosilicate zeolites contains aluminum and silicon sources, inorganic or organic cations, mineralizer, and water. The Si and Al sources are the main sources for the formation of zeolite framework skeleton. The Al sources, generally, include $Al_2(SO_4)_3$, AlOOH, $Al_2O_3$, $Al(OH)_3$, Al(O-i-Pr)$_3$, and as on, while Si sources are TEOS, silica gel, fumed silica, etc. The inorganic or organic cations are necessary in the synthesis of $T^{III}$-containing zeolites, such as aluminosilicates, gallosilicates, borosilicates. They are not only used for the charge balance in zeolite framework but also they act as SDAs for particular structures. As an example, different cations located between the pre-FER layers result in two kinds of zeolites, i.e. **FER** and **CDO**, after the condensation of the layers [10].

**Mineralizing agent.** Hydroxide ion is the most common mineralizing agent, which can dissolve T-element sources (Si, Al, etc.) and provides the reversible T−O−T bond formation and hydrolysis during the synthesis of zeolites. Siliceous zeolites prepared in $OH^-$ medium are usually obtained at high pH, leading to the generation of some silanol defects. In contrast to $OH^-$, $F^-$ [11, 12] allows to significantly eliminate those defects, this can be explained by the charge balance of the framework with occluded $F^-$, and complete condensation of the silica in neutral medium [13, 14]. In addition, the presence of $F^-$ can also facilitate the incorporation of heteroelements (Al, B, Ga, Fe, and Ti) into the zeolite (high-Si or all-Si) frameworks because $F^-$ can react with most of elements to form the complex ions [15, 16].

**SDA.** The application of organic quaternary ammonium cation (known as OSDA) is regarded as a milestone for the hydrothermal synthesis of zeolites [17, 18], which accelerates the discovery of zeolites with novel structures. Two key zeolites for the industry, beta (***BEA**) [19] and ZSM-5 (**MFI**) [20], were hydrothermally synthesized by using respective tetraethylammonium and tetrapropylammonium as OSDAs in 1967 and 1972, respectively. The role of these organic cations is generally proposed [21] as (1) template effect, zeolite framework is closely related to the shape and size of OSDA molecules; (2) structure-directing effect, an OSDA directs the crystallization towards the formation of a particular type of zeolite framework; (3) pore-filling effect, OSDAs in the cavity stabilize the open zeolite framework through the non-bonded host-guest interaction; and (4) zeolite framework charge compensation which caused by the non-$T^{IV}$ framework atoms. It is worth noting that these effects simultaneously occur more or less in the course of organic-involved zeolite synthesis [22].

**Water.** Water not only is an excellent solvent but also participates in the formation of zeolites. The steam water can provide the self-generated pressure in the autoclave at higher temperatures. Moreover, the ratio of $H_2O/SiO_2$ may also significantly affect the phase selectivity of zeolite crystallization. For example, pure siliceous zeolite **CHA** can only be formed at $3 \leq H_2O/SiO_2 \leq 5.3$, otherwise a second phase **STT** is present when the $H_2O/SiO_2$ is lower than 3 or higher than 5.3 [23].

### 2.1.3.2 Hydrothermal synthesis

Hydrothermal synthesis was successfully applied for the zeolite synthesis in 1940s through mimicking the conditions of generation of natural zeolites [3]. The hydrothermal

synthesis can be carried out in either static or tumbling conditions. The agitation can facilitate the mass transport in the reaction media [24]. Agitation is revealed to influence the crystallization kinetics, particle size distribution, and chemical composition of the framework [25]. The stirring of the reaction mixture can also influence the outcome of final crystal structures. Hanif *et al.* found that pure **FAU** and **EMT** phases can be obtained with agitation, while an intergrowth of **FAU** and **EMT** phases is the main product under static condition due to the decrease in local concentration of the reactants at the liquid-solid interface below the "apparent" concentration as a result of limited mass transport [26].

Hydrothermal synthesis method has been widely applied in zeolites synthesis for decades. However, the system consists of some environmentally unfriendly issues: large amount of organic/inorganic templates, waste of water for purification, time-consuming synthesis, and so on. To reach the purpose of sustainable chemistry, many efforts have been devoted to develop sustainable synthesis protocols [27-29], using low-cost, recyclable templates, or template-free system [30-32]. In addition, several techniques, such as microwave heating [33], hydroxyl free radicals assisted synthesis [34], and rapid synthesis in capillary [35], were developed to speed up the crystallization kinetics of the hydrothermal synthesis. Okubo *et al.* developed an ultrafast synthesis strategy for the synthesis of zeolites in a "mini autoclave" which can produce $AlPO_4$-5 in one minute [36-38].

#### 2.1.3.3 Seed-assisted synthesis

Synthesis of targeted zeolites using hydrothermal method is still challenging due to the slow crystallization kinetics of zeolite and the appearance of undesirable phases. The seed-assisted technique by adding crystal seeds in the synthesis gel has opened a new horizon for the synthesis of many useful zeolites [39]. The required time to obtained crystalline zeolites is highly reduced when crystal seeds are added into the synthesis gel [40]. Moreover, the size and morphology of crystals can be affected by the seeds [41]. Yu *et al.* systematically studied the effect of seed size on the synthesis of SAPO-34 (**CHA**) crystals and found that non-uniform micron-sized cubic crystals of SAPO-34 were obtained when micron-sized seeds are used, while uniform nano-sized crystals were formed when using nano-sized seeds (Figure 2.8) [42]. Many zeolites can be synthesized in the absence of OSDAs using seed-assisted strategy, such as **MFI** [43], ***BEA** [44, 45], and SAPO-34 [46].

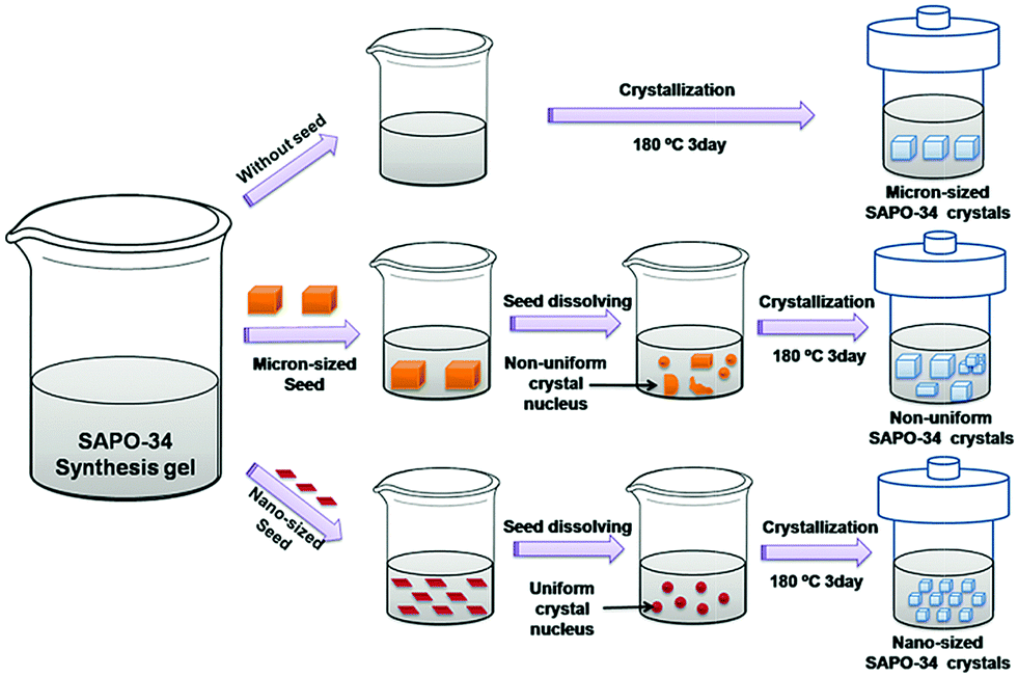


Figure 2.8 Schematic representation of the influence of the size of seeds on the final crystal size [42].

Many works have been carried out to study the mechanism of seed-assisted crystallization. Generally, two mechanisms prevail in the seed-assisted crystallization: (1) the seeds undergo partial dissolution and new crystals grow on the surface of seeds [45, 47, 48]; (2) most of seeds are dissolved and the essential building units can direct the new crystal growth [36, 49, 50]. Regarding to the partial dissolution mechanism [45, 47], viable crystals were developed on the surface of the partially dissolved crystals which act as the SDA to direct the crystal growth (Figure 2.9, top). While in some cases, the seed crystals are completely dissolved and the released species contain the building units of seed structures, which can promote the crystallization and crystal growth. Therefore, a different crystal shape can be obtained when using the seeds prepared in a conventional autoclave, while no significant difference can be observed by reusing the seeds obtained (Figure 2.9, bottom) [36].

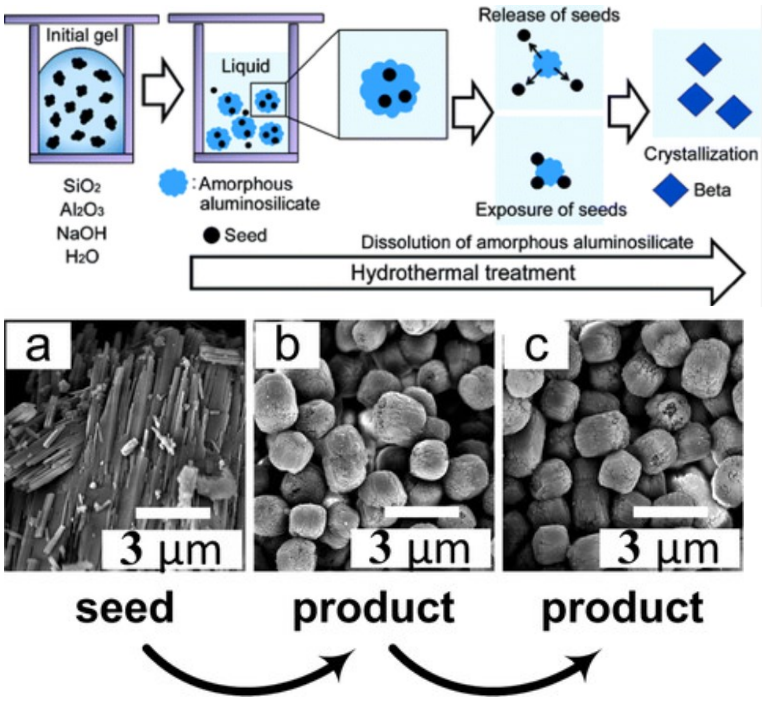


Figure 2.9 Schematic presentations of the crystallization processes in seed-assisted synthesis of ***BEA** without OSDA (top) [47]. Crystal morphologies of $AlPO_4$-5 synthesized using the product as seeds (bottom) [36]. Seeds prepared by the conventional hydrothermal method (**a**); products synthesized in the continuous flow reactor using "a" as the seeds (**b**), and in an iteration way the obtained "b" was used as seeds for synthesis "c" (**c**).

## 2.2 Zeolite crystallization: classical and reversed crystal growth

### 2.2.1 Classical crystal growth

Zeolites are metastable crystalline materials that are commonly synthesized from amorphous aluminosilicate precursors in an alkaline/neutral aqueous solution. Understanding the zeolite crystallization mechanism, especially at the molecular level, is essential for the development of materials with desired properties and for the improvement of synthesis protocols [51]. However, such a comprehesive insight into the mechanism is still elusive due to a large amount of species present in the synthesis mixtures and many factors affecting the formation of final products [52]. Generally, the accepted crystallization mechanism (Figure 2.10), that is defined as classical crystal growth, includes three main steps [53, 54]:

(1) induction period, prenucleation including depolymerization of the source of heteroelements with further formation of oligomeric (element)-silicate ions upon condensation;

(2) nucleation period, i) primary nucleation consisting of the reorganization of oligomeric anions and $SDA^+$ into clathrate-like primary units; ii) generation of nuclei centres by aggregation of the silicate clusters;

(3) crystal growth.

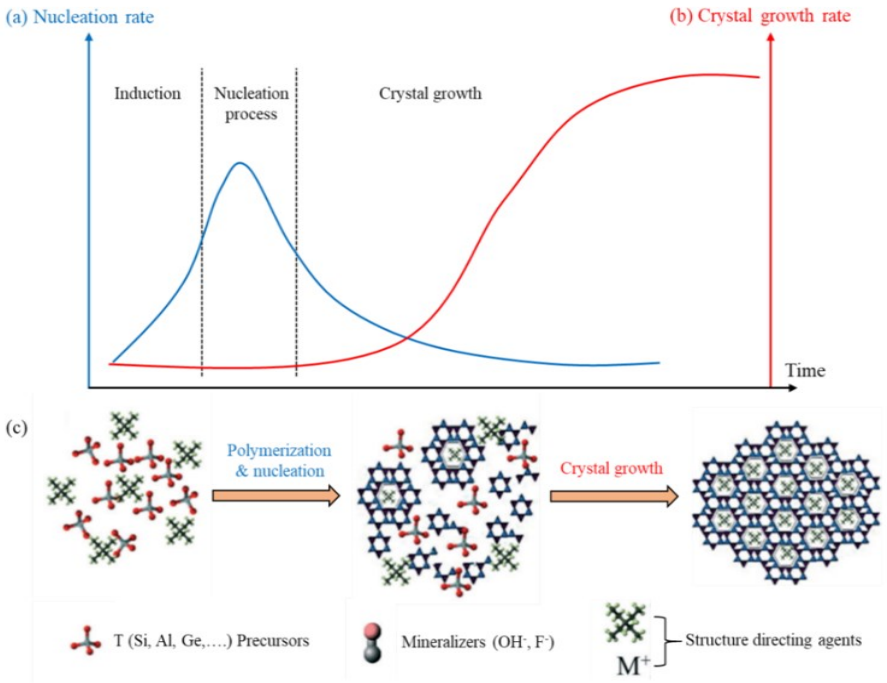


Figure 2.10 Schematic representations of the (**a**) nucleation rate and (**b**) crystal growth rate of zeolites, and (**c**) related rearrangements from amorphous particles into crystalline zeolite during the synthesis [55].

### 2.2.2 Reversed crystal growth

The reversed crystal growth mechanism was firstly reported for the zeolite **ANA** in 2007 [56]. In contrast to the classical model assuming the growth from the nuclei center, in the reversed crystal growth, the crystallization begins with the integration of nanocrystallites on the very early stage of crystallization into large aggregates, which is followed by the recrystallization starting at its surface towards the center. Therefore, the crystal growth direction in the reversed mechanism is from the surface to the center. So far, the recrystallization (i.e. formation of *crystalline* phase from another *crystalline* phase) of

aggregates in the reversed crystal growth has been found in many systems, including zeolites [57, 58], perovskites [59, 60], metal oxides [61, 62], and metal-organic frameworks [63, 64].

The formation of zeolite **ANA** is a representative example to illustrate the crystallization mechanism in the reversed crystal growth [56], as shown in Figure 2.11. The crystalline nanoplates (**ANA**) with an average diameter of ~ 20 nm were formed at the beginning of crystallization (Figure 2.11a). Then, these crystallites spontaneously agglomerated to form discus-shaped aggregates via an oriented aggregation mechanism (Figure 2.11b).

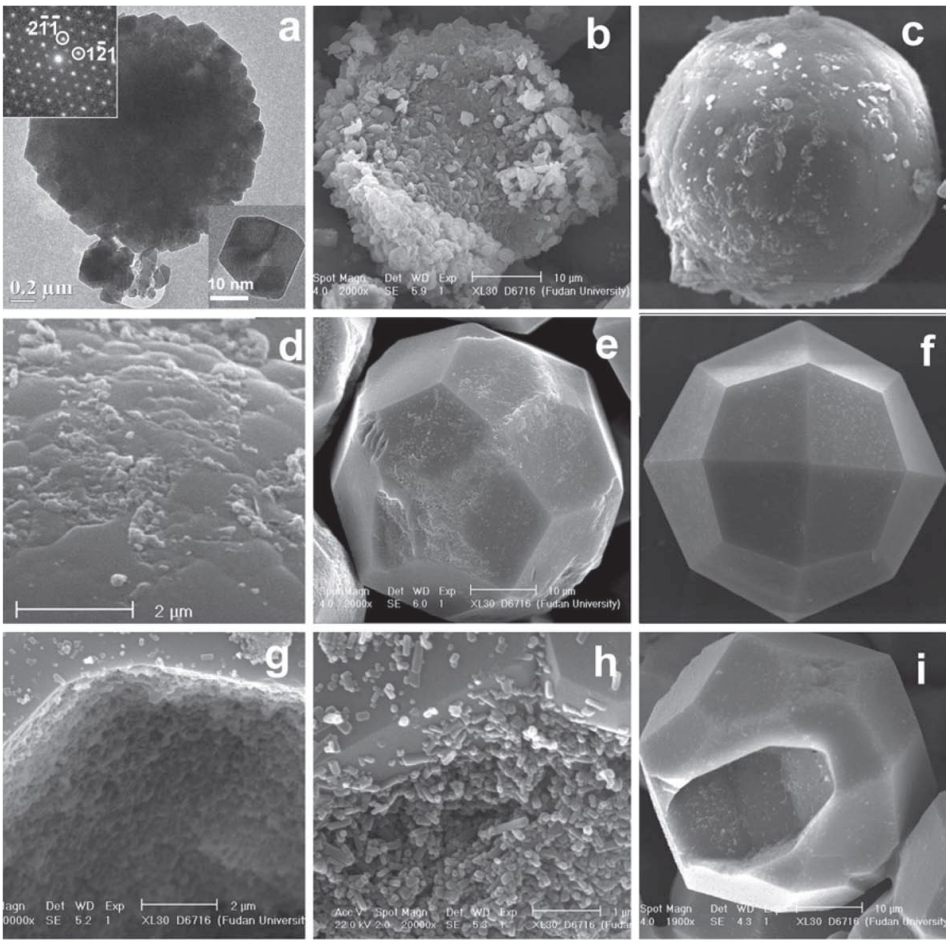


Figure 2.11 TEM (**a**) and SEM (**b–i**) images of zeolite ANA formation in different synthesis time through the reversed crystal growth mechanism [56, 65].

These aggregates further self-assembled into polycrystalline microspheres (Figure 2.11c). Due to the limited space and restricted mass transport inside the microspheres, the crystalline nanoplatelets inside the microspheres grew into large nanorods via Ostwald ripening. Simultaneously, a single crystalline thin shell was formed on the surface of the microsphere via surface recrystallization (Figure 2.11d). As a result, an icositetrahedral

morphology is gradually developed (Figure 2.11ef). With the prolongation of synthesis time, the single crystalline shell increases in thickness through the consumption of inner nanorods (Figure 2.11gh), as a result, a single-crystal icositetrahedra with a small hole is generated (Figure 2.11i). Except for the formation of zeolite **ANA** from amorphous silicon-aluminum sources, zeolite **ANA** with a regular icositetrahedral morphology can also be synthesized via transformation of zeolite Y though the reserved crystal growth mechanism [66].

In addition to such mechanism, crystallization starting at the surface of amorphous aggregates (i.e. formation of *crystalline* phase from *amorphous* state) towards their centers instead of recrystallization of preformed crystallites is a conceptually different type of reversed crystal growth. This kind of mechanism is not so common as the aforementioned type of recrystallization, which is probably due to the fast formation of crystallites at the very early stage of crystallization [65, 67]. Confinement of starting materials within the matrix of polymers can inhibit the free growth of crystals and provide particular nucleation sites at the host-guest interfaces stimulating the reversed crystal growth. Wang *et al.* reported cube-like zeolite A with a core-shell structure was formed via particle aggregation and surface- to-core crystallization by adding extra chitosan polymer into the initial synthesis gel [68], as shown in Figure 2.12. Despite a well crystalline shell can be obtained when the gel was aged overnight at room temperature before the hydrothermal treatment, a second phase (**SOD**) is formed inside the cubes under hydrothermal conditions for 4 hours.

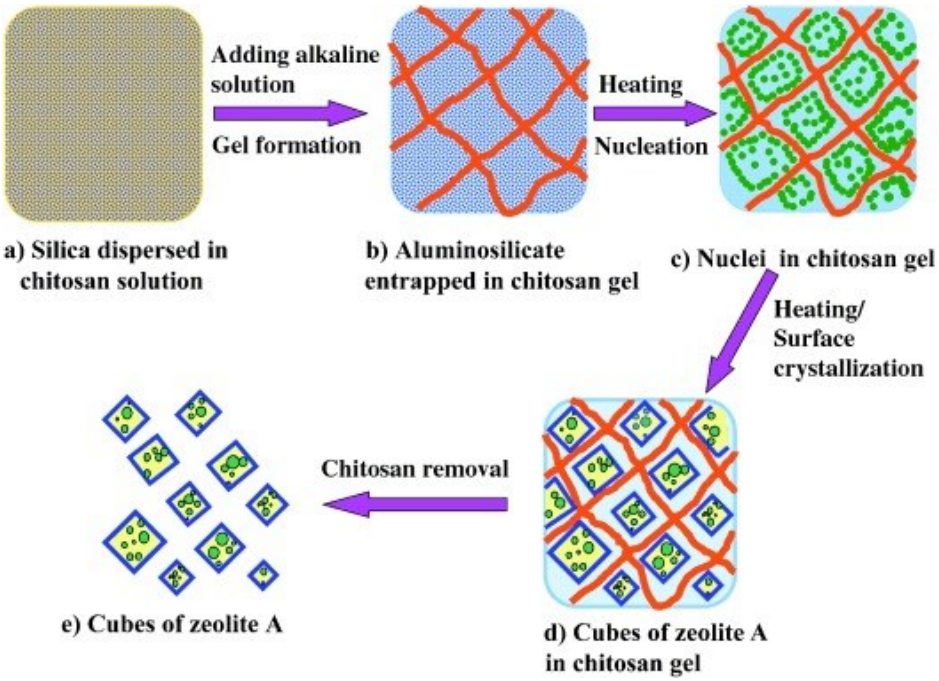


Figure 2.12 Schematic presentation of the formation of cubic zeolite A with a core-shell structure in the presence of chitosan polymer [68].

Zhou *et al.* systematically studied this formation process through the step-by-step observation of crystal growth and confirmed the aggregation and surface- to- core crystallization mechanism for the formation of zeolite A [69]. Unfortunately, a second phase (**SOD)** appeared at the cube center when a crystalline shell was formed and it grew further by consuming the amorphous species and then the crystalline zeolite A. Finally, only **SOD** zeolite was obtained (Figure 2.13). Therefore, the formation of zeolite A and its transformation to **SOD** is strictly not a model example for reversed crystal growth based on its definition because the crystallization of zeolite A does not reach its center despite a crystalline shell is formed. Besides, the formation of crystalline shells at the beginning of crystallization was also observed in the synthesis of ZSM-5 when mesoporous silica spheres were used as the starting silica sources [70].

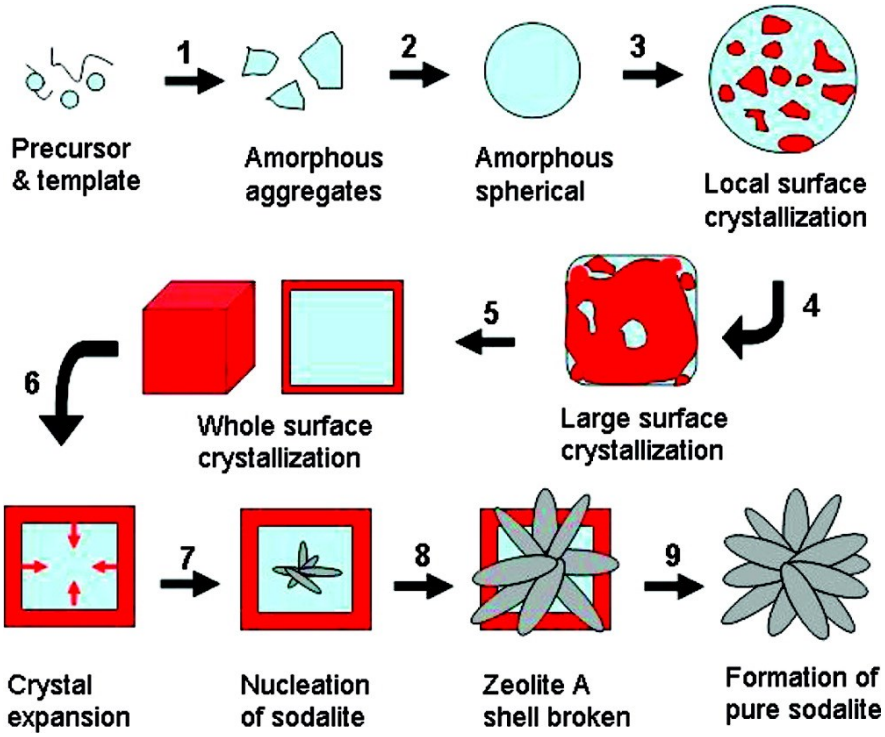


Figure 2.13 Schematic presentation of growth of zeolite A (**LTA**) via reversed crystal growth mechanism and phase transformation from zeolite A to sodalite (**SOD**) [69].

Although the reversed crystal growth mechanism has been observed in many systems, it has not been fully understood yet.

(1) The proof of the reversed crystal growth mechanism in these materials requires more experimental work [65]. The proposed surface crystallization of zeolite A in the

reversed crystal growth has not been directly observed and hence the transformation from the spherical to cubic morphologies has not been proved (step 4 in Figure 2.13) [69].

(2) The mechanism in the aggregation process is still elusive [65]. The reason for the formation of nanoplatelets with a short axis along the (111) domain axis of zeolite **ANA** is not yet fully understood, nor is the reason for the perfectly oriented aggregation of these nanoplatelets [56].

(3) What is the pathway-determination factor and how does it influence the crystallization mechanism? Aggregation of small species at the early stage is believed to be the most important step in reversed crystal growth [67]. For example, multiple nucleation of $CaCO_3$ can take place either on the surface of the aggregates or inside the aggregates depending on the interaction strength between $Ca^{2+}$ and polymer additives [71]. A change of the crystallization mechanism from the classical to the reversed crystal growth was found in several systems when additional organic molecules (e.g ethylamine.) or polymers (chitosan or gum arabic) was added into the synthesis gel [56, 69, 72]. However, inhibition of the free growth of crystals cannot explain aggregation at the early stage in other systems acting without adding any extra agents. Generally, the synthesis system contains a mixture of inorganic and organic ions (SDAs, mineralizing agents, other modifiers) and the interaction between them was assumed to affect the initial aggregation [67, 73, 74]. However, no direct evidence was reported to confirm the relevance of this assumption [65, 67, 73].

In chapter 4.1, we present a truly reversed zeolite crystal growth process, in which the crystallization starts from the surface of amorphous aggregates and then proceeds towards their centers. In addition, the crystallization mechanism regarding to the pathway-determination factors and crystal growth rate will be discussed in detail.

## 2.3 Structural flexibility of zeolites: ADOR strategy

### 2.3.1 General aspects of ADOR

3D zeolites are the most common products that crystallize directly from the reaction gel under hydrothermal conditions (bottom-up route). One of the main weaknesses for the conventional hydrothermal method is the limited control of the “black” reactor and the lack of predictable synthesis of products [75]. For such a purpose of control, many researches have been carried out to provide a basic understanding of the parameters including the nature of

SDA, mineralization agents ($OH^-$, $F^-$), and $H_2O$/T ratio, etc. [76]. Besides, alternative approaches in a top-down route for synthesis new zeolite structures are developed [75, 77].

The introduction of Ge into the zeolite synthesis mixtures has promoted the discovery of many highly open zeolite structures containing *d4r* and/or *d3r* and/or *s3r* units, which have not been achieved in their silicate or aluminosilicate forms [78-82]. From a structural point of view, germanosilicate zeolites are worthy of interest, however, their applications are highly hindered due to the structural instability caused by the readily hydrolysable Ge−O bonds [83, 84]. One typical structural feature of some germanosilicate zeolites is that their frameworks are composed of the stable Si-rich layers (or clusters) connected by labile Ge-rich *d4r* units [85]. Therefore, Si-rich domains can be potentially reassembled into a 3D zeolite under specific conditions if partial or complete removal of Ge-rich *d4r* linkages happen [86]. This is the basis of so-called ADOR (assembly-disassembly-organization-reassembly) process, which is developed in our group [87].

In contrast to the hydrothermal (bottom-up approach) synthesis, ADOR is a top-down approach for the synthesis of 3D zeolites. ADOR protocol consists of 4 steps (Figure 2.14): (1) *assembly* involving the hydrothermal synthesis of parent zeolite with the desired characteristics (*i.e.* zeolites containing both stable and labile parts); (2) *disassembly* involving the selective removal of the Ge-rich *d4r* domains, resulting in the formation of layered precursor; (3) *organization* including rearrangement/reintercalation to correct the orientation of layers for later reconnection; (4) *reassembly* involving the condensation of layers to form a new daughter zeolite.

In comparison with the conventional hydrothermal synthesis, new materials prepared using ADOR strategy can possess strong structural strain because the formation of ADOR products does not carry out under equilibrium conditions [77]. Generally, the formation of highly-energetic (i.e. thermodynamically unfeasible or unfavorable) zeolites by the hydrothermal synthesis is considered to be impossible as the most stable products tend to form accordingly in the equilibrated reaction mixtures. Synthesis of the so-called “unfeasible” zeolites was realized via ADOR when using **UTL** as the parent zeolite along with the required organization agent (choline cation) [88].

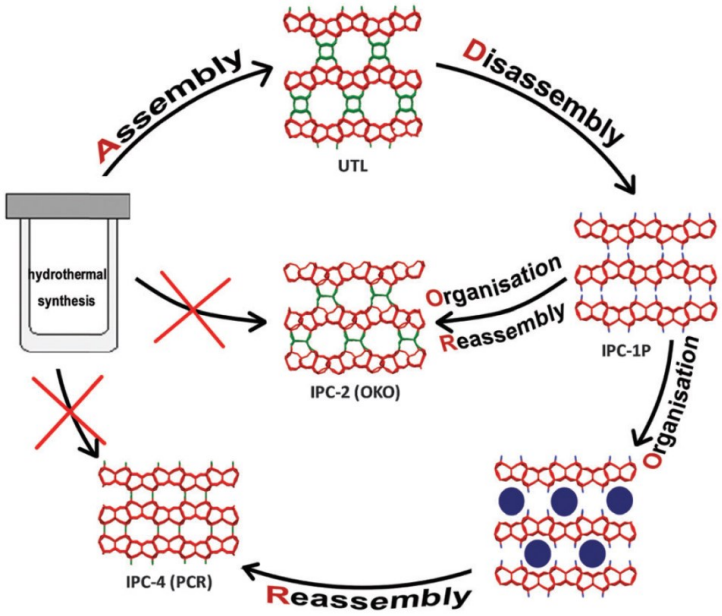


Figure 2.14 Schematic representation of the ADOR protocol for the synthesis of IPC-2 (**OKO**) and IPC-4 (**PCR**) zeolites from **UTL**; both daughter zeolites have not been yet synthesized through the direct hydrothermal method [87].

Key features required to achieve the successful preparation of new zeolites by applying ADOR strategy are the structure and chemical composition properties of the parent zeolites. The successful cases so far are mainly germanosilicate zeolites possessing Ge-rich *d4r* units [77]. Generally, an "ADORable" zeolite should have a sufficiently high number of Ge in the *d4r* units, which is enough to disconnect the zeolite framework and to form the independent Si-rich layers. It can be expected that each *d4r* unit should contain at least 4 Ge atoms for the realization of complete disconnections between the layers of the parent zeolite. As shown in Figure 2.15, among the six possible configurations of 4 Ge atoms within a *d4r* unit, only (a) and (b) allow the full separation of Si-rich layers [87]. Germanosilicate zeolites possessing the remaining configurations (c) – (f) are hydrolytically stable under acidic conditions (germanosilicate structure remains unchanged in the acid treatment) due to the presence of Si−O−Si linkages between the layers. Therefore, at least 4 Ge atoms presented in each *d4r* unit are required for the full separation of layers. Moreover, different arrangements of Ge in *d4r* units will seriously affect the final products. **UTL** with Si/Ge = 6 is an illustrative example, in which each *d4r* unit contains 4 Ge atoms (assuming Ge occupies only *d4r* units). According to the results of $^{19}$F MAS NMR and $^{1}$H – $^{29}$Si CP/MAS NMR in **UTL**, Ge preferentially forms one Ge *s4r* attached to the layer (corresponding to the configuration (a) on Figure 2.15) and hence the layers can be fully disassembled [80, 89]. However, in the case of **IWW** or **ITH**, Ge is randomly distributed in all T-sites of *d4r* [89], resulting in an

incomplete separation of Si-rich layers when a considerably low Ge concentration is achieved [90, 91].

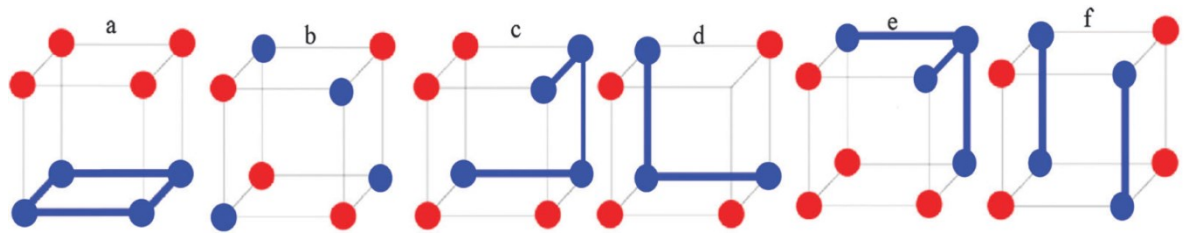


Figure 2.15 Different arrangement of 4 Ge atoms (red) and 4 Si atoms (blue) within *d4r* units [87].

### 2.3.2 ADOR mechanism: UTL as an example

#### 2.3.2.1 Assembly

The first step in the ADOR protocol for the structural transformation of germanosilicate zeolites is the *assembly*, that is, synthesis of parent germanosilicate zeolites. The hydrothermal synthesis generally involves the preparation of synthesis gel with particular compositions, crystallization of germanosilicates, and removal of organic cations in the cavity of germanosilicates. For example, **UTL** zeolite is synthesized with a synthesis composition of 0.8 $SiO_2$: 0.4 $GeO_2$: 0.4 DMAH: 30 $H_2O$ at 175 °C for 7 days under agitation.

#### 2.3.2.2 Hydrolysis

The hydrolysis of Ge−O bonds occurs immediately when the parent **UTL** is in contact with water or acid solution. Henkelis *et al.* systematically studied the hydrolysis of **UTL** in water at elevated temperature, and all steps related to disassembly and rearrangement are shown in Figure 2.16 [92]. An IPC-2P* intermediate containing IPC-2P structure but with Ge residing within the layers is formed in 1 min. The remaining Ge−O bonds are further hydrolyzed to form IPC-1P (precursor of **PCR** zeolite with interlayer O-bridge connectivities) in 30 min, in which all *d4r* units have been completely removed. Considering the dominant occupation of *d4r* units by Ge, changes of XRD patterns related to the inter-layer planes can be observed owing to the generation of a layered material (Figure 2.17). As a result, removal of *d4r* units leads to a shrinkage of the interlayer spacing ($d_{(200)}$) from 14.5 to 10.5 Å) [93].

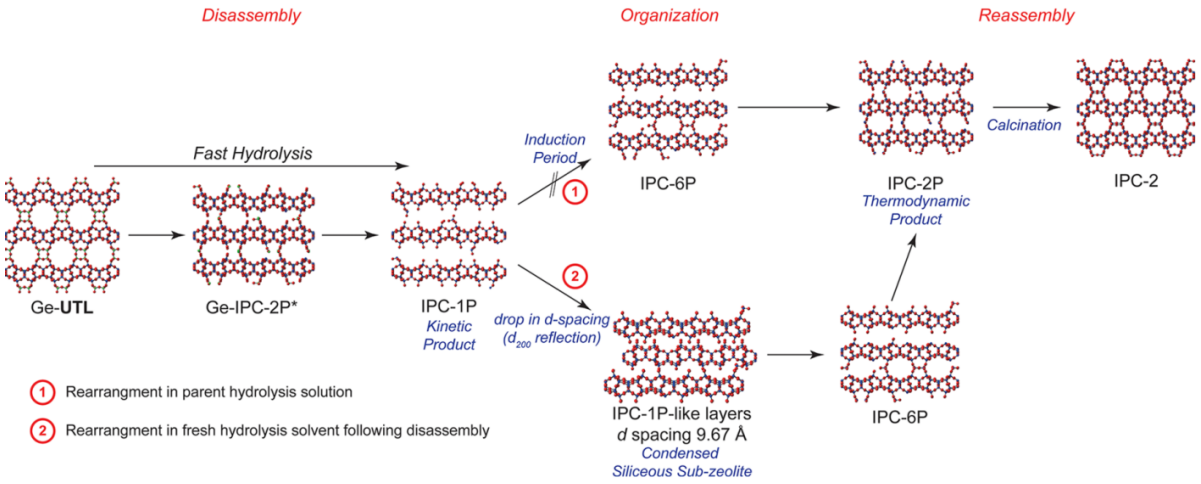


Figure 2.16 Elementary steps of the ADOR process for **UTL** hydrolysis at 100 °C in water [92].

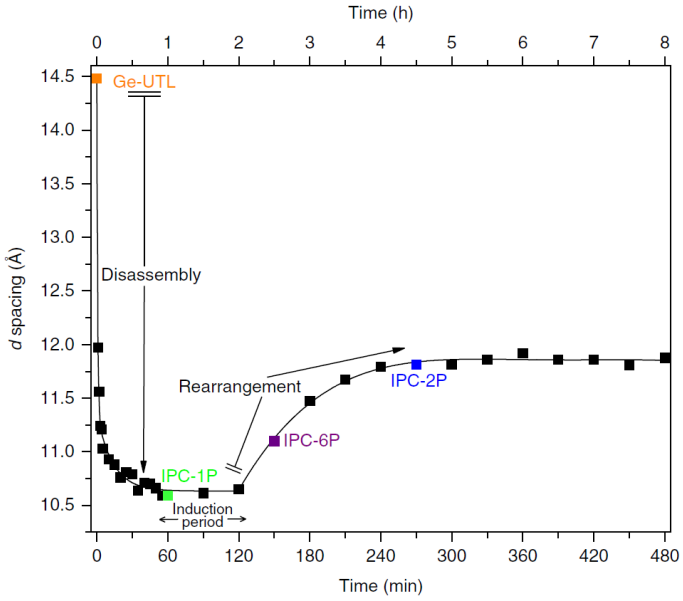


Figure 2.17 The variation of d-spacing for the (200) refection of UTL vs reaction time in water at 100 °C [93].

### 2.3.2.3 Rearrangement

The complete hydrolysis of *d4r* is not the end of the reaction in water. It is possible to intercalate extra Si between the layers to form a new zeolite precursor IPC-2P (precursor of **OKO** zeolite with *-s4r-* interlayer linkages). That is so-called rearrangement. The rearrangement to form IPC-2P ($d_{(200)}$ = 11.75Å) through the IPC-6P intermediate ($d_{(200)}$ = 11.53Å, precursor of the stage-structured ***PCS** zeolite with 1:1 ratio of **PCR**- and **OKO**-type linkages) begins after an induction period when IPC-1P ($d_{(200)}$ = 10.50Å) forms (Figure 2.17). Two possible sources of Si upon rearrangement are proposed, that is silicate in the solution

after hydrolysis or silicon in the Si-rich layers (Figure 2.16). By recording the differences after removing the Si-rich solution via replacing with fresh water when the hydrolysis is finished, Henkelis *et al.* found that the silicon for rearrangement is mainly from the Si-rich layers of the parent germanosilicates, confirmed by the observation of the defective Si-rich layers with smaller d-spacing.

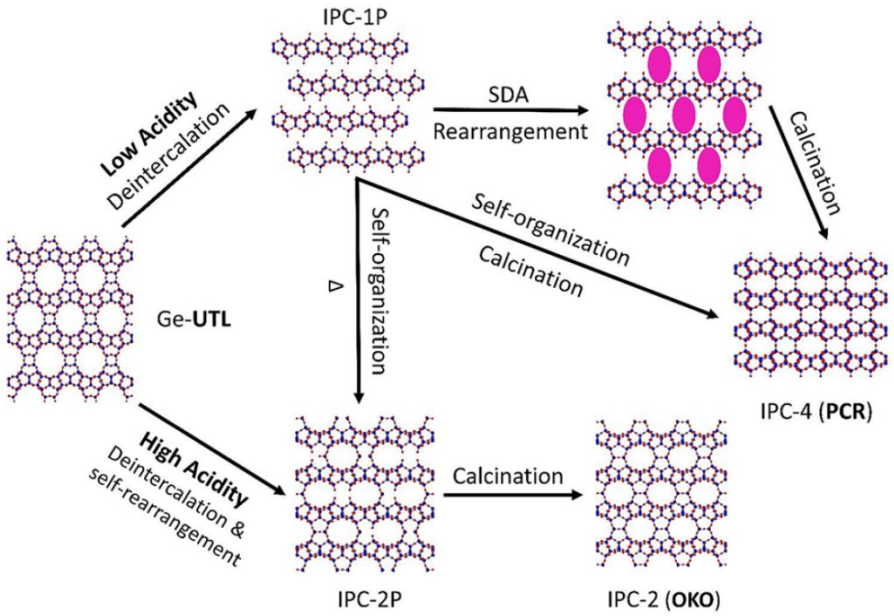


Figure 2.18 The *organization* step in ADOR by intercalation with a SDA (top) or a hydrolysis/deintercalation and self-rearrangement in acid (bottom) [92].

Hydrolysis and rearrangement of intermediate precursors in acid solution are slightly different from that in water (Figure 2.18). The structures of final products obtained depend on the acidity of solution and reaction temperature. At room temperature, IPC-1P is the final products in low concentrated acid solutions, while IPC-2P will be formed in highly concentrated acid solutions [94]. This difference can be explained by the ability for self-arrangement of the disassembled layers at high acidity condition at room temperature after full removal of Ge-rich *d4rs,* while it can only be stimulated at high temperature in low acidic solution. Besides the self-rearrangement of IPC-1P in solution, intercalation of SDA can also organize the layers to direct the formation of final zeolites with different connectivity. A well crystalline IPC-4 (**PCR**) can be obtained by calcination after the intercalation of octylamine into the interlayer space of IPC-1P [86]. Moreover, IPC-10P and IPC-9P can be obtained by treatment of IPC-1P in the choline hydroxide solution either in the presence or absence of dimethyldiethoxysilane, respectively (Figure 2.19) [88].

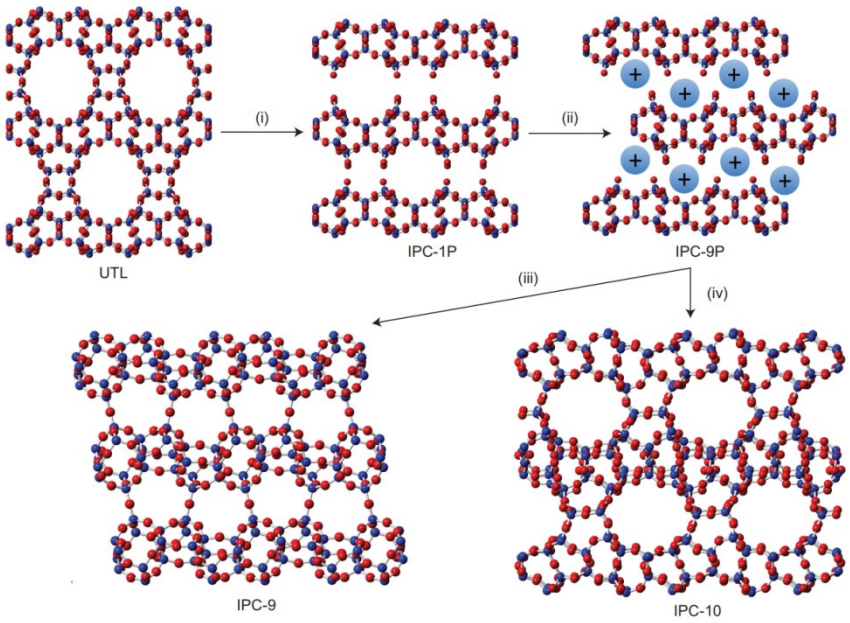


Figure 2.19 The ADOR process in the formation of IPC-9 and IPC-10 [88]. (i) Disassembly step for the formation of IPC-1P; (ii) followed by the introduction of choline cations (blue balls with positive charges) between the layers to form IPC-9P, which can be reassembled in two ways: (iii) direct calcination to form IPC-9, and (iv) calcination after intercalation of diethoxydimethylsilane for the formation of IPC-10.

#### 2.3.2.4 Reassembly

Condensation of the disassembled Si-rich layers can be realized by the calcination of precursors at 200 – 550 °C. In addition, the layers can also be condensed under high pressure. Noticeably, pressure-induced condensation of IPC-1P produces a fully crystalline IPC-2 under a pressure of 1 GPa at 200 °C, while IPC-4 is obtained at 550 °C under ambient pressure [95].

### 2.3.3 ADORable zeolites

The number of achievable structures from one parent zeolite by the ADOR approach is restricted because of the limited number of ways for connecting the rigid Si-rich layers. The set of products given by the ADOR approach can be increased, to some extent, by careful selection of the treatment conditions applied for the manipulation with the layer reassembly in the organization step [88]. Six different structures were already obtained by utilizing **UTL** as the parent zeolite (Table 2.1), nevertheless, those are not yet the full set of daughter zeolites predicted theoretically for this structure [96]. In addition, the starting materials used for synthesis of new zeolites achieved by ADOR protocols have been expanded to other germanosilicates, such as **UOV** (IPC-12) and ***CTH** (IPC-15 and IPC-16). Potentially, more

daughter zeolites can be produced from these parent materials if proper treatment conditions are applied.

Table 2.1 Overview of the new zeolites obtained in the ADOR approach.

| Parent zeolite | Daughter zeolite | Interlayer units in resulting zeolite | Reference |
|---|---|---|---|
| **UTL** | IPC-2 (**OKO**) | *s4r* | [86, 97] |
| | IPC-4 (**PCR**) | *O-bridge* | [86] |
| | IPC-6 (***PCS**) | *O-bridge/s4r* | [98] |
| | IPC-7 | *s4r/d4r* | [99] |
| | IPC-9 | *s4r* | [88] |
| | IPC-10 | *s4r* | [88] |
| **UOV** | IPC-12 | *O-bridge* | [100, 101] |
| ***CTH** | IPC-15 | *O-bridge* | [102] |
| | IPC-16 | *s4r* | [102] |

Up to now, 41 germanosilicates have been verified by the IZA structure committee. Except of the above mentioned germanosilicates, there are several germanosilicates which can be perspective parent zeolites used for new zeolite preparation in ADOR approach. Table 2.2 lists potential germanosilicates where they are divided into three categories based on the directions of location of *d4rs* (or other types of labile units such as *d3r*s, *s3r*s). Germanosilicates with 1D *d4r*s means that all the *d4r*s of this material are located in one plane and the silicate *layers* are connected by these *d4r*s; 2D means that the silicate *chains* are connected by the *d4r*s which are distributed in 2 dimensions; 3D means that the silicate *clusters* are connected by the *d4r*s oriented along all 3 dimensions. However, no successful transformation of these germanosilicates in ADOR approach was reported so far due to the particular features of their structures. For example, condensation of disassembled **IWW** layers obtained in acid solution results in the de-intercalation and reconstruction of the parent zeolite with a chemical composition different from that of the initial **IWW** zeolite but with the same structure [90]. Besides, poor stability of the respective 2D **IWR** layers results in degradation of structure during ADOR treatment [77, 103]. It should be noticed that the lability of the frameworks increases dramatically when the "dimensionality" of *d4r* location increases.

Degradation of zeolite frameworks, such as **SOV**, **ITT**, **IWS** etc., occurs after removal of SDA when exposure to ambient atmosphere [104, 105]. Therefore, careful selections of treatment conditions should be taken into consideration to avoid a collapse of structure after removal of SDA when manipulating the *d4r*.

Table 2.2 Selected ADORable parent zeolites, adopted from IZA database.

| Germanosilicate | Types of SBU | "Dimensionality" of d4r | Reference |
|---|---|---|---|
| **IWR** | *d4r* | 1D | [106] |
| **IWW** | *d4r* | 1D | [107] |
| **ITH** | *d4r* | 1D | [108] |
| **ITR** | *d4r* | 1D | [109] |
| **IWV** | *d4r* | 1D | [110] |
| **SOV** | *d4r* | 2D | [111] |
| **POS** | *d4r* | 2D | [112] |
| **UWY** | *d4r* | 2D | [113] |
| **IWS** | *d4r* | 3D | [114] |
| **ITT** | *d4r, s3r* | 3D | [81] |
| **IRR** | *d4r, d3r* | 3D | [82] |
| **BEC** | *d4r* | 3D | [78] |

## 2.4 Chemical flexibility of zeolites: isomorphous substitution by heteroatoms

Isomorphous substitution is the replacement of silicon atoms from the framework for other heteroatoms while maintaining the initial structure. Zeolite has been considered as crystalline microporous aluminosilicates for a long time [5]. Al has an ionic radius, bond angles (T–O–T) and bond lengths (T–O) close to those of Si, making it an ideal atom to isomorphously substitute the framework Si. Besides Al, other three or four valent elements, such as B, Ga, Ge, Sn, Ti, and Zr can also be introduced into the zeolite framework [78, 115-119]. This possibility is realized by altering the ''fine structure'' of the flexible frameworks (i.e. bond lengths and angles) to compensate the structural strains caused by the isomorphous

substitution [53]. Diversity of framework elements allows tailoring the nature of the generated Lewis and Brønsted acid centers for a catalytic purpose (Figure 2.20) [120]. Recent advances in zeolite synthesis enable to prepare zeolites with diverse structural flexibility. Both of direct hydrothermal synthesis and post-synthesis substitution were exploited for the incorporation of heteroelements into zeolite frameworks [53].

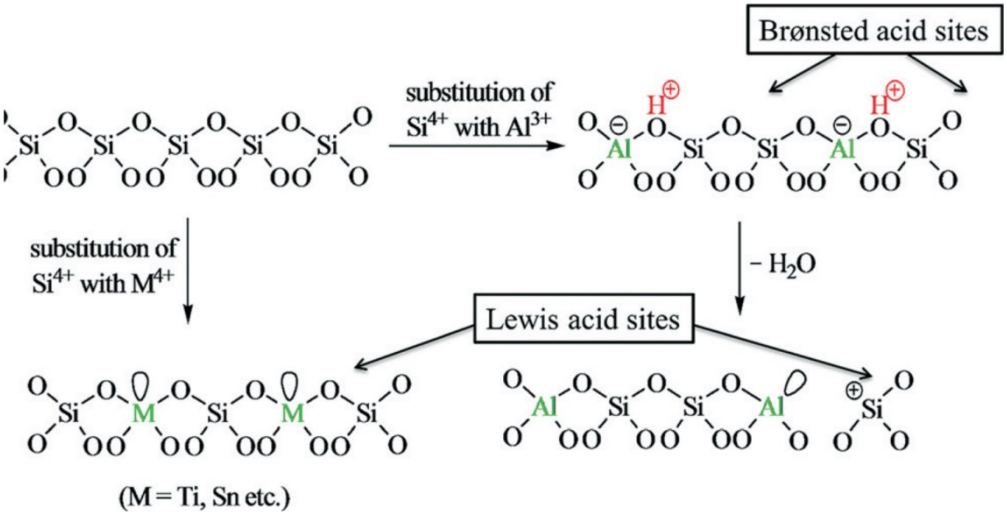


Figure 2.20 Schematic representations of Brønsted and Lewis acid sites in zeolite [120].

### 2.4.1 Substitution in the direct synthesis

Direct hydrothermal synthesis of zeolites with variable framework compositions is widely utilized for the chemical adjustment of particular properties in zeolites. Typically, the starting reaction gel is prepared by mixing the solvent, source of silica and heteroelement, inorganic and/or organic cations in $F^-$ or $OH^-$ medium. By manipulation with the parameters of reaction compositions and/or crystallization conditions, products containing heteroatoms in the zeolite frameworks can be synthesized [121, 122]. Besides, a significant impact of the synthesis methods on the kinetics of crystallization of heteroelement-containing zeolites was demonstrated. Awate *et al.* reported different kinetics for the crystallization of Sn-MFI synthesized by hydrothermal and dry gel conversion (DGC) methods [123]. Shorter induction period and faster crystallization was observed when DGC method was employed (7 h to get 100 % crystallinity at 170 °C) compared with the hydrothermal method (45 h under the same conditions). Moreover, a slightly lower activation barrier for nucleation (50 *vs.* 56 kJ $mol^{-1}$) and crystallization (53 *vs.* 60 kJ $mol^{-1}$) of Sn-MFI than that formed in the hydrothermal synthesis was shown.

### 2.4.2 Post-synthesis isomorphous substitution

As an alternative method to the direct synthesis, post-synthesis incorporation of T-atoms in zeolite framework with heteroelements can be realized by the insertion of heteroatoms into the position of "silanol nests". The latter is achieved upon removal of atoms (Si, Al, B, Ge, etc.) from zeolite framework by the treatment in neutral, acidic or alkaline solutions. Following incorporation of heteroelements can be done via gas-phase metalation or liquid-phase reaction condensation (Figure 2.21) [53]. Gas-phase metalation is performed by the treatment of a demetalated zeolite with a heteroelement precursor at high temperature [124]. For example, Sn-containing ***BEA** zeolite was prepared via two-step post-synthesis approach, involving the dealumination of ***BEA** zeolite in highly concentrated nitric acid solution (6 M) followed by the treatment with $SnCl_4$ vapour at 500 °C [125]. The content of Sn in the resulting samples is up to 6.2 wt%. In turn, liquid-phase method, i.e. impregnation, included the treatment of zeolites with a liquid source of heteroelements. Ti and Sn were grafted into **IWW** zeolites through the impregnation of degermanated **IWW** zeolites with $TiCl_4$ and $SnCl_4$ in organic solvent and $N_2$ atmosphere [126].

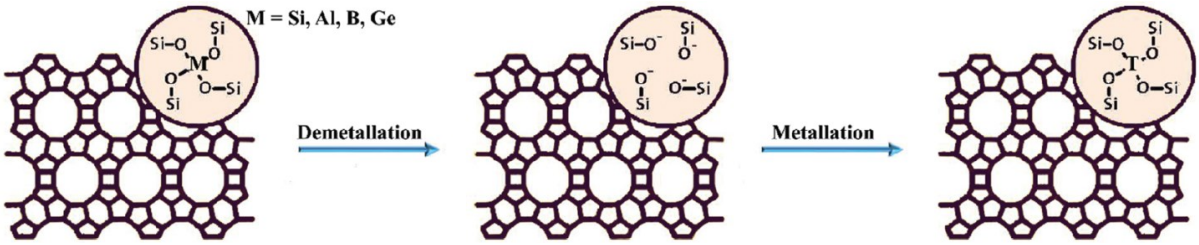


Figure 2.21 Schematic diagram of post-synthesis incorporation of heteroatoms into zeolites [53].

## 2.5 Gas separation of $CO_2/CH_4$ in zeolites

Carbon dioxide is an undesirable component in natural gas because it decreases the combustion efficiency and leads to pipeline corrosion under humid conditions [127, 128]. Selective removal of $CO_2$ from $CH_4$ is a necessary process to produce natural gas of high quality. Recently, the separation of $CO_2/CH_4$ by zeolites has attracted much attention due to their well-defined microporosity, high stability and chemical flexibility [129]. For the realization of selective adsorption of $CO_2$ over $CH_4$ on zeolites, kinetics and thermodynamics contributions are, generally, considered to be responsible [130]. Despite of small difference in kinetic diameters between $CO_2$ (3.3 Å) and $CH_4$ (3.8 Å), small pore zeolites with pore sizes

close to mentioned molecular dimensions can be applied to limit the diffusion of $CH_4$ in zeolites [131]. Regarding the thermodynamics contribution, the adsorbate–adsorbent interaction resulting from the quadrupole $CO_2$ is important for selective adsorption and uptake capacity [132-134]. In this respect, the nature of the adsorbent including its hydrophobicity/hydrophilicity [135, 136], chemical compositions [137, 138], and framework flexibility [139-141] can affect this interaction. In particular, the extra-framework cations in zeolites are demonstrated to not only appear as an adjustor of the pore size [142] but as a "molecular trapdoor" to influence the accessibility of supercavities [143, 144]. In addition, the type and distribution of the cations can have a significant impact on the adsorption properties [145, 146]. Except for the extra-framework cations, zeolite framework can also interact with the $CO_2$ molecules. For example, the framework of Cu-SSZ-13 was confirmed to be the preferred $CO_2$ adsorption sites rather than the extra-framework $Cu^{2+}$ cations [147]. In addition, isomorphously substituted aluminophosphate by Mg and Co atoms shows an enhanced selectivity of $CO_2$ over $CH_4$ and $N_2$ compared with its original form [148].

## 2.6 Zeolites studied in this work

### 2.6.1 Zeolite AST

The framework of **AST** zeolite is considered as a clathrate compound involving large [$4^6 6^{12}$] cages (**AST** units) connected by sharing the hexagonal faces, thereby forming smaller [$4^6$] cages (*d4r* units) between **AST** units (Figure 2.22). This typical arrangement directs the formation of a zeolite with the same amount of small and large cages.

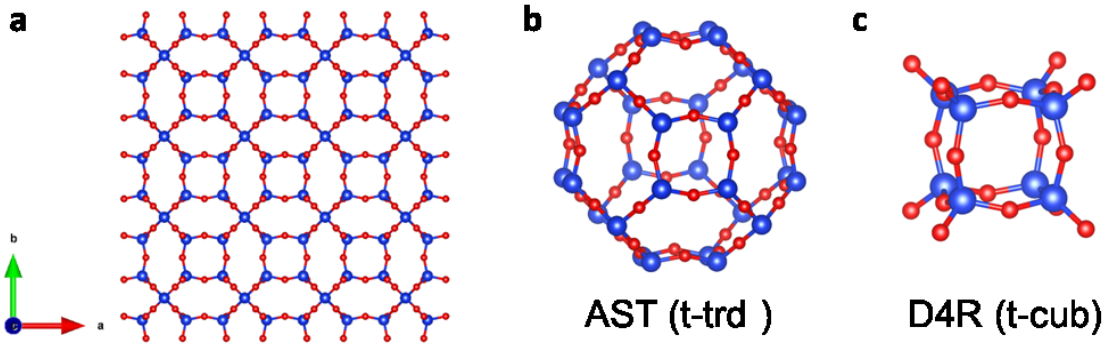


Figure 2.22 Structure of zeolite **AST** (a); *ast* cage (b); and *d4r* unit (c).

Zeolite **AST** was firstly synthesized as aluminophosphate ($AlPO_4$-16) and siliceous phase in 1991 [149, 150]. Later, pure germanate **AST** (AUS-9) was successfully prepared [151], and germanium can be partially substituted by silicon [152]. Synthesis of zeolite **AST** in germanate and purely siliceous forms often suggests the utilization of organic cation and $F^-$ anion in the reaction gel [149, 153-156]. Many OSDAs can direct the formation of AST phase, including quinuclidine [149], dimethyldiethylammonium [152], tert-butyltrimethylammonium [157], tetramethylammonium [158], and 4-methyl-2,3,6,7-tetrahydro-1H,5H-pirido[3,2,1-ij]-quinolin-ium [159]. Organic cations typically locate in the large cavity (*ast* unit), while fluoride anions are occluded in the *d4r* cages, both organic cation and $F^-$ anion can be removed by calcination at high temperature [155].

### 2.6.2 Zeolite CHA

**CHA** is a small-pore zeolite with 8-ring pore windows (3.8 × 3.8 Å, Figure 2.23). Zeolite **CHA** was widely applied to separate $CO_2$ (kinetic diameter: 3.30 Å) from $CH_4$ (3.80 Å) in the natural gas upgrading process because of suitable pore size comparable with that of mentioned gas molecules [160, 161]. Moreover, **CHA** zeolite has been proven to be an efficient catalyst for decomposition of nitrogen oxides after ion-exchanged with metal Cu [162]. Besides, SAPO-34 (**CHA** topology) has been reported as one of the active catalysts for the production of propylene and ethylene in the reaction of methanol-to-olefin (MTO) [163]. Furthermore, zeolite **CHA** contains only one crystallographic independent T site, making it a valuable model for the investigation of heteroatoms insertion into the framework [164].

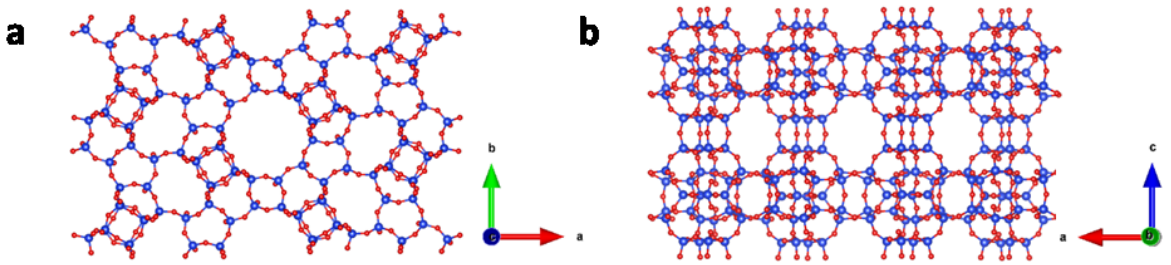


Figure 2.23 Structure of zeolite **CHA**, viewed in *axb* plane (a); *axc* plane (b).

Aluminosilicate **CHA** zeolite (commonly denoted as SSZ-13) can be synthesized in the presence of trimethyladamantylammonium hydroxide (TMAdaOH) in a broad range of Si/Al ratio. Besides, SSZ-13 can be prepared via the interzeolite conversion of **LTL** [165], **LTA** [166], **FAU** [167], and ***BEA** [168] in the presence of tetraethylammonium [169], TMAdaOH, and dimethylethylcyclohexyl ammonium [170]. In addition, it can be crystallized

using seeding method without OSDA, but the Si/Al ratio is less than 4 [171]. Compared with the aluminosilicate **CHA**, pure siliceous **CHA** can only be crystallized in the presence of both OSDA and $F^-$ ions in a very narrow range of water content [23].

### 2.6.3 ADORable germanosilicates: IWW and IWR

#### 2.6.3.1 Zeolite IWW

Zeolite **IWW** contains a 3D pore system with 8- (4.52 × 3.32 Å), and 12- (6.66 × 6.66 Å) ring channels along the [001] direction, both of which are intersected by a sinusoidal 10-ring channel (5.86 × 4.98 Å), as shown in Figure 2.24. **IWW** zeolite contains *d4r* units in 1D which connects the Si-rich layer along the *c* direction. Thus, under particular conditions in the ADOR process, the (00l) d-spacing can be decreased, while the XRD peaks corresponding to the (hk0) planes is nearly the same to the parent materials. **IWW** zeolite was firstly discovered as the germanosilicate ITQ-22 in 2003 [107] obtained using 1,5-bis-(methylpyrrolidinium)-pentane as OSDA. Later, both hexamethonium and 5-azoniaspiro[4,5]decane were found to be able to direct the formation of **IWW** zeolite [172, 173]. However, the final Si/Ge ratio of **IWW** zeolite prepared by these three OSDA is in the range 3 − 5 no matter what the initial amount of Ge feed used. Recently, Wu *et al.* reported **IWW** zeolite with Si/Ge = 1 can be prepared using 1,4-bis-(dimethyl-1-adamantylammonium)-butane as OSDA [174]. Despite of such a low Si/Ge ratio obtained in **IWW** zeolite, there exist 3 Si atoms per *d4r* evidenced by the $^{19}F$ MAS NMR spectroscopy, indicating some Ge atoms are located in the *layers* [89].

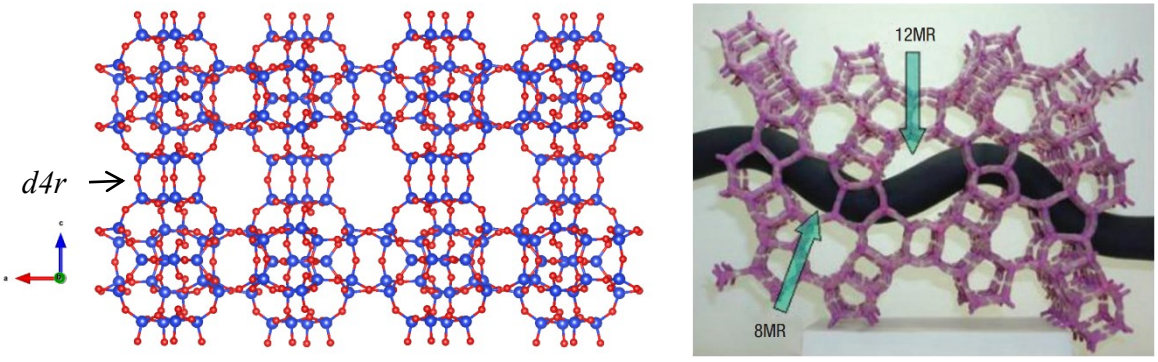


Figure 2.24 Structure of **IWW** zeolite: view in *axc* plane which shows the 1D *d4r* in *c* direction (left) and 3D pore system (viewed in *axb* plane) in which both of 8- and 10- rings are intersected by the sinusoidal 10-ring channel (right) [107].

### 2.6.3.2 Zeolite IWR

Zeolite **IWR** possesses a 3D pore system with intersecting 12- and 10-rings pores (as shown in Figure 2.25). Similar to the **IWW** zeolite, **IWR** zeolite contains 1D *d4r* units along the *c* direction, thus judgement about the success of disassembly and assembly is corresponding to the changes of (00l) XRD peak positions. **IWR** was initially synthesized as aluminogermanosilicate ITQ-24 using hexamethonium cation as an OSDA [106]. Recently, direct synthesis of aluminosilicate **IWR** zeolite was achieved using a new OSDA allowing get a stronger interaction between zeolite framework and organic molecules [175]. Besides Al-containing **IWR**, it is also possible to incorporate B into the **IWR** framework with a broad range of Si/Ge and B/(Si+Ge) ratios when F is introduced in the synthesis gel [176].

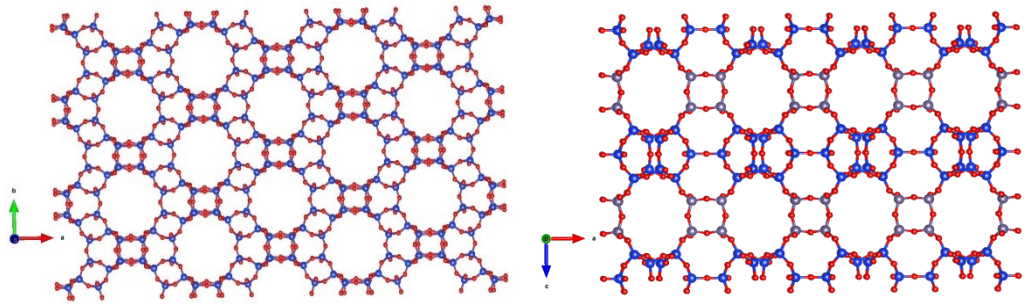

Figure 2.25 Structure of **IWR** zeolite: view in *axb* plane (left) and in *axb* plane (right). The T-atoms in *d4r* are shown in grey color.

The Ge atoms in **IWR** is also confirmed to be mainly located in the *d4r* units, similar to other germanosilicates. In addition, Ge also occupies T-atom positions in the Si-rich layers, especially at a low Si/Ge ratio [177]. The presence of Ge in both *d4r* and *layers* increases the hydrolytically instability of zeolite framework, which limits the application of ADOR for its structural transformation. As a result, a degradation of crystalline **IWR** (Si/Ge = 1.8) was observed when contact with water or acid solution [178].

# 3. Experimental part

## 3.1 Reagents and Solvents

| Chemicals | Quality | Company |
|---|---|---|
| 1,2-dimethylimidazole | 98 % | Sigma-Aldrich |
| 1,4-dibromobutane | 99 % | Sigma-Aldrich |
| 1,8-diazabicyclo[5.4.0]undec-7-ene | 98 % | Sigma-Aldrich |
| 1-adamantanamine | 98 % | Alfa Aesar |
| 1-methylimidazole | 99 % | Alfa Aesar |
| 2-(bromomethyl)naphthalene | 96 % | Sigma-Aldrich |
| 3-methylbenzyl chloride | 98 % | Alfa Aesar |
| 4-methylbenzyl chloride | 98 % | Sigma-Aldrich |
| aluminium hydroxide | | Acros Organic |
| cis-2,6-dimethylpiperidine | 98 % | Sigma-Aldrich |
| decamethonium bromide | 98 % | TCI Chemical |
| diethyl ether | 99.9 % | Lachner |
| diethyldimethylammonium hydroxide solution | 20 % in $H_2O$ | Sigma-Aldrich |
| ethyl acetate | P.A. | Penta |
| fumed silica | / | Sigma-Aldrich |
| gallium(III) nitrate hydrate | 99.9 % | Sigma-Aldrich |
| germanium oxide | 99.99 % | Acros Organic |
| glass microfiber filter | / | Whatman™ |
| hexamethonium bromide | 99 % | Sigma-Aldrich |
| hydrobromic acid | 99.99% | Sigma-Aldrich |
| hydrochloric acid | 37 % | Sigma-Aldrich |
| hydrofluoric acid | 48 % | VWR Chemical |
| hydroiodic acid | 99.99 % | Sigma-Aldrich |
| ortho-boric acid | 100 % | VWR Chemical |
| sodium hydroxide | 98 % | Penta |
| titanium (IV) ethoxide | / | Acros Organic |
| trimethyladamantammonium hydroxide solution | 20.35 % in $H_2O$ | SACHEM |

## 3.2 Synthesis of zeolites

### 3.2.1 Zeolite AST

Zeolite **AST** was prepared using diethyldimethylammonium hydroxide (DEDMAOH) as the SDA. Typically, HF was slowly added into the solution of DEDMAOH under stirring with further introduction of freshly prepared fumed silica solution (10 wt% in $H_2O$). The resulting mixture was stirred overnight under ambient conditions followed by the evaporation of the excess of water in the oven (at 60 °C). Once reaching the required composition (1 $SiO_2$: *x* DEDMAOH: *x* HF: 4 $H_2O$, *x* = 0.3 ~ 0.7), the reaction mixture was treated at 170 °C for 1 ~ 14 days under agitation. The final products were recovered by filtration, washed sequentially with water and ethanol, and dried at 60 °C.

When adding additional $NH_4F$ or HX (X = Cl, Br, I), the composition of reaction mixture was 1 $SiO_2$: *x* DEDMAOH: *x* HF: 0.2 $NH_4F$: 4 $H_2O$, or 1 $SiO_2$: (*x* + 0.2) DEDMAOH: *x* HF: 0.2 HX: 4 $H_2O$. For the typical procedure, $NH_4F$ or HX was added to the mixture of DEDMAOH and HF, and then follow the same procedure as described above.

### 3.2.2 Zeolite CHA

#### 3.2.2.1 Pure Si-CHA

Si-CHA zeolite was prepared with a composition of 1 $SiO_2$: 0.5 TMAdaOH: 0.5 HF: 3 $H_2O$ [179]. Tetraethyl orthosilicate (TEOS) was hydrolyzed in the TMAdaOH solution under stirring at ambient conditions. In order to evaporate the excess of the water, the gel can be transferred to the oven (60 °C) when it cannot be mixed using magnetic stirrer. Then, the formed solid-like mixture was grinded to fine powder, followed by addition of HF and secondary grinding. Finally, the crystallization proceeded at 150 °C for 2 days with rotation. Final solid products were recovered by centrifugation, washed sequentially with water and ethanol, and calcined at 600 °C for 6 h under air flow.

#### 3.2.2.2 Synthesis of M-CHA, M = Al, B, Ga

Aluminium hydroxide, ortho-boric acid, gallium(III) nitrate hydrate were used as Al, B and Ga sources, respectively.

Al-substituted H-form **CHA** (Al-CHA) was prepared by the crystallization of the reaction mixture (1 $SiO_2$: 0.5 TMAdaOH: 0.05 $AlO_{1.5}$: 44 $H_2O$) at 150 °C for 1 day. $Al(OH)_3$

was firstly dissolved in SDA solution followed by the addition of colloidal silica. Once reaching the required composition, a specified amount (2 wt% of $SiO_2$) of Si-CHA was introduced into the mixture. Subsequently, the mixture was hydrothermally heated at 150 °C for 1 day.

B- and Ga-substituted H-form **CHA** (B-, and Ga-CHA) were synthesized using the reaction mixture with a composition of 1 $SiO_2$: 0.4 TMAdaOH: $x$ $MO_{1.5}$: 44 $H_2O$ ($x$ = 0.2 for $BO_{1.5}$, 0.05 for $GaO_{1.5}$). The synthesis proceeded with the same procedure as Al-CHA but using fumed silica as the silica source instead of colloidal silica, and crystallized for 1 and 3 days for B-CHA and Ga-CHA, respectively.

The final M-CHA products were collected by centrifugation, washed sequentially with water and ethanol, dried at 60 °C, and calcined at 600 °C for 6 h with 1 °C $min^{-1}$.

#### 3.2.2.3 Synthesis of Ti-CHA

Titanium ethoxide was used as the Ti source for the preparation of Ti-CHA, which can be crystallized from the mixture with a composition of 1 $SiO_2$: 0.05 $TiO_2$: 1.4 TMAdaOH: 1.4 HF: 6 $H_2O$. Typically, titanium ethoxide was firstly mixed with the solution of SDA. Subsequently, colloidal silica was introduced with additional stirring overnight under ambient conditions followed by the addition of HF. Once the required composition was achieved, a certain mass (2 wt% of $SiO_2$) of Si-CHA was added under stirring with further heating at 150 °C for 30 h.

### 3.2.3 Zeolite UTL

#### 3.2.3.1 Synthesis of (6R, 10S)-6,10-dimethyl-5-anizoporo[4.5]decane hydroxide (DMADH)

SDA for **UTL** synthesis (Figure 3.1) was prepared under alkaline conditions based on ref. [180]. Typically, 8.52 g of solid NaOH was dissolved in 210 g of water to prepare ~ 1 M NaOH solution followed by the addition of 1,4-dibromobutane (45.99 g). After heating up to ~ 75 °C, (2R, 6S)-2,6-dimethylpiperidine (24.11 g) was added drop-by-drop under vigorous stirring. Then, the reaction mixture was stirred at 100 °C until the homogeneous solution formed. After that, the flask was placed into the ice batch to cool down the solution followed by the addition of solid NaOH until forming the oily products. Solid products were recovered through crystallization, filtration, and extraction with chloroform. The resulting solution

(SDA dissolved in chloroform) was mixed with anhydrous $Na_2SO_4$ powder to remove the remaining traces of water. Finally, the solid SDA was obtained after filtration, evaporation of chloroform and washing with diethyl ether.

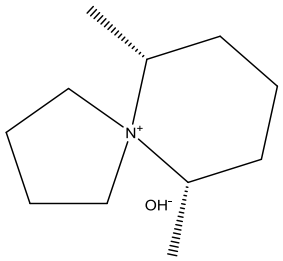


Figure 3.1 SDA used for **UTL**, (6R,10S)-6,10-dimethyl-5-azoniaspiro-[4.5]decane hydroxide.

### 3.2.3.2 Synthesis of zeolite UTL

**UTL** zeolite was synthesized by the crystallization of the reaction mixture (0.8 $SiO_2$: 0.4 $GeO_2$: 0.4 DMDAH: 30 $H_2O$) at 175 °C for 7 days with rotation ref. [181]. Typically, the bromide form of SDA was ion-exchanged into OH form using Ambersep® 900(OH) anion exchange resin (8 mmol SDA/g resin). After filtration, washed with deionized water and dried overnight at 60 °C, the as-synthesized **UTL** samples were calcined at 550 °C for 6 h.

### 3.2.4 Zeolite IWW

### 3.2.4.1 Synthesis of 1,5-bis-(methylpyrrolidinium)-pentane dihydroxide – $MPP(OH)_2$

SDA for **IWW** synthesis (Figure 3.2) was prepared according to ref. [107]. N-methylpyrrolidine (30 g) and 1,5-dibromopentane (28.2 g) were added into the acetone (225 ml), the mixture was refluxed at 55 °C overnight. Obtained solid products were separated by filtration and washed with acetone.

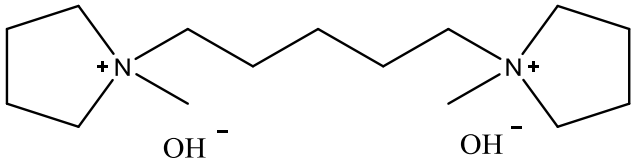


Figure 3.2 SDA used for synthesis of **IWW**, 1,5-bis-(methylpyrrolidinium)-pentane dihydroxide.

### 3.2.4.2 Synthesis of IWW

SDA in hydroxide form $MPP(OH)_2$ was used for the synthesis of **IWW** zeolites according to the ref. [107]. Typically, $GeO_2$ was dissolved in SDA solution with further

addition of Si source (TEOS). The mixture was stirred for several hours to evaporate ethanol/water, then the resulting mixture with required composition (0.66 $SiO_2$: 0.33 $GeO_2$: 0.25 $MPP(OH)_2$: 15 $H_2O$) was heated at 175 °C under static for 11 days. **IWW** samples were recovered by filtration, washed sequentially with water and ethanol, dried at 60 °C and calcined at 580 °C for 6 h.

### 3.2.5 Zeolite UOV

DMDH (Figure 3.3) was used as SDA for the synthesis of **UOV** based on ref. [101]. Firstly, OH form of SDA (~ 1.5 M) was obtained after the ion-exchange of bromide form of SDA and appropriate concentration of resulting solution was achieved by evaporation of the excess of the water. Then, required amount of $GeO_2$ was dissolved in SDA solution with further addition of fumed silica under stirring. After that, the resulting gels a composition of ($x$ $SiO_2$: $(1 - x)$ $GeO_2$: 0.25 DMDH: $y$ $H_2O$, $x$ = 0.33 ~ 0.66, $y$ = 5 or 10) were crystallized at 175 °C under static conditions for 7 ~ 14 days. The final product was separated by centrifugation, washed distilled water, dried overnight at 60 °C and calcined at 550 °C in air flow for 6 h.

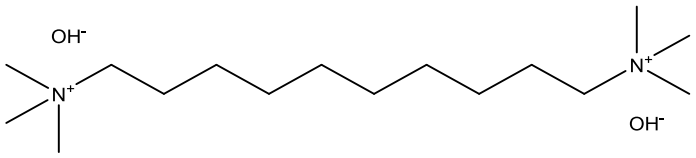


Figure 3.3 SDA used for synthesis of **UOV**, decamethonium dihydroxide.

### 3.2.6 Zeolite IWR

#### 3.2.6.1 Synthesis of B-containing IWR (OH form and F form)

B-containing **IWR** was synthesized using hexamethonium dihydroxide (HMIDH) as SDA1 (Figure 3.4) according to ref. [106]. The composition of the starting gel for the synthesis of B-containing **IWR** was set as: $(1 - x)$ $SiO_2$: $x$ $GeO_2$: $(0.05 - 0.1)$ $BO_{1.5}$: 0.225 HMH: $y$ HF: 5 $H_2O$, where $x$ = 0.33 or 0.17, $y$ = 0 or 0.1. The bromide form of SDA was firstly ion exchanged into OH form using Ambersep® 900(OH) anion resin. For the typical procedure of the synthesis, $GeO_2$ was dissolved in HMIDH solution with further addition of TEOS under stirring at ambient temperature. For the F form **IWR**, after thorough evaporation of ethanol and the excess of the water, HF was added into gel further homogenized by stirring. Subsequently, the crystallization was carried out at 175 °C with rotation for 10 days. The

resulting products were collected by filtration, washed with deionized water, dried overnight at 60 °C and further calcined at 550 °C for 6 h.

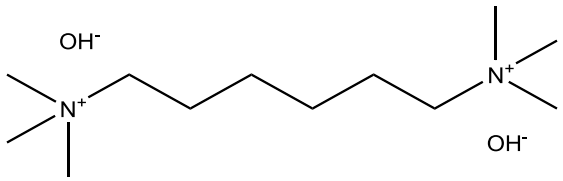


Figure 3.4 SDA1 used for synthesis of IWR, hexamethonium dihydroxide.

### 3.2.6.2 Synthesis of B-free IWR

The obtained B-containing **IWR** samples were used as crystal seeds for the synthesis of B-depleted **IWR** in the B-free reaction mixture. The starting gel composition was the same as for the B-containing **IWR** except the presence of additional B-containing **IWR** seeds (10 wt% $SiO_2$) and the absence of B.

### 3.2.6.3 Synthesis of IWR(SDA2)

Germanosilicate **IWR** was synthesized using 1,8-diazabicyclo[5.4.0]undec-7-ene (DBU) as SDA2 (Figure 3.5), the reaction mixture with a composition of 1.0 $SiO_2$: 0.5 $GeO_2$: 1.5 DBU: 7 $H_2O$ was heated at 170 °C for 7 days with rotation [182]. In a typical synthesis, 3.8 g DBU was firstly added into 6.3 ml water, followed by the dissolving of 2.6 g $GeO_2$ in the mixture. Then, 3.0 g fumed silica was introduced into the solution with further stirring until a homogeneous gel was formed. The synthesis mixture was crystallized at 170 °C under static conditions for 7 days. Once the crystallization was finished, **IWR** product was collected by filtration, washed with water and then dried overnight at 60 °C. As-synthesized samples were calcined at 550 °C for 6 h in air flow, the final sample was denoted as IWR(SDA2).

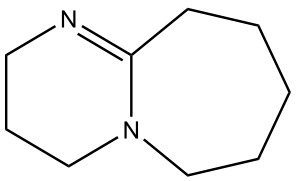


Figure 3.5 SDA2 used for synthesis of **IWR** seeds, 1,8-diazabicyclo[5.4.0]undec-7-ene.

### 3.2.6.4 Synthesis of IWR(SDA1)

For synthesis of IWR(SDA1), IWR(SDA2) was used as crystal seeds in the presence of SDA1. The initial gel composition was set as 0.66 $SiO_2$: 0.33 $GeO_2$: 0.225 HMI: 5 $H_2O$

with IWR(SDA2) seeds (10 wt% of seeds/$SiO_2$). The rest procedures for preparation IWR(SDA1) were the same.

## 3.3 Post treatment of the germanosilicate zeolites

### 3.3.1 Hydrolysis in acidic solution

The calcined germanosilicate zeolites were added into 0.1 ~ 12 M HCl solution (w/v, 10 %) and stirred at selected temperature. After the reaction, the products were separated by filtration and washed with anhydrous ethanol. Finally, the hydrolyzed precursors were dried at 60 °C.

### 3.3.2 Vapour-phase-transport method

Calcined zeolite samples (100 mg) were placed on the borosilicate glass filter membrane (or PTFE membrane) and then in the reactor (Figure 3.6) over HCl solution (12 M, 10 ml), the reaction was preceded at 25 °C for 5 min ~ 48 h. After that, the solid was taken out and transferred to the hood to release the traces of HCl. The obtained samples were further placed in the crucible and heated up to 250 ~ 450 °C for 2 h.

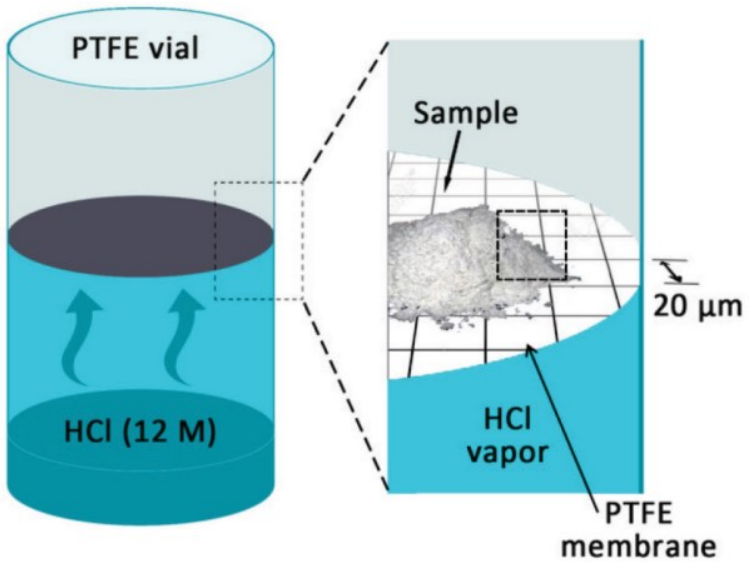


Figure 3.6 Scheme of treatment of **IWW** germanosilicate on PTFE filter.

## 3.4 Characterization

### Basic characterization

The phase and crystallinity of zeolite was examined with X-ray powder diffraction (XRD), which was measured with a Bruker AXS-D8 Advance diffractometer via Cu Kα radiation (λ =1.58416 Å, 40 kV, 30 mA). Before the detection, zeolite sample was evenly ground and placed into the holder.

$N_2$ and Ar sorption isotherms were measured at liquid nitrogen (−196 °C) and argon (−186 °C) temperature with 3Flex (Micromeritics) static volumetric apparatus. A turbo molecular pump was employed to outgas a specified amount of zeolite samples under vacuum for 8 h at 250 °C prior to the measurements.

Scanning electron microscopy (SEM, FEI Quanta 200F) was employed to perform the morphological characterization of zeolite crystals.

High-resolution transmission electron microscopy (HRTEM) was carried out on JEOL NEOARM 200 F microscope at 200 kV equipped with a field emission gun (Schottky-type).

Inductively Coupled Plasma Optical Emission Spectroscopy (ICP-OES, ThermoScientific iCAP 7000) was used to determine the contents of Si, Ge, Ti, Al, B, Ga in zeolite samples. Before measurements, a certain amount (~ 50 mg) of sample was dissolved in a mixture of acids (HF: 1.8 ml, $HNO_3$: 1.8 ml, HCl: 5.4 ml) followed by the complexation of residual HF with saturated $H_3BO_3$ solution.

Bruker Advance III HD spectrometer ($B_o$ = 9.4 T) was used to collect the $^{11}B$ NMR spectra ($\nu_L$ = 192.4 MHz). Prior to measurements, zeolite samples were placed in a zirconia rotor (3.2 mm, 22 µl) and spun at a rate of 15 kHz in a Bruker 3.2 mm HX CP-MAS probe. The spectra were referenced to 0.1 M $H_3BO_3$.

Diffuse Reflectance ultraviolet-visible (DR UV-vis) spectra (190 ~ 600 nm) were recorded on a Cary 300 spectrophotometer.

### Nano X-ray tomography for AST zeolite (Section 4.1)

A high-resolution full-field X-ray transmission microscope Nano-XCT-100 (Xradia Inc., Pleasanton, CA, USA) was used for the 2D and 3D imaging in Zernike contrast (phase contrast) [183]. The FZP was applied for overview imaging in standard mode (10x FZP magnification x 20x optical magnification = 200x total magnification) with pixel size

configurations 65 nm (camera binning 1) to 130 nm (camera binning 2) at 65 µm x 65µm field of view (FOV). For stable imaging, samples were fixed with superglue (Gorilla Glue, Inc., Cincinnati, OH, USA) on a stainless-steel needle. The data acquisition of the four tomographies over 180° tilt angle was performed with following imaging parameters: b) 601 projections, 100 s per each, camera binning 2 (512px x 512px); c) 801 projections, 210 s per each, camera binning 1 (1024px x 1024px), d) 801 projections, 110 s per each, camera binning 1; e) 401 projections, 120 s per each, camera binning 2.

**FTIR experiments for determination of acidity of M-CHA (Section 4.3.1)**

The nature and acidity of Lewis and Brønsted acid sites (LAS and BAS) was determined by Fourier-transform infrared (FTIR) spectroscopy, which was carried out on a Nicolet iS50 spectrometer equipped with a transmission MTC/B detector. Before the measurements, a prepared self-supporting wafer (density: ~ 10 mg $cm^{-2}$) of zeolite samples was outgassed under vacuum for 4 h at 450 °C. All spectra were recorded by 128 scans with 4 $cm^{-1}$ resolution under ambient conditions.

**XRD refinement for M-CHA (Section 4.3.2)**

Powder X-ray diffraction (PXRD) patterns were collected using a STOE STADI-P diffractometer in Debye-Scherrer mode ($Cu_{K\alpha1}$ radiation, $\lambda$ = 1.5406 Å), in the range 5-70° 2θ. Samples were packed into glass capillaries (inner diameter 0.7 mm) and a PXRD pattern collected (hydrated M-CHA). The samples in the capillaries were then dehydrated at 575 K for 24 hours under a vacuum of $9\times10^{-4}$ mbar. The capillaries were sealed immediately and a PXRD pattern collected (dehydrated M-CHA).

The obtained PXRD patterns were initially refined using a Le Bail refinement, fitting in the range 7-70° 2θ, employing a manual background and a pseudo-Voigt peak shape. Subsequent Rietveld refinement was performed for M-CHA-d samples (suffix -d indicating dehydrated sample). The refinement was first conducted using geometric restraints for T−O (1.60 ± 0.02 Å) as well as O−O (2.60 ± 0.02 Å) distances, which were later removed as the refinement progressed. The atomic displacement parameters (ADP) for the oxygen atoms were refined isotropically and its value restricted to be equal for all four oxygen atoms. Both position and ADPs of silicon and the heteroatom were restricted to be equal. The occupancy of the heteroatom was kept constant to the value derived from elemental analysis (B-CHA was set as 0.9 Si and 0.1 B). All refinements were performed using the software JANA2020,

the successor to JANA2006. [184] Details for all refinements and plots can be found in the Table 1-4, Appendix I.

**Adsorption evaluation for M-CHA (section 4.3.2)**

The adsorption measurements of $CO_2$ and $CH_4$ on M-CHA materials were carried out using an ASAP 2020 Plus manometric/volumetric equipment (Micromeritics, USA) at temperatures in range from 273 to 298 K up to 800 Torr of equilibrium pressure. The temperature of sample was controlled by a Peltier thermostat with a Pt sensor (temperature control accuracy ± 0.1 K). Before the experiments, all samples (ca. 75 mg) were treated at 623 K for 8 hours under dynamic vacuum. Methane of 99.997 % and carbon dioxide of 99.9996 % purity provided by Linde, a.s. were used for the measurements without further purification.

The adsorption selectivity for a binary mixture is defined as:

$$\alpha_{1,2} = \frac{x_1/y_1}{x_2/y_2}$$

where $x_1$ and $x_2$ are the molar fractions of the compound 1 and 2 in the adsorbed phase and $y_1$ and $y_2$ are the molar fractions of the compound 1 and 2 in the gas phase. The values $x_1$ and $x_2$ were predicted by the ideal adsorbed solution theory (IAST) [185] using Tóth adsorption isotherm to fit the measured data:

$$n_{ads} = n_m \frac{bp}{[(1+bp)^t]^{1/t}}$$

where $n_{ads}$ is the adsorbed amount [mmol $g^{-1}$], $n_m$ is the maximum adsorption capacity [mmol $g^{-1}$], b is the adsorption coefficient [$torr^{-1}$], p is equilibrium pressure and t is an empirical constant [-]. As it is impossible to find a solution in the closed form when using Tóth isotherm with IAST, our own custom coded algorithm for Scilab was used to numerically obtain the solutions.

**FTIR experiments for M-CHA (section 4.3.2)**

Interaction between the adsorbed $CO_2$ and M-CHA was evaluated using Fourier-transform infrared spectroscopy (FTIR) by dosing small amounts of $CO_2$ into the IR cell at room temperature. Spectra were recorded in transmission mode using Nicolet iS50 spectrometer equipped with a MCT/D detector with a spectral resolution of 1 $cm^{-1}$ by

accumulation of 32 scans for equilibrium and 4 scans for desorption measurements. KBr wafers with density of $\sim$ 40 mg $cm^{-2}$ were prepared, on whose surface small amount of each sample was dispersed and fixed ($\sim$ 2 mg). Samples were activated *in situ* by slow heating (5 K $min^{-1}$) to $T = 573$ K and $p = 5\times10^{-5}$ Torr for 4 hours. Adsorption equilibrium was measured under equilibrium pressures up to 8 Torr via step-by-step increasing pressure with the equilibration of each dose for at least 20 min. After reaching a pressure of 8 Torr and measuring the equilibrium data, the sample was subjected to continuous evacuation by a turbomolecular pump. Desorption kinetics would be monitored by a decrease in the intensity of vibrational bands of adsorbed $CO_2$ by measuring time-resolved IR spectra.

# 4. Results and discussion

For the clarity of the further reading, the structure of the discussion devoted to the different aspects of zeolite chemistry can be schematically illustrated by the following scheme:

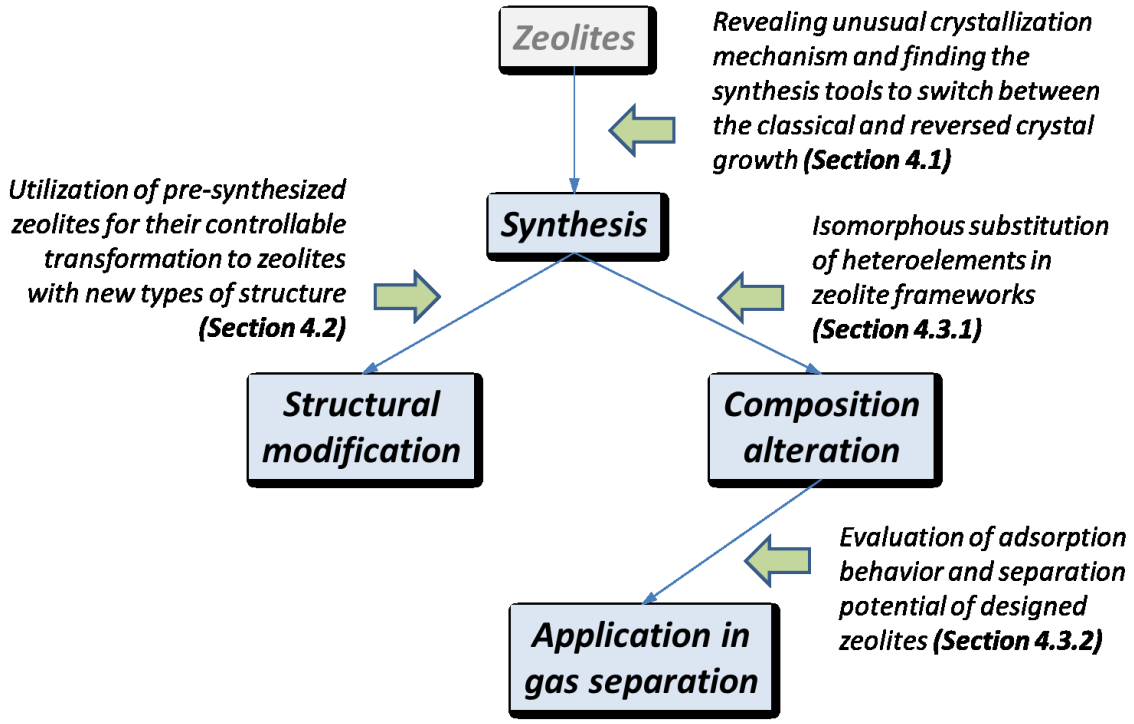


## 4.1 Controllable crystallization mechanism: the classical and reversed crystal growth

In this section, we present a model synthesis system evolving via reversed zeolite crystal growth, in which crystallization starts at the surface of amorphous aggregates. This initial step allows to "switch" the crystal growth modes between classical and reversed routes based on the interplay between inorganic and organic components under particular synthesis conditions. Zeolite **AST** was used to study the aggregation/growth mechanism due to a wide range of conditions (composition of reaction mixture and duration of hydrothermal treatment) suitable for its synthesis. Adjusting SDA/$SiO_2$ and $F^-/SiO_2$ ratios in the zeolite **AST** synthesis mixture revealed the fundamental function of SDA controlling the crystallization pathway, while the concentration of $F^-$ determines the rate of crystal growth. The type of mechanism and details of inner structure of intermediate particles were confirmed by comprehensive electron microscopy studies on aliquots taken at several synthesis times. Furthermore, the

internal crystallinity development of large aggregates (~ 60 μm) in the reversed crystal growth was visualized by nano X-ray tomography for the first time.

### 4.1.1 Between the classical and reversed crystal growth

Zeolite **AST** was synthesized with a gel composition of 1 $SiO_2$: *x* DEDMAOH: *x* HF: 4 $H_2O$ (*x* = 0.15 – 1) for 1 − 14 days. When $x < 0.3$ (*e.g.* $x = 0.15$), only an amorphous phase can be obtained, while at $x > 0.7$ (*e.g.* $x = 1$) a pre-**FER** phase is present (Figure 4.1). For all samples synthesized at $x = 0.3 – 0.7$, only **AST** zeolite phase was detected on XRD patterns (Figure 4.1). This range was used for the following studies. With the variation of *x*, the zeolite **AST** crystallization mechanism can be controlled. At low *x* values ($0.3 \leq x \leq 0.4$) the crystal growth follows the classical route, while at high values ($0.5 \leq x \leq 0.7$) it switches to the reversed crystal growth mechanism.

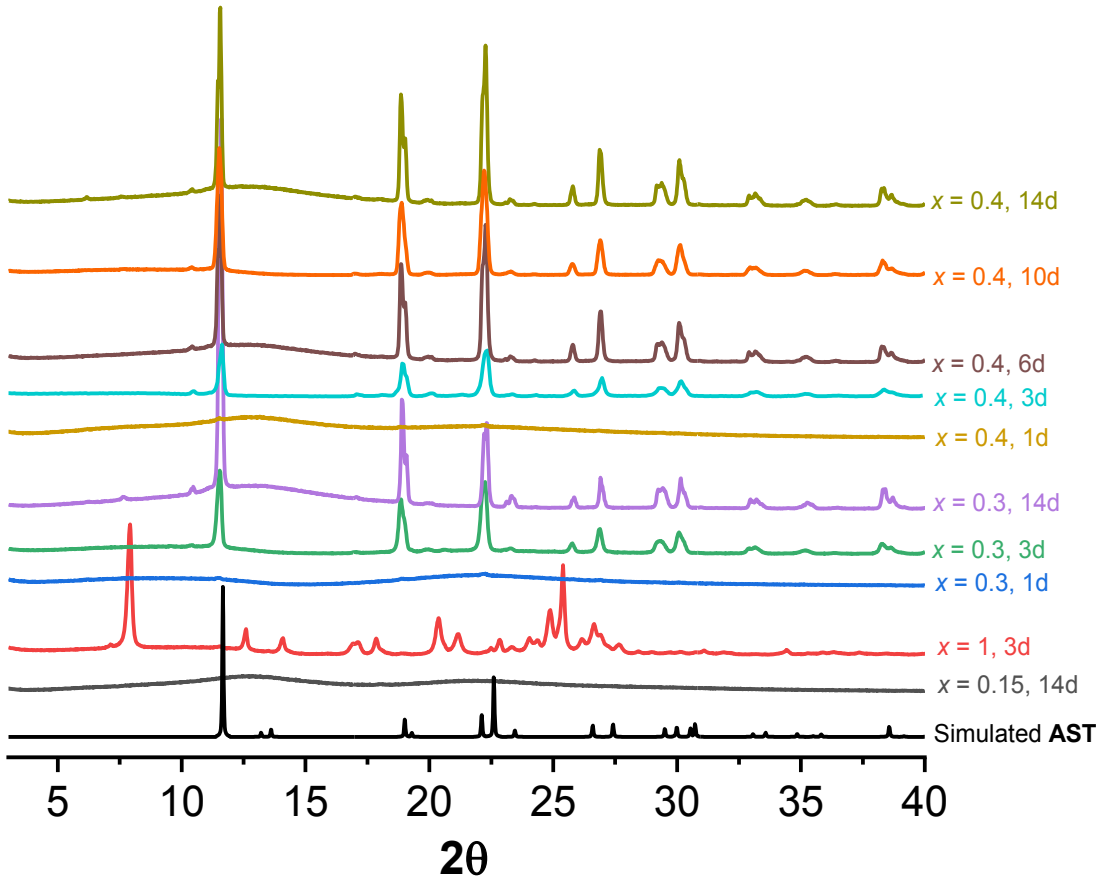


Figure 4.1 XRD patterns of samples prepared with variable *x* for specific time. The synthesis gel composition is 1 $SiO_2$: *x* DEDMAOH: *x* HF: 4 $H_2O$ (*x* = 0.15 – 1). When *x* = 0.15, no crystalline material can be obtained in 14 days, while a pre-**FER** phase was obtained in 3 days when *x* increase to 1. Zeolite **AST** is obtained with x = 0.3 – 0.7.

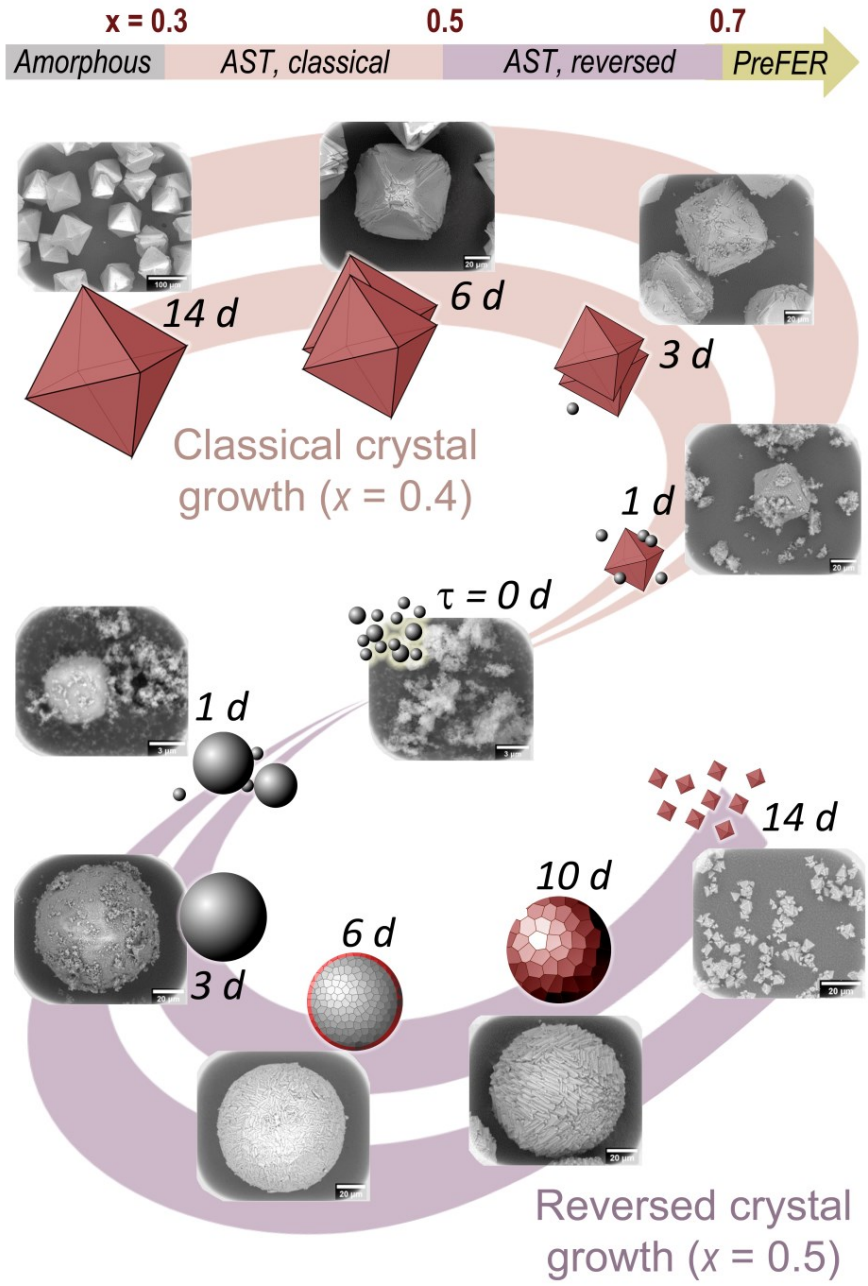


Figure 4.2 Switchable crystallization mechanisms of zeolite **AST** between the classical and reversed crystal growth. Amorphous phase is shown with grey color, crystalline with burgundy.

As a representative case of classical mechanism at $x$ = 0.4 (Figure 4.2), the zeolite **AST** phase (as incomplete octahedral ~ 50 μm particles) was observed already in 1 day, together with a large amount of amorphous phase. At the same time, **AST** crystallites were also observed in the transmission electron microscope (TEM), indicating the crystallization has already started in the system (Figure 4.3). Further growth of **AST** crystals proceeds through the consumption of the amorphous precursor. A pure **AST** phase, presented as octahedral crystals defective on their edges and vertexes, can be obtained in 6 days. These

defects are probably caused by the insufficient rate of crystallization as they can be healed through Ostwald ripening when prolonging the synthesis time. As a result, well-shaped octahedral crystals (~ 90 μm) were formed in 14 days. The decrease in $x$ leads to similar outputs with exception of much slower kinetics at the same stages (appearance of small crystals, complete crystallization, defects healing), which require longer synthesis time (Figure 4.4). This result indicates the importance of the concentration of participating species (SDA and HF) for overall crystallization rate.

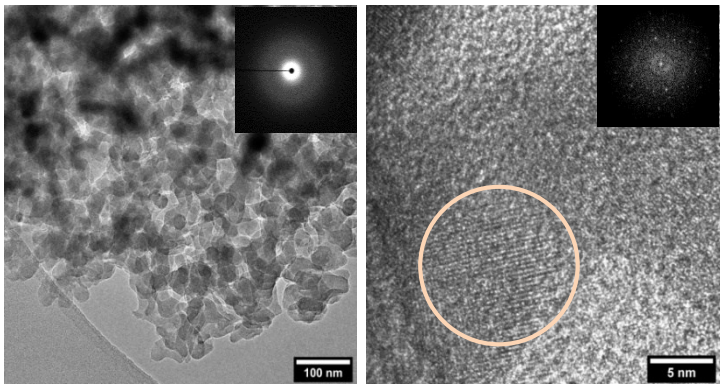


Figure 4.3 TEM images of sample ($x$ = 0.4) obtained in 1 day. (left) A large number of small amorphous particles are presented (SAED image is inserted). (right) A small number of zeolite **AST** crystallites (inserted FFT image).

Reversed crystal growth ($0.5 \leq x \leq 0.7$) involves two steps: aggregation and crystallization [67]. At the very early stage before crystallization starts, the synthesis precursors agglomerate together to form amorphous aggregates. When entering to the second step, contrary to the classical route, the crystallization starts at the surface towards the center of the amorphous aggregates. Synthesis system at $x$ = 0.5 can be taken as an illustrative example (Figure 4.2). Firstly, amorphous spherical particles with a diameter of ~ 5 μm were observed in 1 day together with a large number of small precursor particles (< 1 μm). With prolongation of the synthesis time, spherical particles grow at the expense of smaller particles (Ostwald ripening) without crystallization. After 3 days the spherical particles reach their maximal size (~ 80 μm), while the fraction of small species become negligible. Resulting large spherical particles have a very low crystallinity as confirmed by XRD (Figure 4.1) being the aggregates of amorphous precursors formed at the very early stages of crystallization. After 6 days the surface of the spherical particles become rough and the features (facets) of octahedral crystals with a size range of ~ 4 μm appear.

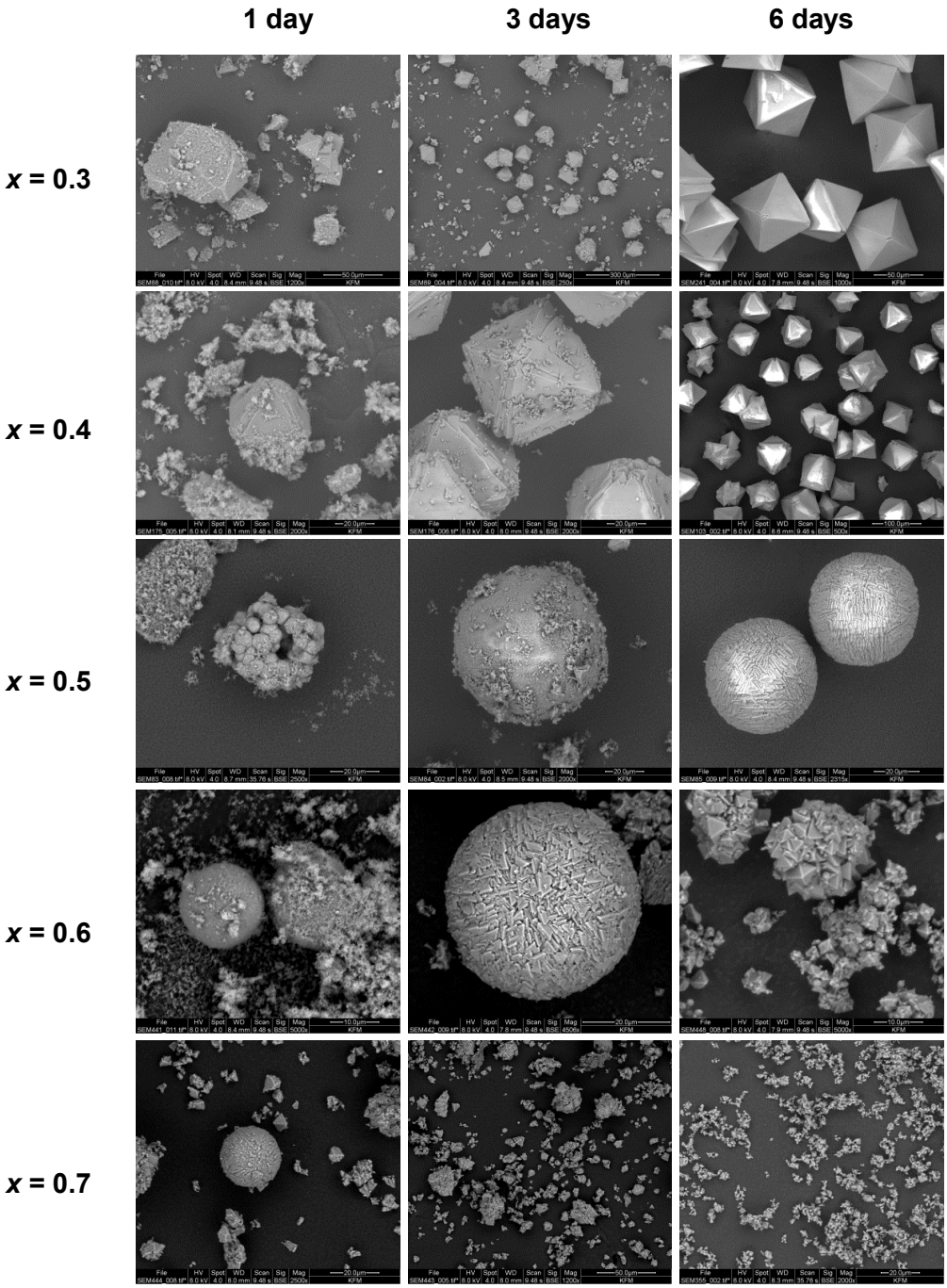


Figure 4.4 The effect of variable x (both SDA and F) on the crystallization pathway and crystal growth rate. At low *x* values ($0.3 \leq x \leq 0.4$) the crystal growth follows the classical route, while at high values ($0.5 \leq x \leq 0.7$) it switches to the reversed crystal growth mechanism. In general, the crystal growth accelerates with an increase of the *x* value, no matter which crystallization pathway the system goes.

Further prolongation of the synthesis (10 days) results in the increased surface roughness due to the growth of crystallites. Crystallization of the amorphous phase results in an increased material density that leads to a partial disintegration of spherical aggregates when the octahedral crystallites continue to grow (Figure 4.5). Finally, small octahedral

crystals were obtained in 14 days as a result of total collapse of aggregates accompanied by complete crystallization. Both the rate of aggregation and crystallization steps is accelerated when *x* increases to 0.6 and further to 0.7 (Figure 4.4). Despite of the accelerated agglomeration, the size of amorphous aggregates decreases from 80 to 25 μm. In addition, the formation of octahedral **AST** crystals (typical for the final crystallization steps) was detected at an earlier time with the increase in *x*. These results suggest that aggregation and crystallization are two competitive processes in the reverse crystal growth pathway [65]. In general, the crystal growth accelerates with an increase in the *x* value, independently of the crystallization pathway.

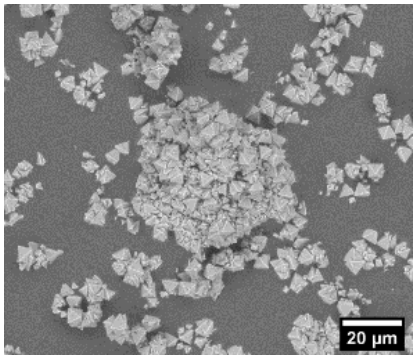


Figure 4.5 SEM image of the remaining agglomerated octahedral **AST** crystals before complete collapse during the reversed crystal growth.

### 4.1.2 Structure of the intermediate particles formed in the reversed crystal growth

Based on the estimation done in the previous section using microscopy data, the system under investigation is assumed to evolve through agglomeration followed by crystallization from the surface to the core. According to this assumption, partially crystalline aggregates (the most complex participating species formed at the intermediate stage of the synthesis) possess both amorphous and crystalline fractions at the same time. Analysis of the cross-section of defective aggregates (Figure 4.6a) allows to distinguish several zones in their inner structure: 1) crystalline surface with well-resolved crystal facets (Figure 4.6b); 2) central part consisting of small spherical particles with a size of ~ 100 nm (Figure 4.6c); and 3) uniform needles with a radial arrangement in between (Figure 4.6d). Besides, additional voids formed due to the densification upon crystallization can be observed between the needles. The presence of voids is most probably the origin of the aforementioned collapse of the aggregates into tiny **AST** crystals after complete crystallization.

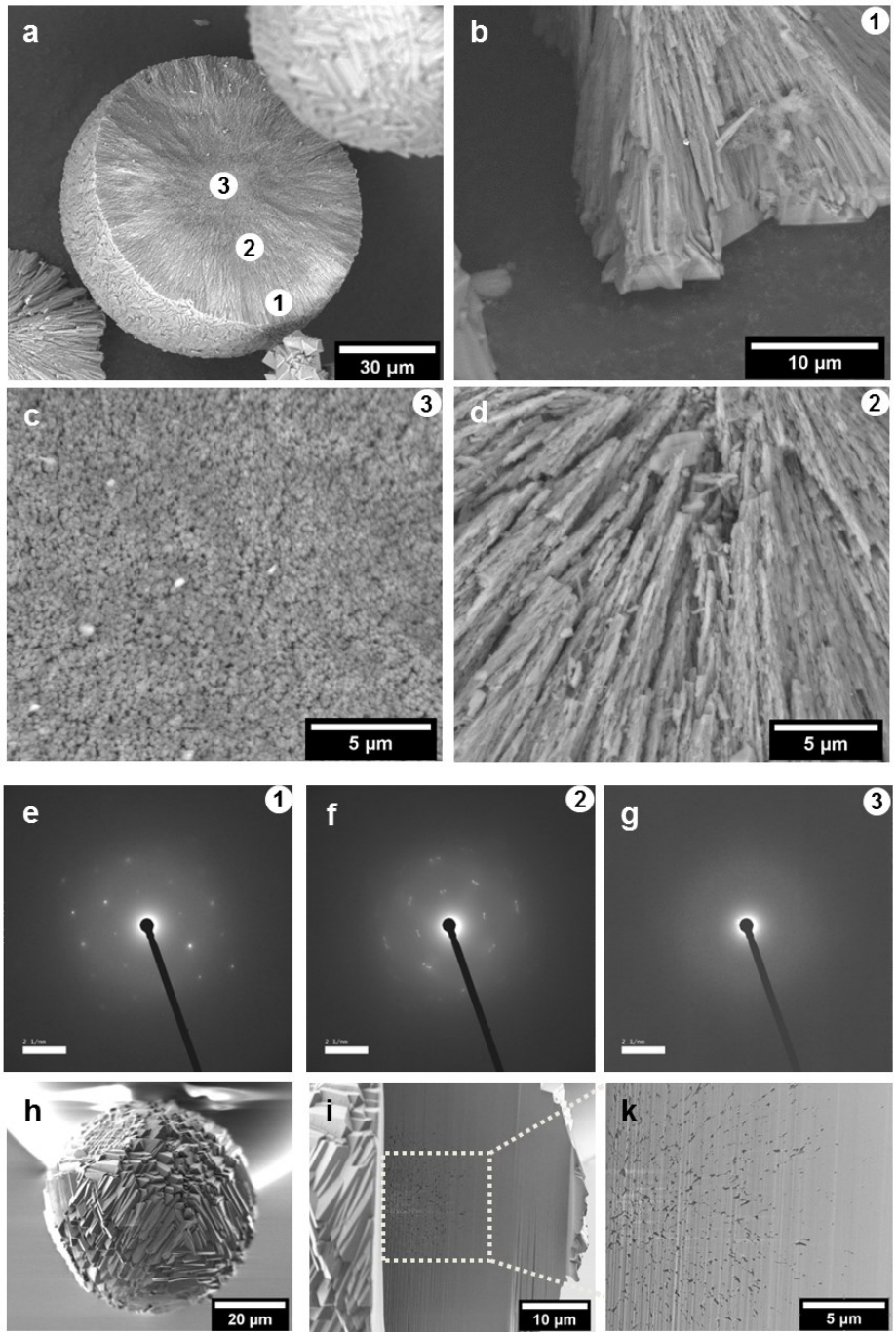


Figure 4.6 Electron microscopy studies on the inner structure of intermediate aggregate in the revered crystal growth. SEM images of defective aggregate in an overall view (**a**); with a crystalline surface with well-resolved octahedral crystal facets (**b**); in the central part consists of small spherical particles with size of ~ 100 nm (**c**); with uniform needles with a radial arrangement in between (**d**). SAED images of the intermediate aggregate on different spots using TEM, after FIB preparation (scale bar: 2 1/nm): (**e**) near the surface of aggregate; (**f**) in intermediate region between the surface and center; (**g**) at the center of aggregate. The numbers represent the sampling regions in respective samples. SEM image of the aggregate (mounted on a tip) obtained in 10 days: (**h**) an overall view; (**i**) a side view of which was milled out a quarter by FIB; (**k**) its corresponding center.

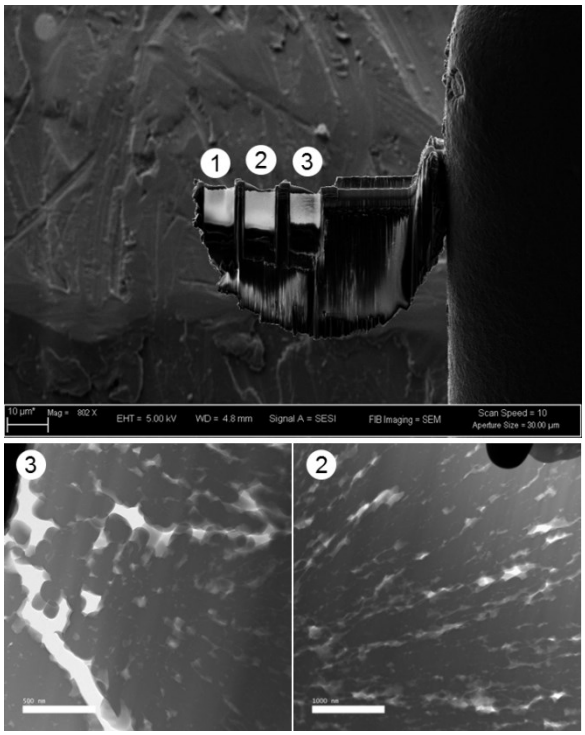


Figure 4.7 Electron microscopy studies on inner structure of aggregates in the intermediate stage of crystallization in the reversed crystal growth. SEM image of the slice of intermediate aggregate after FIB treatment (top) where these three slabs were the sampling regions representing the surface, center and the intermediate zone of the aggregate. TEM images of the respective regions (down).

To confirm the difference in crystallinity of distinguished zones, focused ion beam (FIB) milling was applied to cut spherical aggregate into slices and to polish the obtained slabs, which were further analyzed by selected area electron diffraction (SAED) in TEM (Figure 4.7). Clear diffraction spots in the SAED image of the surface zone (Figure 4.6e) correspond to the well-crystalline **AST** phase near the surface of the aggregate. In contrast, a completely amorphous phase with no signals in the SAED pattern was found at the center of the aggregate (Figure 4.6g). Interestingly, polycrystallites are found in the intermediate region of the aggregates (Figure 4.6f), which means the crystallization process at the middle part of large aggregates is on an earlier stage compared to the outer zone. Besides, the needles consisting of agglomerated crystallites and empty space between them, detected with TEM, are in a good agreement with the SEM results obtained for the defective aggregates (Figure 4.7). This confirms the assumption about the high crystallinity at the outer part and low crystallinity at the inner part for intermediate aggregated particles. When prolonging the synthesis time, needles continue to grow towards the center. It results in the disappearance of small particles at the center, evidencing that crystallization reaches the center at this moment (Figure 4.8). With further increase in the synthesis time, a dense **AST** phase in the shell is

spread inwards the overlying parts of the aggregate, accompanied with the disappearance of needles (Figure 4.8). Simultaneously, the crystals (**AST** phase) in the shell further grow (Figure 4.6h), and voids appear at the core as a result of higher density of crystalline phase than that of amorphous phase (Figure 4.6i-k).

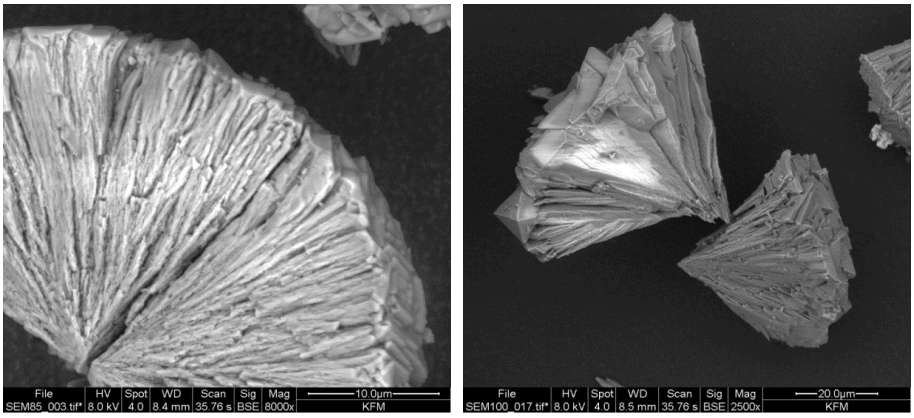


Figure 4.8 SEM images of the defective aggregates obtained in 6 days (left) and 10 days (right) in the reversed crystal growth.

Thus, the evolution of the morphology and crystallinity in the system can be traced with electron microscopy and diffraction methods. However, the application of these techniques requires a destructive samples preparation prior to the measurement, which can affect the inner structure of the material. In addition, voids inside the aggregates can be hardly estimated. Therefore, nano X-ray computed tomography (Nano-XCT) was used as a non-destructive technique to image the evolution of the interior of the aggregates (collaboration with E. Zschech at IKTS). Figure 4.9 shows the tomography studies on the crystals crystallized upon the reversed crystal growth. The size of a single aggregate particle fits perfectly into a field of view (FOV) of 65 µm, which allows visualization of the state of crystallization from the surface to the core of each particle (Figure 4.10) [186]. On a very early stage of the synthesis, the amorphous spherical aggregates have a smooth surface and are uniform inside (Figure 4.9b), which is in good agreement with the SEM data. The aggregate surface becomes rough due to the surface crystallization (Figure 4.9c), while the inner amorphous part is still uniform with no significant difference to the previous stage, confirming the expected direction of crystallization. As crystallization continues inwards, inner voids appear as a result of densification of matter during transformation of amorphous silica to crystalline **AST** phase (Figure 4.9d). Upon further crystallization the volume of inner voids (dark radially distributed stripes) increases (Figure 4.9e).

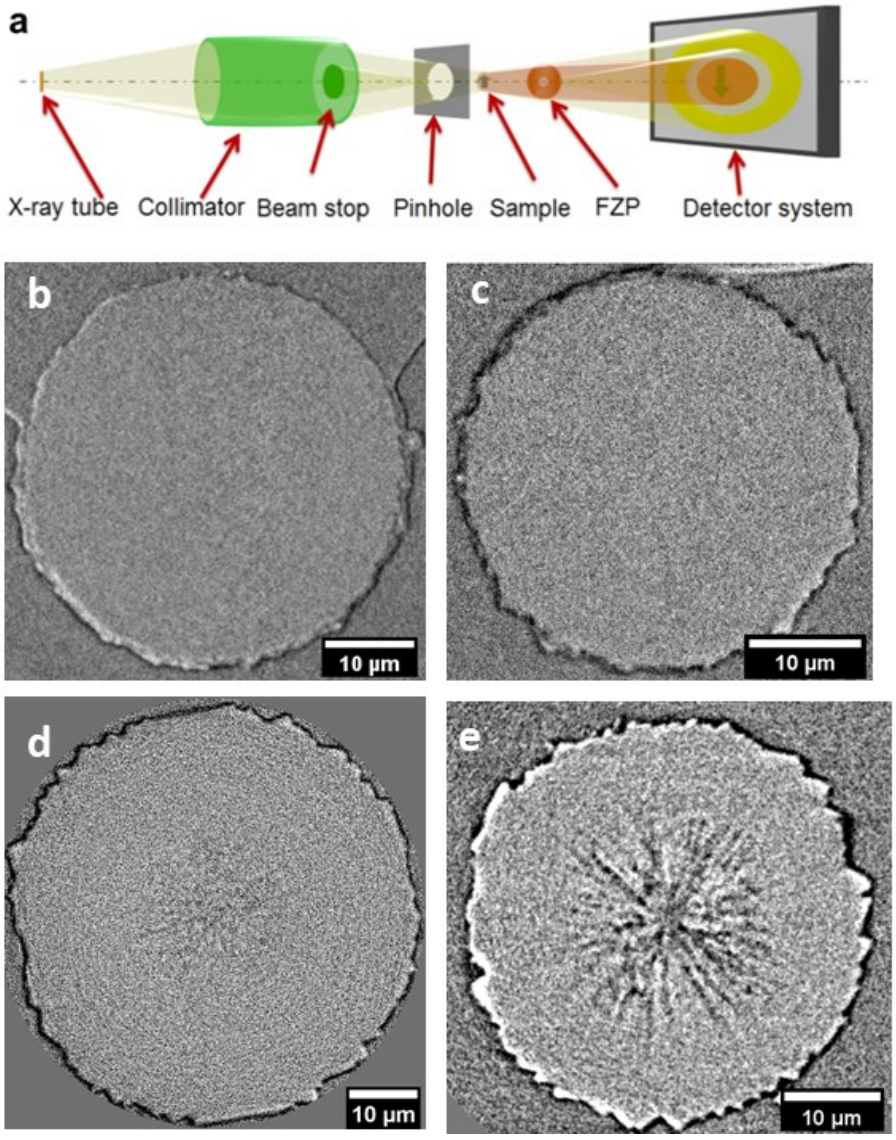


Figure 4.9 Nano X-ray tomography studies on the inner structure of aggregated particles in the revered crystal growth. (**a**) Schematical presentation of the optical path of the X-ray microscope (nano-XCT). Virtual cross sections of aggregated particles obtained in 3 days (**b**), 6 days (**c**), 10 days (**e**), and an intermediate state between 6 and 10 days (**d**). The dark gray values represent a material with low electrical density (air), while bright gray values vice versa (dense crystalline structure).

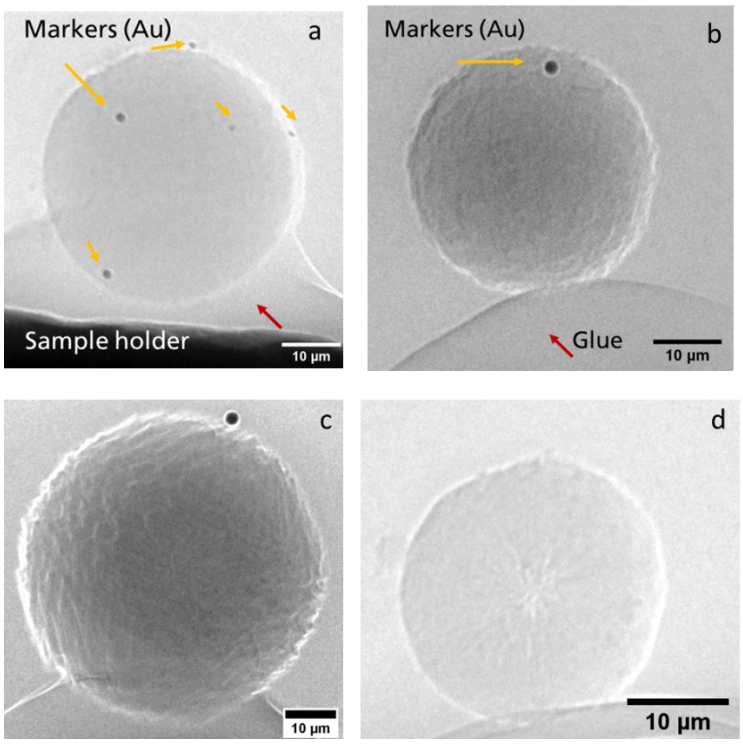


Figure 4.10 Nano-XCT 2D radiographs of the aggregate particles ($x$ =0.5) in different states: (**a**) 3 days; (**b**) 6 days; (**d**) 10 days; and (**c**) an intermediate state between 6 and 10 days. In inner core the dark gray values represent a material with high electrical density (dense crystalline structure), bright gray values vice versa (air/voids).

### 4.1.3 Key factors defining the crystal growth mechanism

Variation of concentrations of both SDA and F can affect the crystallization pathway and crystal growth rate (Figure 4.3). To understand the specific role of SDA and $F^-$, chemical composition of synthesis gel was altered from 1 Si: $x$ $DEDMA^+$: $x$ $F^-$ (normal synthesis) to 1 Si: $x$ $DEDMA^+$: ($x$+0.2) $F^-$ (F-rich conditions) and 1 Si: ($x$+0.2) $DEDMA^+$: $x$ $F^-$ (SDA-rich conditions). To exclude the effect of pH, additional F ions were introduced in a form of $NH_4F$ to set up F-rich conditions, while the excess of $OH^-$ ions (due to the excess of ($x$+0.2) DEDMAOH compared to the $x$ HF under SDA-rich conditions) was compensated by neutralization with 0.2 eq. HBr. To exclude the effect of nature of supplemented halogen anion on the crystal growth, HCl and HI were also tested. Similar obtained results (Figure 4.11) indicate that the type of halogen anion (besides $F^-$) has no significant influence on the crystallization process.

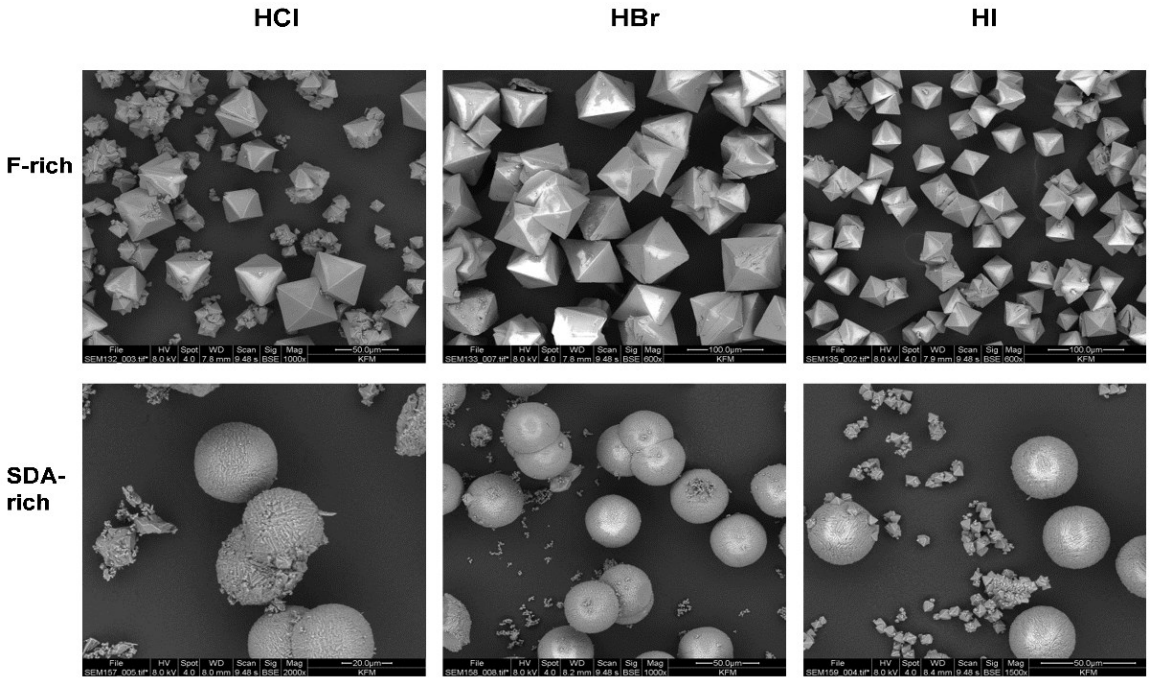


Figure 4.11 The effect of halogen anions ($Cl^-$, $Br^-$, and $I^-$) on the crystallization of zeolite **AST** under both F-rich and SDA-rich conditions. SEM images obtained in 2 days under the F-rich conditions with a synthesis composition of 1 $SiO_2$: 0.5 DEDMAOH: 0.3 HF: 0.2 HX: 4 $H_2O$ (top) and 1 $SiO_2$: 0.7 DEDMAOH: 0.5 HF: 0.2 HX: 4 $H_2O$ (down). From the results we can clearly see that the types of halogen anions do not influence the selection of crystallization pathway.

Increase in $F^-$ concentration results in the expansion of the range of chemical composition for reaction mixtures undergoing classical crystallization: $x_{\text{classical}} = [0.3 - 0.4]_{\text{normal conditions}} \rightarrow x_{\text{classical}} = [0.3 - 0.5]_{\text{F-rich conditions}}$, while the opposite trend is observed when additional SDA is introduced to the system: $x_{\text{classical}} = [0.3 - 0.4]_{\text{normal conditions}} \rightarrow x_{\text{classical}} = [0.3]_{\text{SDA-rich conditions}}$ (Figure 4.12). Besides affecting the crystallization pathway, additional $F^-$ facilitates the crystal growth rate resulting in the increase of crystal sizes from 20 to 40 μm ($x = 0.3$) and from 40 to 60 μm ($x = 0.4$).

Such dependence of crystallization mechanism on the concentrations of $SDA^+$ and $F^-$ can be rationalized taking into account the features of zeolite **AST** structure and the way of its formation. **AST** framework is composed of *d4r* units (small $[4^6]$ cages) connected by "dangling" Si atoms in a way providing also $[4^66^{12}]$ cages significantly larger than $[4^6]$. During the synthesis in fluoride media, $F^-$ is typically located in the small cages (*e.g.* $[4^6]$, *d4r*) and compensated by surrounding cations [153, 187]. In the case of zeolite **AST**, $SDA^+$ is occluded in neighboring $[4^66^{12}]$ cages, which are large enough to accommodate organic

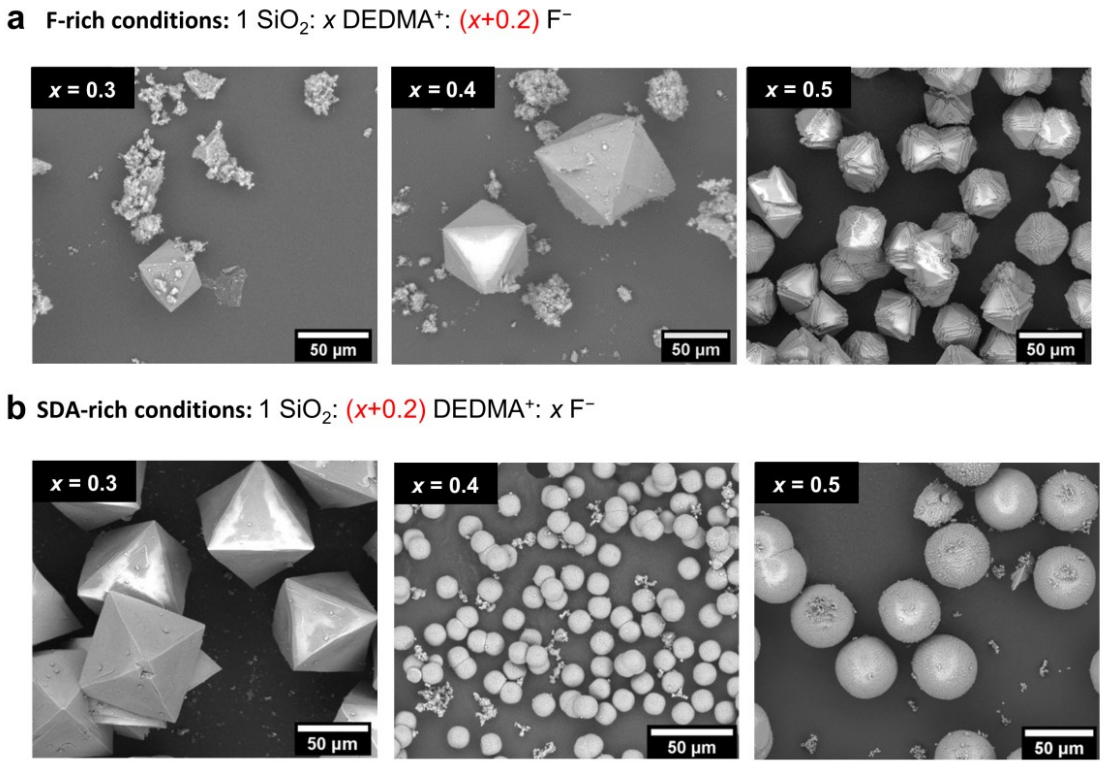


Figure 4.12 The influence of F anion and SDA cation in the synthesis of zeolite **AST** on the selection of crystallization pathways. (**a**) SEM images obtained in 2 days under the F-rich conditions with a synthesis composition of 1 $SiO_2$: *x* DEDMAOH: *x* HF: 0.2 $NH_4F$: 4 $H_2O$ where the $NH_4F$ was used as additional 0.2 eq. $F^-$. (**b**) SEM images obtained in 2 days under the SDA-rich conditions with a synthesis composition of 1 $SiO_2$: (*x*+0.2) DEDMAOH: *x* HF: 0.2 HBr: 4 $H_2O$ where the extra 0.2 eq. HBr was added to neutralize the pH caused by the additional 0.2 eq. DEDMAOH.

cations but have no entrances (pores) to release $SDA^+$ [157, 188]. Addition of $NH_4F$ to the reaction mixture (F-rich conditions) results in 1) formation of occluded ionic pairs ($NH_4^+ – F^–$) that are still relatively mobile (compared to immobilized $SDA^+ – F^–$ pairs) and 2) increase in the overall concentration of fluoride anions provoking fast nucleation and crystal growth via Ostwald ripening. As a consequence, initially formed amorphous precursor particles tend to rapidly transform into relatively small crystallites that further increase in size upon prolongation of the synthesis thus ensuring the *classical* mechanism of **AST** formation. In contrast, addition of extra portion of $DEDMA^+$ (SDA-rich conditions) does not lead to its occlusion as there are no additional compensating $F^–$ anions available in [$4^6$] cages or their analogues in amorphous precursor. Instead, organic cations can interact with the surface of amorphous silica particles inducing the polarization of the surface and thus stimulating their coagulation, which becoming faster process compared to its nucleation under SDA-rich conditions. The same phenomenon is also possible under normal synthesis conditions ([$SDA^+$]

= [$F^-$]) if the overall concentration of $SDA^+ - F^-$ ion pairs exceeds the capacity of **AST** framework for occlusion (at $x \approx 0.4 - 0.5$ according to the obtained data). The domination of initial amorphous particles aggregation (presumably via the mechanism similar to flocculation or coagulation of colloids) over their crystallization ensures the *reversed* mechanism of **AST** formation. Thus, the SDA concentration is the key factor enabling the switching of crystal growth mechanism, while concentration of F anions mainly controls the **AST** crystal growth rate.

### 4.1.4 Summary

A controllable crystallization mechanism between the classical and reversed crystal growth in zeolite **AST** was established based on fine tuning of the interplay among inorganic and organic components under particular synthesis conditions. A truly reversed crystal growth, in which crystallization starts at the surface of amorphous aggregates and then proceeds towards their centers, was demonstrated for the first time. Both kinds of crystallization mechanisms and details of inner structure of intermediate particles were confirmed by electron microscopy studies, while the internal development of crystallinity and voids within the large aggregates upon the reversed crystal growth was visualized by ex-situ X-ray tomography for the first time.

The fundamental functions of SDA and $F^-$ ions that control the crystallization route and crystal growth rate were determined for the first time. The SDA drives the agglomeration of small particles into large amorphous aggregates at very early stages of the synthesis before crystallization starts when the SDA reaches a critical concentration. At low $x$ = SDA/$SiO_2$ ratio ($0.3 \leq x \leq 0.4$) the crystal growth follows the classical route, while at high values ($0.5 \leq x \leq 0.7$) it switches to the reversed crystal growth. Besides, the $F^-$ ions were revealed to govern the rate of crystal growth, a higher concentration of $F^-$ results in a greater growth rate. Understanding the details of growth mechanisms and pathway-determination factors provides a better insight for control of crystal growth, which is important for the improvement of synthesis approaches and design of various forms of crystalline materials.

## 4.2 Zeolites synthesis by advanced ADOR

In this Section, two examples of the construction of new zeolites through optimization of either the *assembly* or the *disassembly* steps in ADOR are considered. This optimization

provides the possibility for the preparation of novel zeolite structures, which cannot be achieved up to now through the hydrothermal synthesis or conventional ADOR protocol. Section 4.2.1 represents a newly developed vapor-phase-transport (VPT) rearrangement technique through controlling the mass transport within the interlayer of zeolite **IWW** for its structural transformation to IPC-18 zeolite; section 4.2.2 shows the synthetic strategy of the structural stabilization of the starting zeolite **IWR** for its transformation to IPC-17.

### 4.2.1 VPT rearrangement technique for the synthesis of new zeolite IPC-18

Germanosilicate **IWW** containing Ge-rich *d4r* units in one dimension and Si-rich *layers* in its framework is a perspective starting material for topotactic transformation to new zeolite using ADOR approach. Previous investigation [90] showed that a lamellar precursor IPC-5P was produced by the treatment of the Ge-rich **IWW** samples (Si/Ge = 3.1) in acidic solutions (0.1 ~ 12 M HCl). However, any subsequent attempts of organization and reassembly led to either reconstruction of the parent **IWW** framework (but increase in Si/Ge ratio), or recrystallization of layers [90]. The reconstruction into initial **IWW** framework is probably caused by the fast reintercalation of Si species during the hydrolysis [98, 189]. Therefore, the challenging task is to find proper conditions to transform the framework of **IWW** zeolite, which can minimize the process of reintercalation of Si during the hydrolysis, while simultaneously preserve the layers of **IWW** framework. It was achieved through controlling the mass transport between the disconnected layers by treatment under the conditions when the amount of solvent is not enough for complete solvation of intermediate species. In our case, **IWW** zeolite was placed over 12 M HCl solution, thus hydrolysis of Ge–O bonds in **IWW** can occur by the HCl vapor but the mass transfer of residing Si species within the interlayers was suppressed due to a low amount of $H_2O$ in the interlayer space.

#### 4.2.1.1 3D-2D-3D zeolite transformation

Three germanosilicates zeolites (**UTL**, **UOV**, and **IWW** with respective Si/Ge ratios of 4.2, 3.1 and 3.7) were applied to the VPT rearrangement approach. **UTL** and **UOV** zeolites, which have been successfully converted into their respective sub-zeolites by the conventional ADOR approach, were chosen as the reference samples for the evaluation of the difference between the conventional ADOR and newly developed VPT strategy. The disassembly (i.e. hydrolysis of *d4r*s units) of germanosilicates was achieved by the reaction of zeolite frameworks with acid vapor (12 M HCl) (i.e. HCl + {–Ge–O–Si–} → {HO–Si–} + {–Ge–Cl}).

Generated volatile $GeCl_4$ (boiling point is 86 °C) was released from the zeolite frameworks, subsequently, adsorbed/dissolved and hydrolyzed in the solution ($GeCl_4 + nH_2O \rightarrow Ge(OH)_nCl_{4-n} + nHCl$) at the bottom of reactor. The presence of Ge in the solution was confirmed by measurement of ICP-OES after the reaction. Compared to the conventional ADOR proceeding in solution, the mass transport of residing Si species between the Si-rich layers in the VPT is minimized thus preventing the reintercalation. This novel method not only enables unrestricted migration of the species generated by decomposition of unstable Ge-rich *d4r* units but also avoids the further reintercalation of Si and thereby water-mediated reconstruction of the germanosilicate framework.

The 2D-to-3D transformation to form the respective daughter structures can be realized by condensation the silanols in the disassembled precursors ({–Si–OH} + {–Si–OH} → {Si–O–Si} + $H_2O$) via calcination. As shown in Scheme 4.1, condensation of precursors obtained from **UTL** results in the generation of the reported zeolite IPC-7 in which *s4r* and *d4r* units are presented as the alternating connecting units between layers, whereas the known zeolite IPC-12 with interlayer *O-bridge* connectivities instead of *d4r* units is formed from **UOV** zeolite. The IPC-n (n = 7, 12) zeolites obtained through the VPT rearrangement did not show any significant difference from their analogues prepared via the conventional ADOR (Figure 4.13). In turn, a new structure, denoted as IPC-18, which contained only *–s4r–* interlayer linkages upon the condensation of IPC-18P precursor, was formed after the VPT treatment of **IWW** (Figure 4.13c). Therefore, the connecting units (i.e. *d4r*, *s4r*, or *–O–*) in the daughter zeolites formed by VPT rearrangement rely on the initial structure of the parent zeolite: the existence of pores in the Si-rich layers (**UOV**: 12 MR, **IWW**: 12 MR and 8 MR) facilitates mass transport in the disassembly step and hence forming the *s4r* units over **IWW** or *–O–* units over **UOV**, while IPC-7 with alternating *d4r*/*s4r* units is produced from **UTL** under the same conditions because of its non-porous layers. Besides, the formation enthalpy for **IWW** with *s4r* was predicted to be lower than that with *–O–* units (by 3.5 kJ $mol^{-1}$) according to the theoretical simulations [96]. Therefore, IPC-18 obtained from **IWW** zeolite contains more stable *s4r* connecting units.

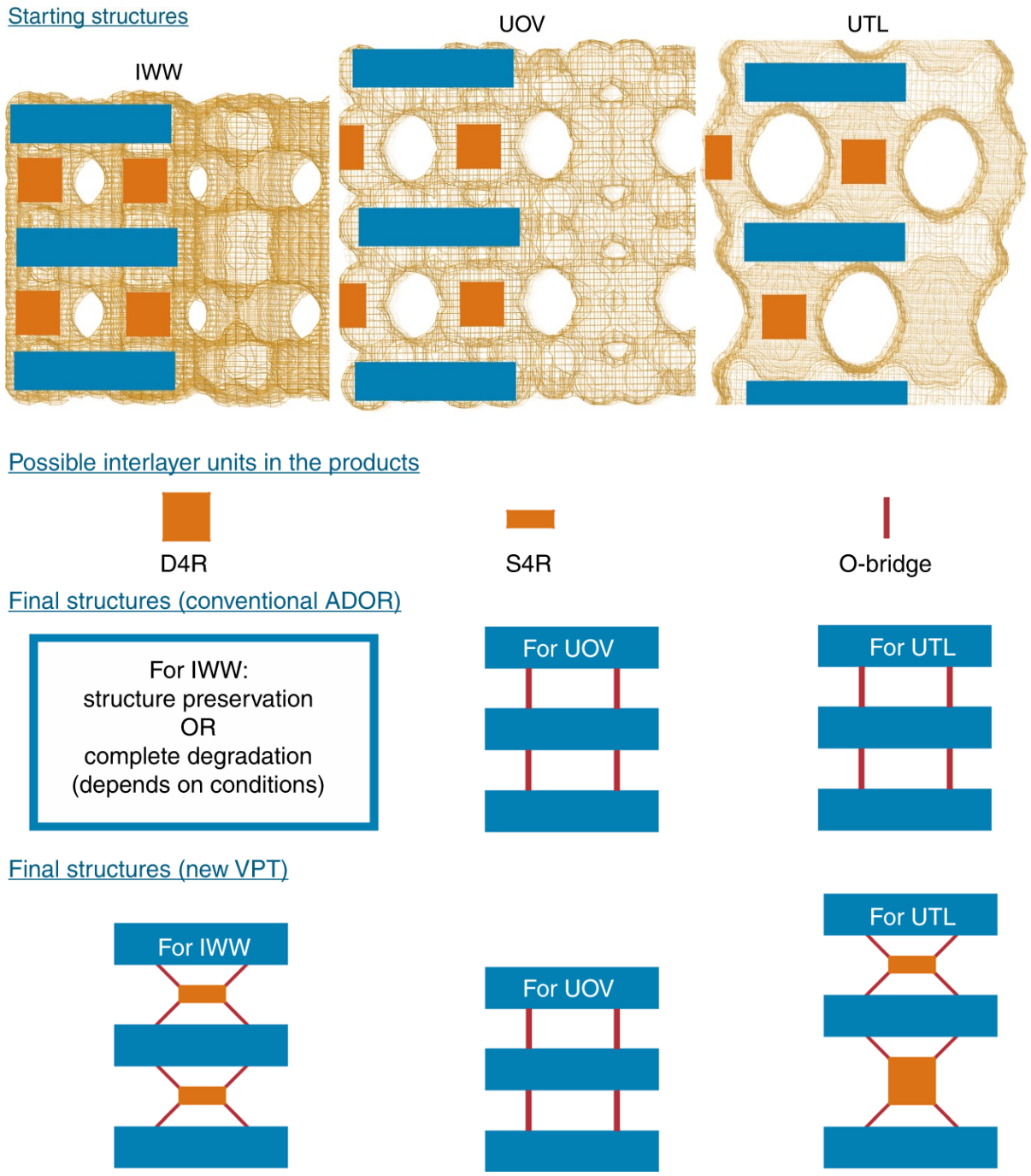


Scheme 4.1 Schematic presentation of initial zeolites (**IWW**, **UOV** and **UTL**) applied and the final products obtained via the conventional ADOR and VPT rearrangement.

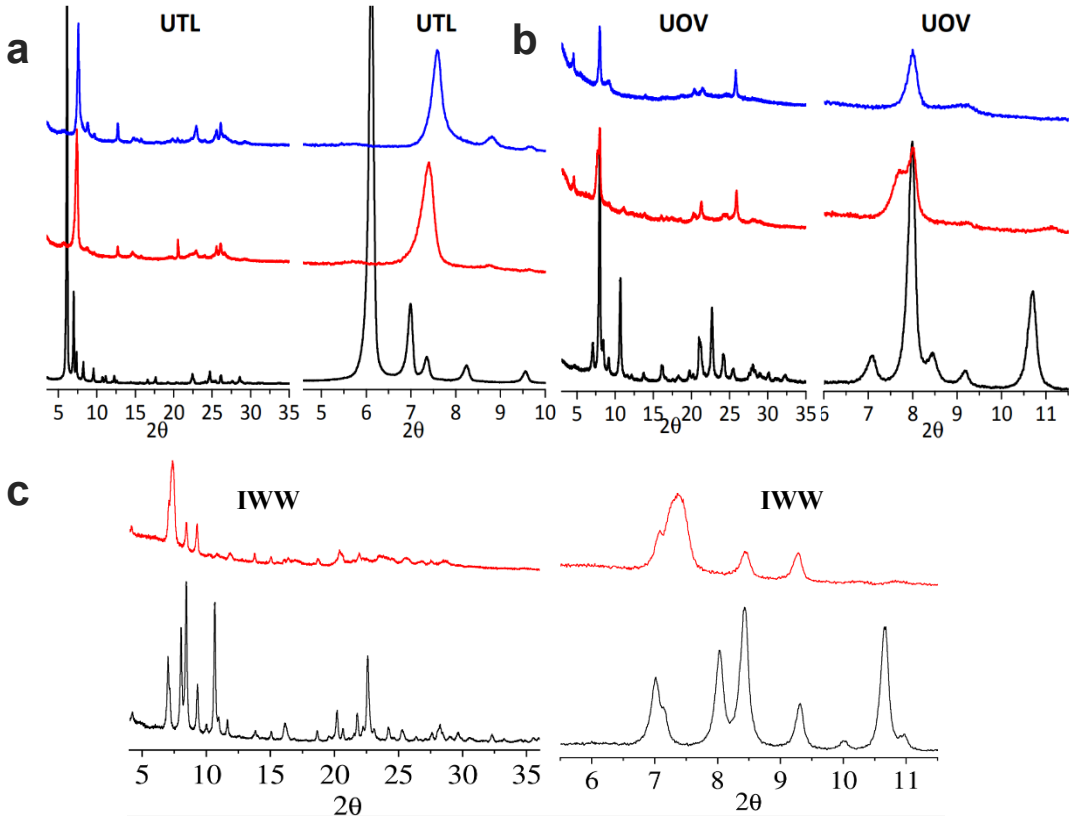


Figure 4.13 XRD patterns of the **UTL**-, **UOV**-, and **IWW**-derived zeolites, starting zeolites (black); samples subjected to VPT (red lines); and further calcination (blue lines). Two types of 2θ scales are used for clarity.

#### 4.2.1.2 Structural features of IPC-18

A reasonable IPC-18 model structure is predicted based on the obtained results and it matches well with its XRD pattern (Figure 4.14a). Based on the Rietveld refinement, the space group of IPC-18 is determined to be $P2_1/c$ with $a = 9.606(4)$ Å, $b = 12.7280(21)$ Å, $c = 40.717(7)$ Å, $\alpha = 90.0°$, $\beta = 94.97°$, $\gamma = 90.0°$, which is different from the initial **IWW** zeolite (*Pbam*). Besides, **IWW** zeolite has a 3D pore system with 8×12×10 channels. Upon the treatment of VPT, 12- and 8-ring pores located in the $a \times b$ plane remain intact, whereas 10-ring pores along the $c$ direction reduce to 8-ring pores due to the transformation of *d4r* into *s4r* units (Figure 4.14b-c). This transformation leads to decreases in micropore volume from 0.172 to 0.104 $cm^3\ g^{-1}$ and average pore size from 0.63 nm to 0.58 nm (Figure 4.14d, e). Despite the decrease in the size and volume of micropores, both **IWW** and IPC-18 zeolites possess the same {mesopore + interparticle} volume of 0.025 $cm^3\ g^{-1}$,

suggesting no significant fraction of additional pores is generated during the VPT transformation.

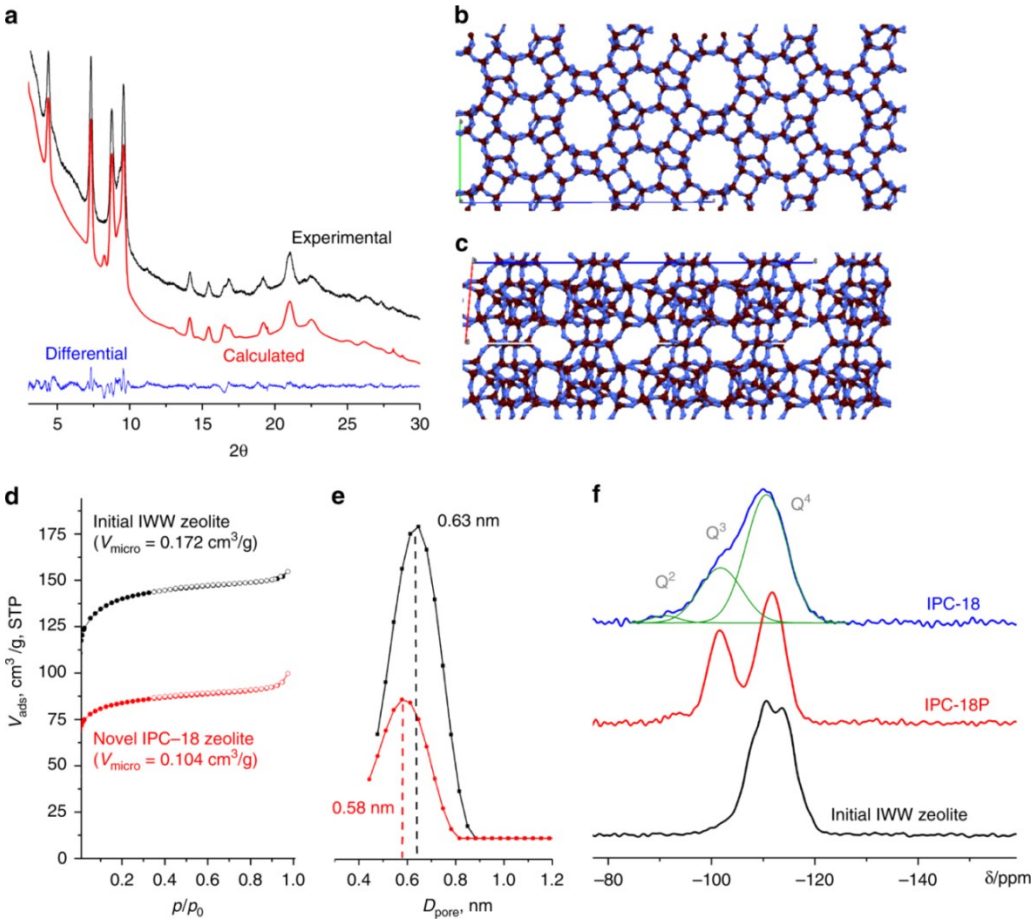


Figure 4.14 Basic characterization of IPC-18. (**a**) Rietveld refinement of XRD patterns of IPC-18. Crystallographic representations of IPC-18 in the *axb* planes projection demonstrating 12 and 8 MR pores (**b**), and in *axc* planes projection showing connectivity between layers through *s4r* units (**c**); (**d**) $N_2$ adsorption/desorption isotherms and (**e**) pore size distribution for parent **IWW** (black) and daughter IPC-18 zeolites (red); **(f)** $^{29}$Si MAS NMR spectra of **IWW**, intermediate IPC-18P and final IPC-18.

$^{29}$Si MAS NMR was used to study the evolution of Si atoms in the framework of **IWW**, IPC-18P, and IPC-18 zeolites (Figure 4.14f). Only one signal corresponding to fully condensed $Q^4$ form of Si atoms (−115 ppm) is presented in the starting **IWW**. In the acid vapor, the Si–O–Ge bonds in **IWW** are hydrolyzed leading to the generation of silanol groups in the IPC-18P. As a result, the intensity of the $Q^3$ signal (−101 ppm) after VPT treatment increases. In addition, a low-intensity $Q^2$ signal (−93 ppm) appears in IPC-18P intermediate. Further calcination of IPC-18P reduced $Q^3$ intensity due to the condensation of its silanols

(2D-to-3D transformation). Nevertheless, the resulting IPC-18 zeolite still maintains a large fraction (25 – 30 %) of $Q^3$ signal, which is probably attributited to the lower calcination temperature than the optimal for structure condensation. In addition, a small amount of residual Ge in the framework of IPC-18 provides $Si(OGe)(OSi)_3$ units containing Si atoms with a characteristic signal that overlap with the $Q^3$.

#### 4.2.1.3 Microscopy study of IPC-18 *vs.* parent IWW

Figure 4.15 shows the comparison between crystal morphologies of the parent **IWW** and resulting IPC-18. There is no significant difference observed, both materials have similar crystals with 10×4×1 μm in size. This is probably because no strong perturbation force was imposed to the crystals, while the crystals break into small pieces during the hydrolysis by using conventional acid solution under agitation [190].

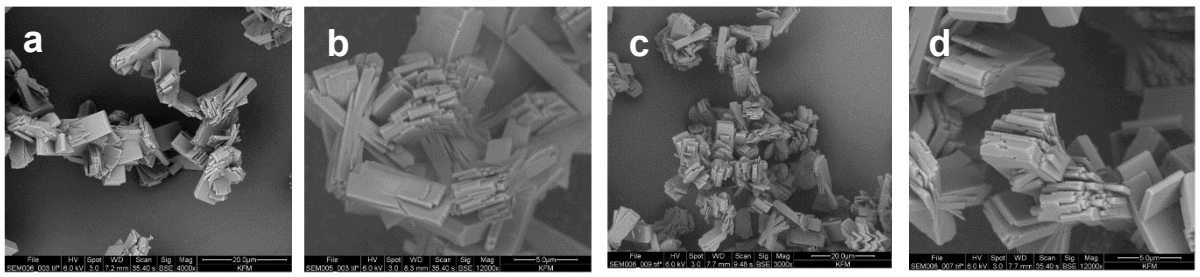


Figure 4.15 Comparison of the crystal morphology of the parent **IWW** (**a**, **b**), and resulting IPC-18 (**c**, **d**).

$C_s$-corrected STEM was employed to analyze the structural similarities and differences between the initial **IWW** and resulting IPC-18 zeolites. Figure 4.16ac records the layers along the [100] direction from the top view, both **IWW** and IPC-18 samples show the same pore system and arrangement, confirming the preservation of the Si-rich layers during the VPT treatment and subsequent condensation. In the structure model, the distance between the T elements of *d4r* is measured to be ~ 3.1 Å, thus, a decrease of ~ 3 Å of the interlayer distance should be expected when the *d4r* is transformed to *s4r*. Along [100] direction, *d4r*s state influenced by the hydrolysis cannot be seen. The difference related to the change from *d4r* to *s4r* can be observed from the side view along [010], as shown in Figure 4.16b-d. The distances between two layers are 12.23 and 9.11 Å for **IWW** and IPC-18, respectively, which is in line with simulated results. Moreover, SAED and FFT images also clearly show well crystalline materials (Figure 4.16).

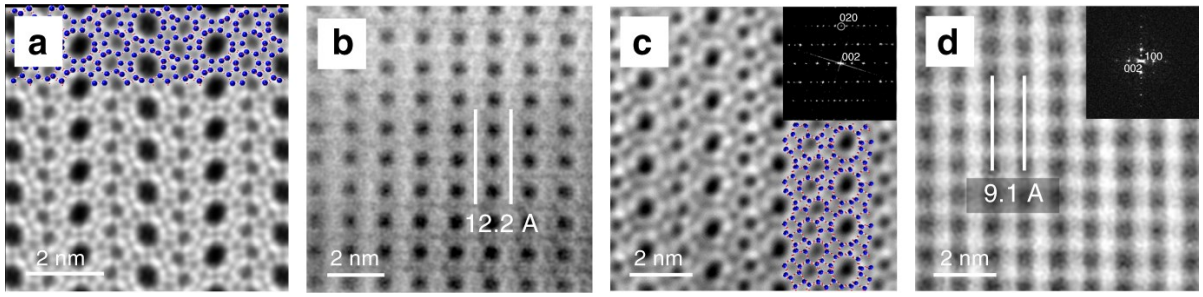


Figure 4.16 $C_s$-corrected STEM-ADF images of **IWW** (**a**, **b**) and IPC-18 (**c**, **d**) zeolites.

#### 4.2.1.4 Mechanism of VPT zeolite rearrangement

To get a better understanding of both disassembly and reassembly process during the transformation, the structure of the intermediate after the VPT treatment (i.e., **IWW** → IPC-18P) and topotactic condensation (i.e., IPC-18P → IPC-18) were characterized by the *in situ* techniques (Figure 4.17) (collaboration with Z. Luo at USTC). The diffraction peaks with varying positions over time were recorded by *in situ* synchrotron XRD. The evolution of the interlayer (*hkl* ($l \neq 0$) and intralayer (*hk0*) peaks was identified to elucidate the mechanism of **IWW** → IPC-18P → IPC-18 transformations (i.e. 3D-2D-3D transformation). In addition, *in situ* XRD and XANES were used to quantitatively analyze the lattice and the local state of the Ge elements during the VPT rearrangement to determine the relationship between the properties of leaving atoms and framework characteristics during the process of the structural transformation.

Immediately after injection of 12 M HCl solution into the reactor, the peak positions related to the *001* plane shifted to higher angles (Figure 4.17a), evidencing a decrease in the interlayer d-spacing caused by the decomposition of *d4r*s. Both intensities and positions of XRD diffraction peaks related to both inter- and intralayer planes (*e.g. 110* and *400*) are also experienced a remarkably change in the first stage of hydrolysis (0 – 2 min). To quantitatively analyze the changes, we correlated the unit cell parameters and reaction time, as shown in Figure 4.17c, which gives further insight into the VPT processes. Actually, besides the interlayer parameter (*c*), all *a, b, c* constants significantly changed, meanwhile, the indicator ($\beta$ angle) of the layers shift relative to each other maintains unchanged in the first step. These results indicate that Si-rich layers relaxed with only a partial distortion but were still stacked at this stage, which is probably a result of hydrogen bonding and ionic interactions between interlayer species. The major change in the state of Ge atoms is clearly revealed in the spectra of *in situ* XANES where the Ge K-edge ($E_0$) steeply and linearly

decreases with time in this stage (0 – 2 min) due to the breakage of the most Ge–$OT^{IV}$ ($T^{IV}$ = Si or Ge) bonds (Figure 4.17d).

When reaction reaches to the second stage (2 → 10 – 12 min), the positions related to the *hkl* ($l \neq 0$) planes continue to gradually shift to higher angles. However, the *c* parameter experiences a series of minor changes (at ~ 0.5, 2, 3 min) firstly, and then starts to decrease, while, the *a* and *b* decrease monotonically in this stage. Interesting, the $\beta$ increases first and then decreases (peak at ~ 90.7°), suggesting a transient modification of the layers (structural organization). XANES spectra show the evolution of the state of Ge over time in the second stage, which is accompanied by a linear change in $E_0$ but slower than in the first stage. The overall transformation during this period is accounted for a slow hydrolysis of the remaining Ge–O bonds after primary deconstruction of the *d4r*s and leaching of Ge species residing in Si-rich layers. Complete decomposition of *d4r* and removal of leached species enable the partial recovery of layer because $\beta$ and *b* return to their initial values at the end of the second stage (~ 12 min).

At the final stage (> 12 min) of the VPT treatment, the intensities and positions of most XRD diffraction peaks maintain, corresponding to the final lattice parameters. Only peaks related to the *hkl* ($l \neq 0$) planes (such as *313* and *001*) show minor changes in the intensities during this stage. Besides, the $E_0$ of Ge atoms keeps nearly invariable during the final hydrolysis.

Heating the intermediate IPC-18P obtained by the VPT treatment of zeolite **IWW** up to ~ 500 K has no significant impact on the positions or intensities of XRD peaks relating to the intralayer *hk0* planes (Figure 4.17 b). In contrast, the position of *001* reflection associated with the interlayer *d*-spacing gradually shifts to high angle upon thermal treatment in the range of $T = \mathrm{RT} - 350$ K, and then being almost constant at temperatures of 350 – 450 K. Further increase in the temperature to 450 – 650 K leads to a shift of positions in all XRD reflections and a reduction of the intensities at the temperatures higher than 650 K, showing a gradual loss of the crystallinity of IPC-18.

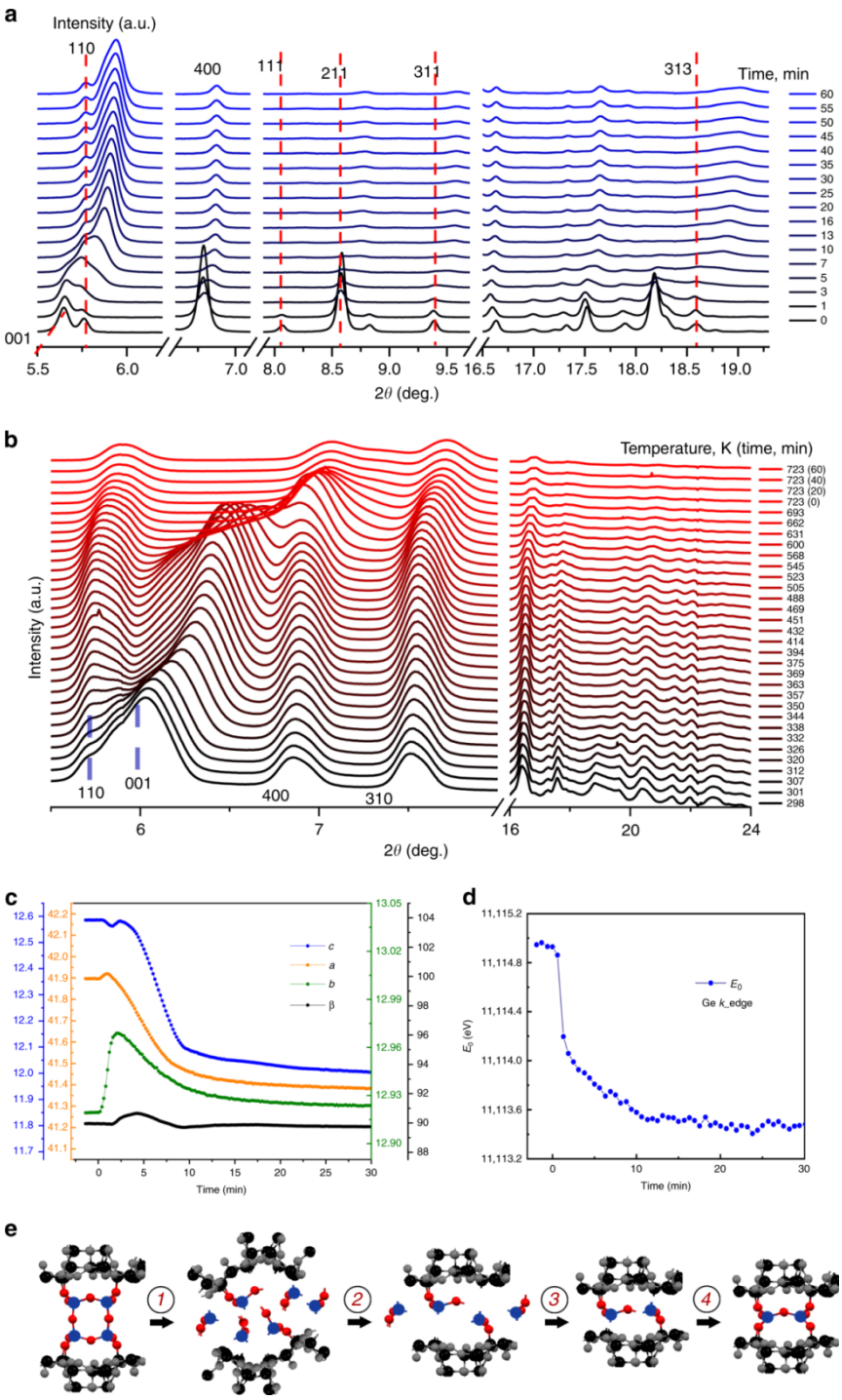


Figure 4.17 In situ studies on the mechanism of VPT. (**a**) In situ XRD patterns of the parent **IWW** during the VPT treatment under the acid vapor; (**b**) in situ XRD patterns recorded the thermal condensation of IPC-18P into IPC-18; (**c**) variation of unit cell parameters (lengths in Å and angle in degree) as a function of time during the VPT treatment; (**d**) evolution of Ge K-edge ($E_0$) extracted from in situ XANES spectra representing changes in Ge state during the VPT treatment; (**e**) schematic presentation of the proposed mechanism (Si and Ge atoms are not distinguished for clarity) for the whole processes.

According to the results of *in situ* XRD and XANES, a plausible mechanism (Figure 4.17 e) for the transformation of **IWW** → IPC-18P → IPC-18 (3D-2D-3D) was proposed:

(1) 0 – 2 min: fast breakage of Ge-rich *d4r*s accompanied by partial deformation of the Si-rich layers at room temperature;
(2) 2 – 12 min: extraction of the rest Ge along with the partial reorganization of the parent Si-rich layers;
(3) 10 – 12 min: slow rearrangement of the species remaining in the interlayer space until an equilibrium state reached at room temperature (> 12 min);
(4) thermal condensation of layers (reassembly) upon mildly enhanced temperatures (~ 350 K) with negligible effect on the layer structures.

#### 4.2.1.5 Summary

This newly developed VPT rearrangement approach was successfully applied for the ADOR transformation of a series of germanosilicate zeolites with 1D Ge-rich *d4r* units (i.e., **IWW**, **UOV** and **UTL**). This novel protocol overcomes the limitations of the conventional ADOR method, in which the mass transport within the interlayers cannot be controlled. Besides the known IPC-7 and IPC-12 with high crystallinity by VPT technique prepared from respective **UTL** and **UOV** zeolites, a new IPC-18 zeolite, which was previously predicted but not yet synthesized via existing synthesis methods has been successfully prepared. The plausible mechanism of VPT rearrangement was revealed using *in situ* synchrotron XRD and XANES results demonstrated the acid-induced reorganization of the interlayer and intralayer units of zeolite **IWW**, leading to a transient disordering of the structure with further reconstruction to a well-ordered new material. The VPT rearrangement approach was successfully applied into different germanosilicates, highlighting the potential application of this technique for the structural transformation of other crystalline materials with an unstable frameworks deconstructing upon the solvent treatment.

### 4.2.2 ADORable IPC-17 zeolite derived from germanosilicate IWR

**IWR** zeolite was firstly discovered as aluminogermanosilicate zeolite [106], then five types of **IWR** materials with different chemical compositions − pure siliceous, aluminosilicate, germanosilicate, borosilicate, and borogermanosilicate − were also prepared [175, 176, 178]. From the structural point of view, **IWR** zeolite containing Si-rich *layers* connected by *d4r* units can be potentially transformed into new zeolites by the ADOR

approach. Ge is preferred to be located in the *d4r* units, while Al and B elements are randomly distributed in the IWR framework [80, 175, 176]. Therefore, from the chemical point of view, only germanosilicate and borogermanosilicate **IWR** are suitable candidates for the realization of structural transformation by the ADOR approach because the treatment of the others in water/acidic solution can lead to either structural collapse or preservation of initial structure [178]. Many studies on the location of Ge in **IWR** zeolite revealed that in addition to its preferential location in the *d4r* units, Ge also occupies other T-sites in the Si-rich layers, especially at a low Si/Ge ratio [177, 191]. The presence of Ge in the layers makes the zeolite highly hydrolytically unstable. As a result, germanosilicate **IWR** (Si/Ge =1.8) was degraded into amorphous material in water under room temperature [178]. An acidic treatment of borogermanosilicate **IWR** with relatively low Ge content (Si/Ge = 6.9, 14.8 % B) showed that it has been disassembled even after 5 minutes of the treatment but the formation of lamellar precursor was accompanied by the layer destruction excluding their manipulation via ADOR protocol [91]. In this section, we apply several strategies relating to the *assembly* step to improve stability of the **IWR** layers and show successful transformation into new zeolite.

#### 4.2.2.1 Strategies for stabilization of IWR

Five synthetic strategies were applied to improve the stability of **IWR** layers (see section 3.2.6 for experimental details):

- *Variation of the Si/Ge ratio in the initial **IWR** zeolite*. For a successful disassembly of the **IWR** framework into layers, the Si/Ge ratio below 6 in the parent **IWR** is necessary [87, 102]. The post-modification stabilization to adjust the Si/Ge ratio leads to the **IWR** zeolite with too low Ge (Si/Ge > 100) and also the formation of defects under harsh conditions [178]. Therefore, this method was not considered. Herein, we applied the direct hydrothermal synthesis of borogermanosilicate **IWR** in the reaction mixtures with Si/Ge = 2 – 5 and (Si+Ge)/B = 20 using SDA1.
- *Stabilization/healing of structural defects (silanols) in **IWR** zeolite*. Silanol defects in zeolites leading to the instability when contacting with water [104] are often formed in high pH media. These defects can be minimized by the introduction of $F^-$ ions into the reaction mixture. Therefore, F-stabilized borogermanosilicate **IWR** was synthesized in F-containing reaction mixture (Si/Ge = 2 and (Si+Ge)/B = 20) using SDA1, which can potentially lead to improvement of the layer stability during the following *disassembly* and *reassembly* steps.

- *Decrease in the B content using seeded method*. The borogermanosilicate **IWR** prepared using SDA1 was submitted as the crystal seeds for the synthesis of **IWR** zeolite in the absence of B source. Sample obtained at the first iteration of seed-assisted synthesis was used as the source of seeds for the second iteration under the same conditions. As the result of repeatedly seeding synthesis, the content of B in the final sample was decreased to < 0.1 % according to the chemical analysis by ICP-OES. Direct synthesis with a low B content in reaction mixture without seeding was not successful as it led to the formation of a second **IWW** phase.
- *Decrease in the B content in direct synthesis with another SDA*. Instead of using SDA1 (hexamethonium dihydroxide), SDA2 (1,8-diazabicyclo[5.4.0]undec-7-ene) was chosen to synthesize B-free germanosilicate **IWR** [182]. One specific feature of samples prepared by this approach is of extremely low thickness (~ 10 nm) along *c* crystallographic axis. As a result, the (001) diffraction peak in the XRD patterns (at ~ 7°) was found to possess negligible intensity for such IWR(SDA2) crystals. In addition, this *c* axis is related to the direction of the main structural changes expected upon ADOR transformation. Thus, the layer stability can be limited due to the harsh conditions typically applied in ADOR.
- *Increase in the stability of germanosilicate **IWR** by seeding method*. Similar seeding strategy was applied to synthesize stable germanosilicate **IWR** in the presence of SDA1 by using IWR(SDA2) as seeds. The obtained **IWR** crystals (IWR(SDA1)) have a different morphology to IWR(SDA2) and the (001) diffraction peak in the XRD patterns appears back compared to that of IWR(SDA1).

The XRD patterns of the final products are shown in Figure 4.18. The introduction of B can promote the formation of **IWR** phase when using SDA1, otherwise the **IWW** phase is present as impurity [91]. When the B/Si mol% in the synthesis gel exceeds 5, undesirable **IWW** phase is also present in the final products (Figure 4.18a, IWR-2-B-10). In contrast, pure borogermanosilicate **IWR** can be crystallized from the gels containing sources with Si/Ge = 2 – 5 and T/B = 20, either with or without $NH_4F$, despite a low intensity of (001) diffraction peak. Well crystalline **IWR** zeolite was achieved when using borogermanosilicate **IWR** as seeds in B-free media. Pure germanosilicate **IWR** was obtained using SDA2 without the introduction of B (Figure 4.18b, IWR(SDA2)). Well crystalline germanosilicate **IWR** with increased layer thickness was obtained when the IWR(SDA2) was submitted as seeds in the presence of SDA1 (Figure 4.18b, IWR(SDA1)).

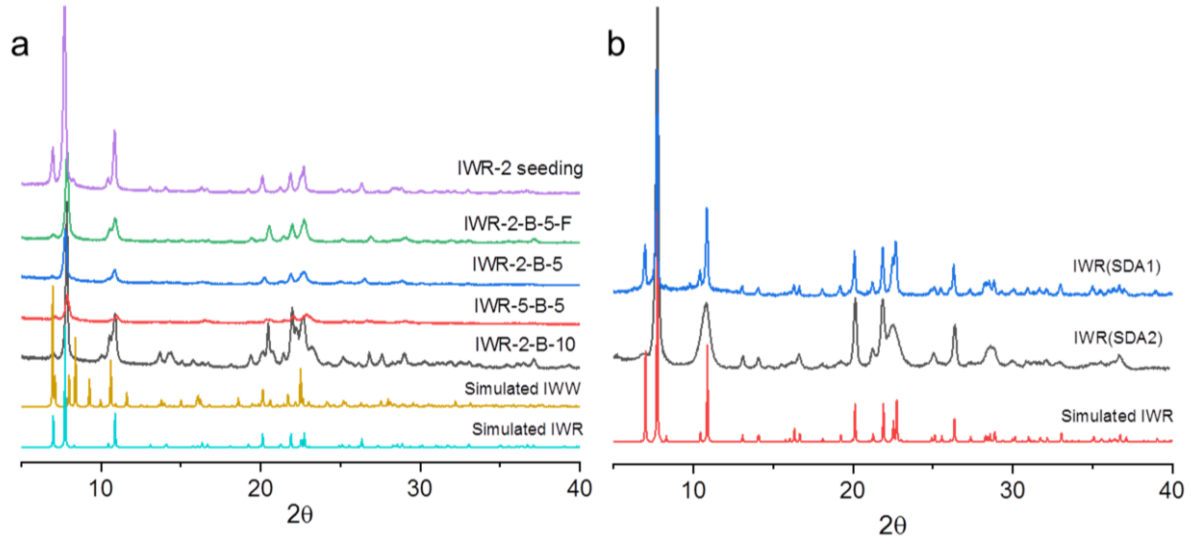


Figure 4.18 XRD patterns of **IWR** zeolites prepared in different conditions. (**a**) Sample label of IWR-x-B-y means that this sample was prepared with x = Si/Ge and y = B/(Si+Ge) in mol%; IWR-2-B-5-F is the sample synthesized with Si/Ge = 2 and (Si+Ge)/B = 20 in the F media; IWR-2 seeding is the sample prepared with Si/Ge =2 using the obtaining B-containing **IWR** as seeds in an iteration method. (**b**) IWR(SDA2) was prepared with Si/Ge =2 in the presence of SDA2; IWR(SDA1) is sample synthesized with Si/Ge =2 using IWR(SDA2) as seeds in the presence of SDA1.

#### 4.2.2.2 Application of ADOR approach

The *disassembly* was performed either in acid solution (0.1 M and 12 M HCl) or in its acid vapor (12 M HCl). The key parameters to access the accomplishment of ADOR transformation are the positions of "interlayer" peaks in the XRD patterns (indicator for the change of interlayer distance) and the intensities of "intralayer" peaks (representative for the layer crystallinity). If the right-shift of (00l) "interlayer" reflections in the final daughter zeolites is smaller than predicted (*e.g.* if 2θ position for (001) peak < ~ 8.8°), it is considered as unsuccessful transformation.

Treatment of these **IWR** borogermanosilicates (*i.e.* IWR-2-B-5 and IWR-5-B-5) in 12 M HCl solution leads to a shift of the (001) diffraction peak to a higher angle, indicating a decrease in the interlayer distance due to the extraction of Ge from *d4r* units (Figure 4.19a). At the same time, the intensities of the intralayer diffraction peaks decrease, suggesting a degradation of the layers in these two **IWR** borogermanosilicates. The evidence of the degradation of the intralayer units is more obvious after thermal condensation of the resulting intermediates at 450 °C as almost all diffraction peaks disappeared (Figure 4.19b). Similar layer degradation in acidic solution was also observed in the F-stabilized borogermanosilicate

**IWR**. Besides, its layers are not completely disconnected in 12 M HCl solution as the peak at ~ 7° remains despite the low intensity.

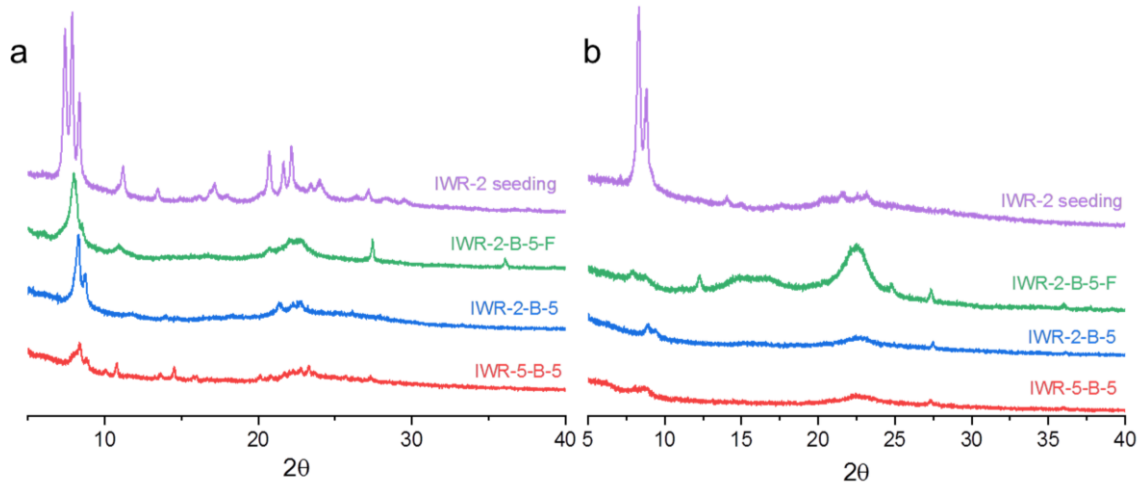


Figure 4.19 XRD patterns of **IWR** samples treated in 12 M HCl solution for 6 hours (**a**) and the resulting samples after calcination at 450 °C for 2 hours (**b**).

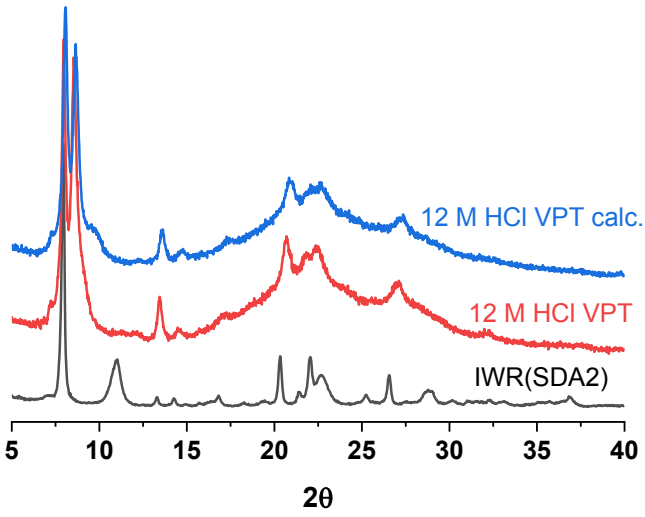


Figure 4.20 XRD patterns of samples prepared by treating IWR(SDA2) in the 12 M HCl vapor for 16 hours and subsequent calcination at 450 °C for 2 hours.

Successful *disassembly* was achieved in the B-depleted sample synthesized by using B-containing IWR as seeds in the B-free reaction mixture in an iteration sequence when treated in 12 M HCl solution, as a shift of (001) diffraction peak and a preservation of intralayer diffraction peaks were observed (Figure 4.19, IWR-2 seeding). The following *reassembly* by treating the resulting intermediate at elevated temperature leads to the

formation of new zeolite, which is denoted as IPC-17, however, its crystallinity is relatively poor. Similar outputs were obtained with IWR(SDA2) when treated in 12 M HCl vapor followed by calcination at 450 °C for 2 hours (Figure 4.20). In addition, a broad peak at 15 – 30° was observed in both the disassembled intermediate and final IPC-17, indicating a degradation of the thin layers in IWR(SDA2).

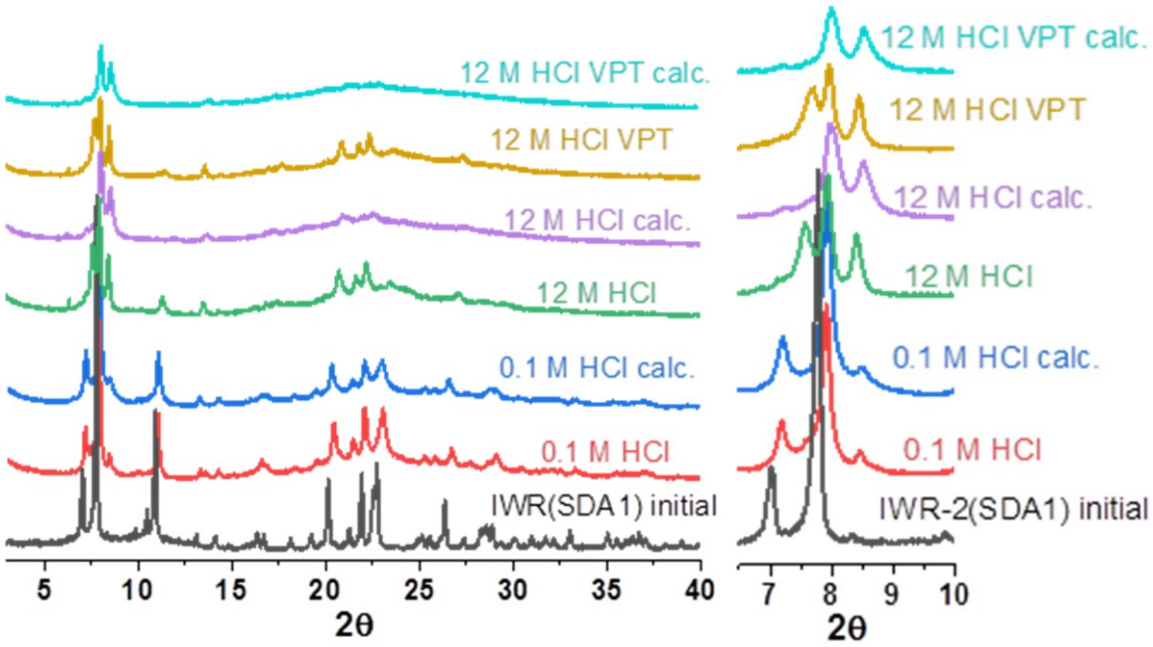


Figure 4.21 XRD patterns of samples prepared by treating IWR(SDA1) in the 0.1, 12 M HCl solution, and 12 M HCl vapor and following calcination at 450 °C for 2 hours (left), and and the enlarged part at 2θ 6.5 – 10° (right).

An improved crystallinity of the resulting IPC-17 was achieved when the SDA type was changed (SDA2 → SDA1) between two seeding steps. Due to the increased layer thickness, the intensity of the (001) diffraction peak in IWR(SDA1) increases compared with the IWR(SDA2) (Figure 4.21). When the diluted HCl solution (0.1 M) was applied as the disassembly agent, incomplete hydrolysis is occurred as the (001) diffraction peak remains in both disassembled intermediate and thermally treated sample.

The behavior of different types of prepared **IWR** zeolites upon *disassembly* and further *reassembly* was summarized in Scheme 4.2, where green color means the success of transformation, yellow – partial success, and red – unsuccessful outcome.

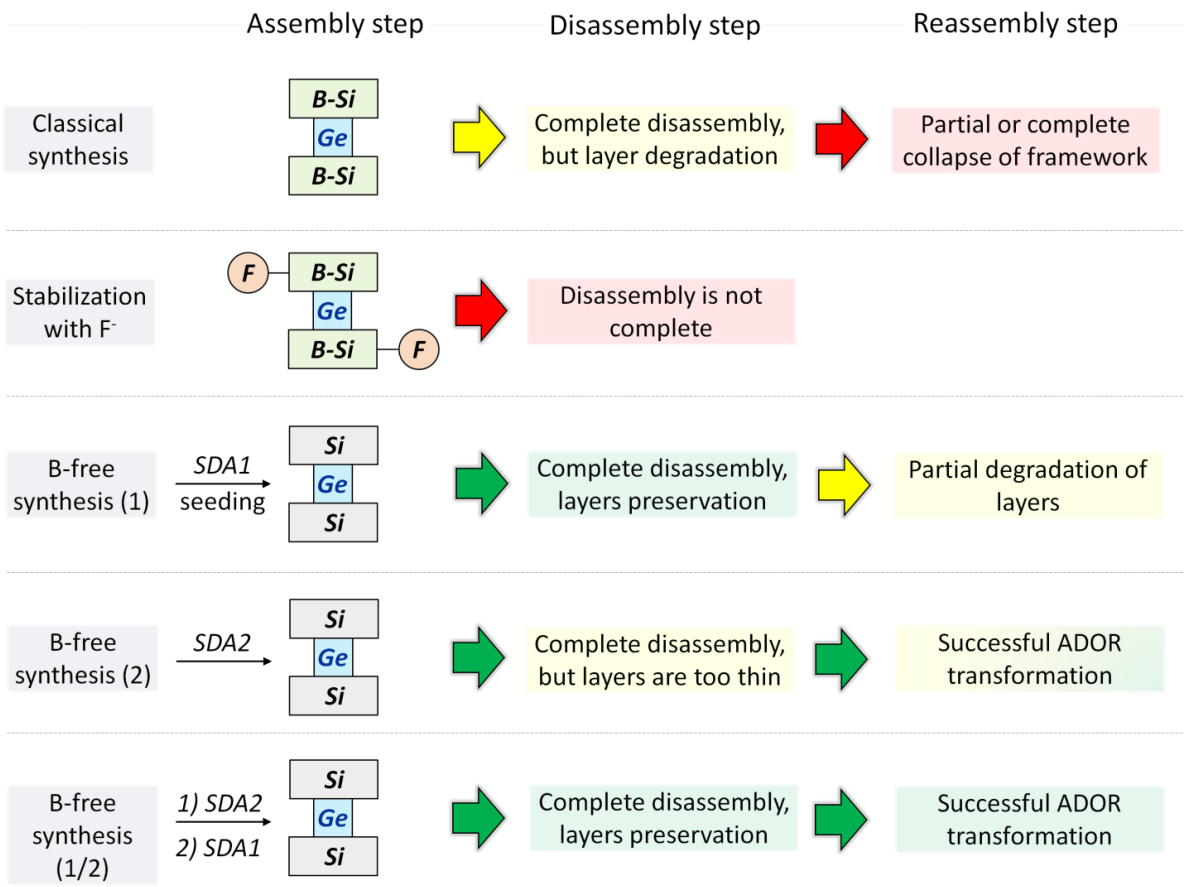


Scheme 4.2 Variation of the **IWR** zeolite synthesis strategy for *assembly* step and its consequence for following *disassembly* and *reassembly* steps.

### 4.2.2.3 Structural feature of IPC-17

Several possible IPC-17 structures were estimated by DFT method according to the topology of parent **IWR** zeolite [96]. Figure 4.22 shows the preliminary data of Rietveld refinement of IPC-17, which represents a good fit of the estimated structure (collaboration with P. S. Wheatley at U. St Andrews).

Successful formation of new zeolite IPC-17 was also confirmed by the results of high-resolution transmission electron microscopy (HRTEM) (Figure 4.23). Considering the negligible difference in topology of layers in parent IWR and daughter IPC-17 zeolites (Figure 4.23ae, $a \times b$ projections for both materials are practically the same), a good match of "top view" HRTEM images is in accordance with the model (Figure 4.23cg). Unmodified 12-ring pores and their preservation in final IPC-17 can be recognized. The decrease in d-spacing along c direction from 1.24 to 0.98 nm upon transformation also correlates with the value predicted for the model and corresponds to the change in the interlayer distance caused by the replacement of *d4r*s by *s4r*s units (Figure 4.23 bd and fh, "side" view).

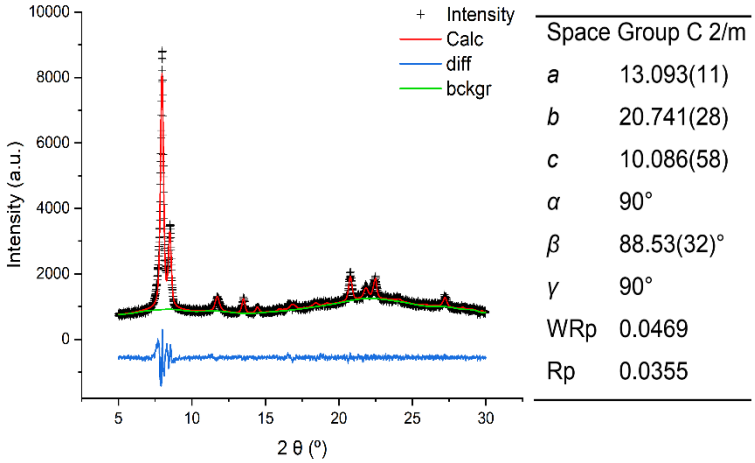


Figure 4.22 Rietveld refinement of IPC-17 (top) and comparison of **IWR** and IPC-17 structure where the *d4r* units in **IWR** transform into the *s4r* units in IPC-17 (bottom).

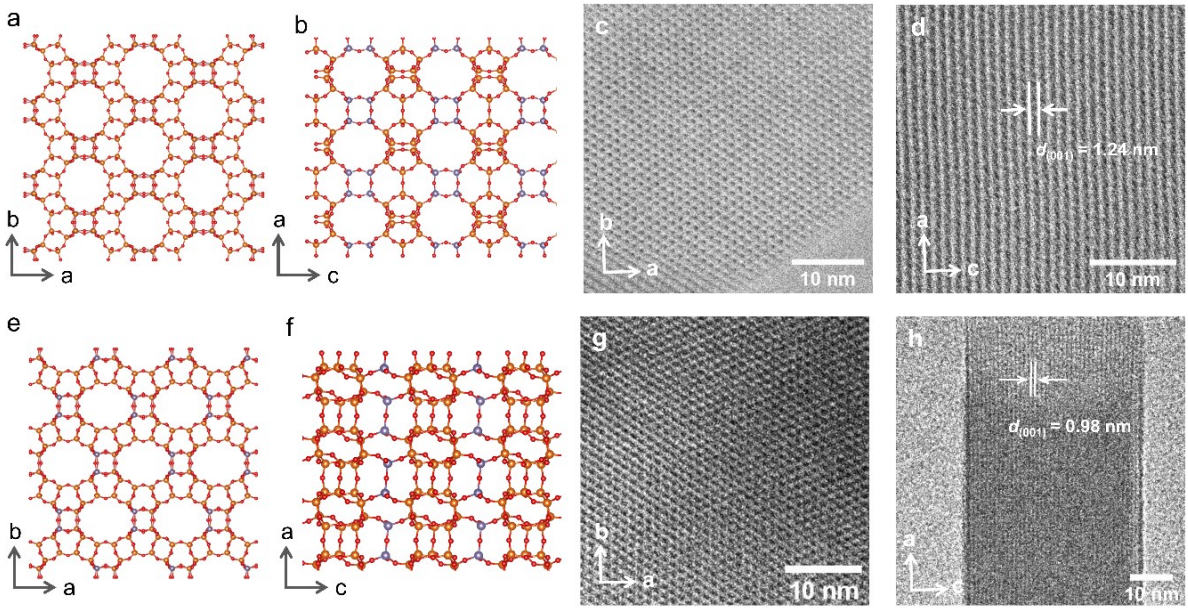


Figure 4.23 Crystallographic models of IWR zeolite in the (a) a×b ("top") and (b) a×c ("side") projections demonstrating the layer plane and connectivity between layers, respectively. The corresponding HRTEM images of initial **IWR** in the (c) *a*×*b* and (d) *a*×*c* projections. Crystallographic models of IPC-17 zeolite in the (e) *a*×*b* ("top") and (f) *a*×*c* ("side") projections showing the maintenance of layer structure but change in the interlayer connectivity. HRTEM images of IPC-17 zeolite corresponding to *a*×*b* (g) and *a*×*c* (h) projections. The T atoms in the D4Rs and S4Rs are highlighted with dark grey color in the models.

Evolution of Si atoms environment in the process of **IWR**-to-IPC-17 was studied by $^{29}$Si MAS NMR analysis. Fully condensed framework of **IWR** contains mainly $Q^4$ Si atoms (at ~ 107 and ~ 115 ppm) corresponding to $Si(OT)_4$ (T = Si or Ge) environment and a small

fraction (5 – 10 %) of $Q^3$ atoms (at ~ 101 ppm) corresponding to silanol defects. During *disassembly* step the framework of **IWR** undergoes controllable decomposition to form the IPC-17P layered intermediate resulting in the formation of large fraction of silanols ($Q^3$, at ~ 101 ppm). Besides, a deeper framework deconstruction was also observed a small signal at ~ 92 ppm corresponding to $Q^2$ Si atoms ($Si(OSi)_2(OH)_2$) was detected in IPC-17P intermediate. This phenomenon is presumably related to the transformation of $Q^3$ sites presented in the initial zeolite (i.e. $Q^3 \rightarrow Q^2$ transition for deficient sites instead of $Q^4 \rightarrow Q^3$ for initially non-deficient sites). The following calcination of IPC-17P leads to a decrease in the intensity of $Q^3$ signal, reflecting the condensation of silanols {Si−OH + HO−Si → Si−O−Si}, and formation of IPC-17 zeolite with dominant fraction of $Q^4$ atoms. Difference in the positions of $Q^4$ peaks in the starting and final zeolites can be related to the change in the chemical composition and thus the environment of Si atoms at framework positions surrounded either by $x$Si + (4 − $x$)Ge (in **IWR**) or mostly by 4Si (in IPC-17).

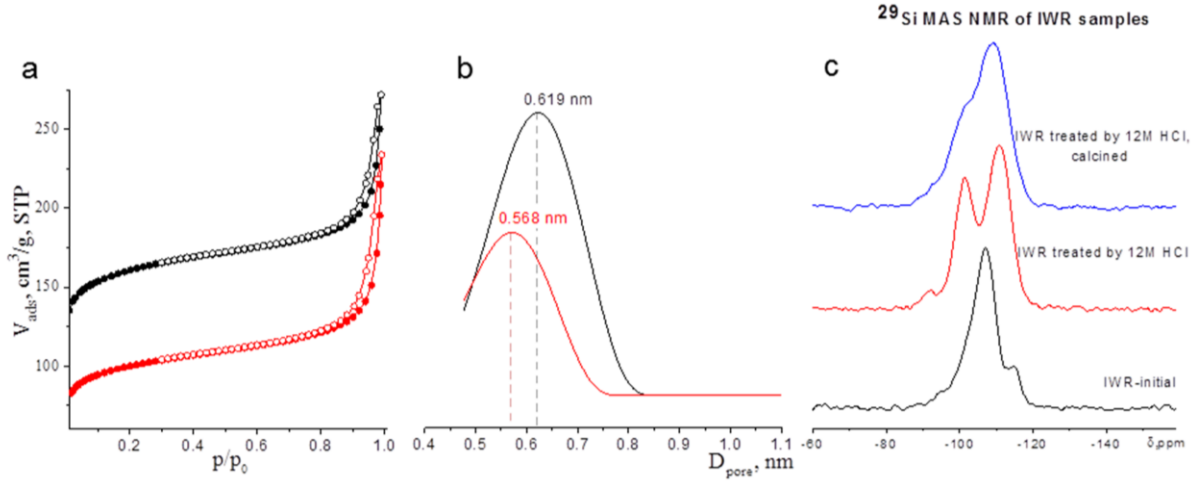


Figure 4.24 (**a**) $N_2$ adsorption/desorption isotherms for parent **IWR** (black) and daughter IPC-17 zeolites (red); (**b**) pore size distribution for initial **IWR** (black) and final IPC-17 (red); (**c**) $^{29}$Si MAS NMR spectra of **IWR**, intermediate IPC-17P, and IPC-17 samples.

### 4.2.2.4 Summary

In this section, we present the synthesis of a new zeolite IPC-17 with 12×8×8-ring pores derived from **IWR** (12×10×8-ring pores) using the ADOR protocol. To improve the layer stability for the structural transformation during the ADOR treatment, several strategies in the *assembly* step, including either individual approaches or combination of F-stabilization, seeding method, and alteration of SDA, were applied. Finally, a well crystalline IPC-17 zeolite was obtained and thus the family tree of ADOR-derived zeolites is expanded with the

new branch related to the **IWR** as the parent zeolite. Despite only one representative of this branch was found up to now, this work shows the feasibility of ADOR transformation for zeolites with porous system propagated in all three directions to the altered and previously unknown zeolites. These findings can help in the design of novel derivatives of further potential families of zeolites produced via ADOR approach, such as **ITR** and **ITH** zeolites (10×10×9-ring pores).

## 4.3 Isomorphous substitution in CHA for separation of $CO_2/CH_4$

Chabazite (coded as **CHA**), a typical small-pore zeolite (~ 3.8×3.8 Å), has been widely studied for separation of $CO_2/CH_4/N_2$ gas mixtures. Chemically flexibility in **CHA** framework allows the introduction of heteroatoms into its framework. However, there exists no report yet revealing the influence of the interaction between the **CHA** framework and the guest molecules on the performance of separation of $CO_2/CH_4$. To minimize the contribution of extra-framework cations, which can strongly affect the adsorption of $CO_2$ [192, 193], zeolite **CHA** in the protonic form is studied for the evaluation of gas separation efficiency. Herein, in this section, we present the preparation of heteroatoms substituted **CHA** by seeded growth and its utilization for separation of $CO_2/CH_4$.

### 4.3.1 Seeded growth of isomorphously substituted CHA

Structure/framework flexibility of zeolite **CHA** enables the framework Si atoms to be isomorphously substituted by several $T^{III}$ and $T^{IV}$ atoms, such as B, Ga, Al, Ti etc. However, synthesis of heteroatoms substituted **CHA** in protonic form by the conventional hydrothermal method is still challenging and time-consuming due to its slow crystallization kinetics. Liu *et al.* calculated the substitution energy in **CHA** and revealed that the energy required for the synthesis of B-, Ga-, and Fe-CHA is much higher than that of Al-CHA [194]. Besides, the energy for the substitution of **CHA** in protonic form is significant higher than in other cationic forms ($Na^+ < K^+ < Li^+ < NH_4^+ < H^+$). Notably, the absolute substitution energies for B- and Fe-CHA in protonic forms are positive, resulting in an unfavorable thermodynamic for the preparation of these zeolites. Therefore, B-CHA in protonic form with good crystallinity can be obtained in 15 days [195]. Many synthesis protocols were developed to facilitate the crystallization, i.e., microwave radiation [196], ultrafast continuous-flow synthesis [37], seeding method [197], and UV irradiation [34]. Among them, a small amount of pre-

synthesized material as crystal growth seeds has been proven to direct the crystallization towards the target material and accelerate the crystal growth rate [39, 198, 199]. However, no results are reported so far for direct synthesis of isomorphously substituted **CHA** zeolites by seeded growth.

#### 4.3.1.1 Phase purity

Four different heteroatoms incorporated **CHA** (M-CHA, M = B, Al, Ga, and Ti) were synthesized by a direct hydrothermal synthesis with the assistance of Si-CHA seeds, prepared according to the ref. [179]. When the Si-CHA was introduced into the synthesis gel, the resulting time for the crystallization of M-CHA is greatly decreased compared to the previous results (Table 4.1). For instance, the required time for synthesis of B-CHA was reduced to 1 day in the presence of Si-CHA seeds, while it was reported to be 15 days without seeds [195].

Table 4.1 Chemical compositions, synthesis time, and textural properties of M-CHA (M = Si, B, Al, Ga, and Ti).

| Samples | Gel | | Final products | | | | Reference | | |
|---|---|---|---|---|---|---|---|---|---|
| | SSi/M | SSi/M | $S_{BET}$ ($m^2\ g^{-1}$) | $V_{micro}$ ($cm^3\ g^{-1}$) | Time (h) | Si/M | $S_{BET}$ ($m^2\ g^{-1}$) | Time(h) | |
| Si-CHA | ∞ | ∞ | 647 | 0.30 | 48 | ∞ | 602 | 48 | [179] |
| Al-CHA | 20 | 6.6 | 665 | 0.31 | 24 | 7.5 | / | 144 | [200] |
| B-CHA | 5 | n.d. | 682 | 0.28 | 24 | / | / | 360 | [195] |
| Ga-CHA | 20 | 5.7 | 687 | 0.30 | 72 | 23 | / | 120 | [201] |
| Ti-CHA | 20 | 9.1 | 723 | 0.31 | 30 | / | / | 96 | [16] |

/ means unknown data from the previous reports.

The Si/M ratio was set as 20 in the initial synthesis gel for Al-, Ga-, and Ti-CHA while 5 for B-CHA. Generally, the incorporation of B into the framework of zeolites is not easy because of the high mobility of B species, and thus low Si/B ratio is required. ICP-OES was used to analyze the chemical composition of the final products (Table 4.1). Ga- and Al-CHA has a Si/M ratio of 25.7 and 16.6, respectively. Besides, a high Si/Ti ratio (~ 50) in Ti-CHA is obtained compared to that of Al- and Ga-CHA due to the unfavorable kinetics of Ti incorporation into zeolites [5]. The **CHA** phase purity was confirmed using XRD patterns

(Figure 4.25), revealing the maintenance of **CHA** structure during the isomorphous substitution.

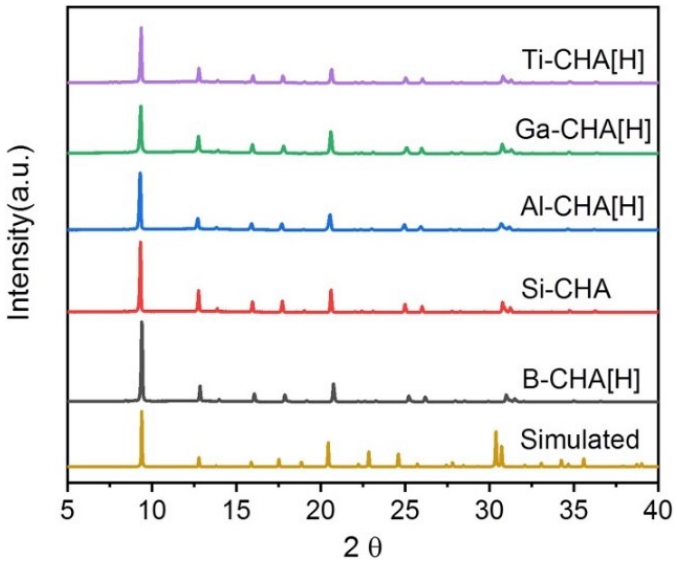


Figure 4.25 XRD patterns of M-CHA (M = Si, B, Al, Ga, and Ti) and simulated **CHA**.

### 4.3.1.2 Morphology and textural properties

The effect of heteroelement nature on the shape and size of M-CHA crystals was evaluated by SEM (Figure 4.26). Cubic crystal with ~ 6 μm is observed in Si-CHA, which is in a good agreement with the previous report [199]. The introduction of B or Ti into **CHA** does not alter the shape of crystals compared to Si-CHA, but their respective sizes of crystals decrease to 4 μm and 2 μm. Noticeably, Ti-CHA crystals have a smooth surface with no additional attached particles, evidencing an absence of undesirable $TiO_2$ particles which is typically observed in the previous report [202]. Contrary to the cubic feature for B- and Ti-CHA, both Ga-CHA and Al-CHA tend to assemble into small spherical particles with crystal sizes of 0.5 and 3.5 μm, respectively.

$N_2$ adsorption/desorption isotherm was employed to determine the effect of incorporated heteroelements on the porosity of M-CHA (Figure 4.27). All **CHA** samples show a similar type I isotherms, typical for microporous materials exhibiting similar values of the micropore volume (0.28 – 0.31 $cm^3\ g^{-1}$) and BET area (647 – 726 $m^2\ g^{-1}$, Table 4.1). This indicates similar textural properties after incorporation of heteroatoms into the **CHA** framework.

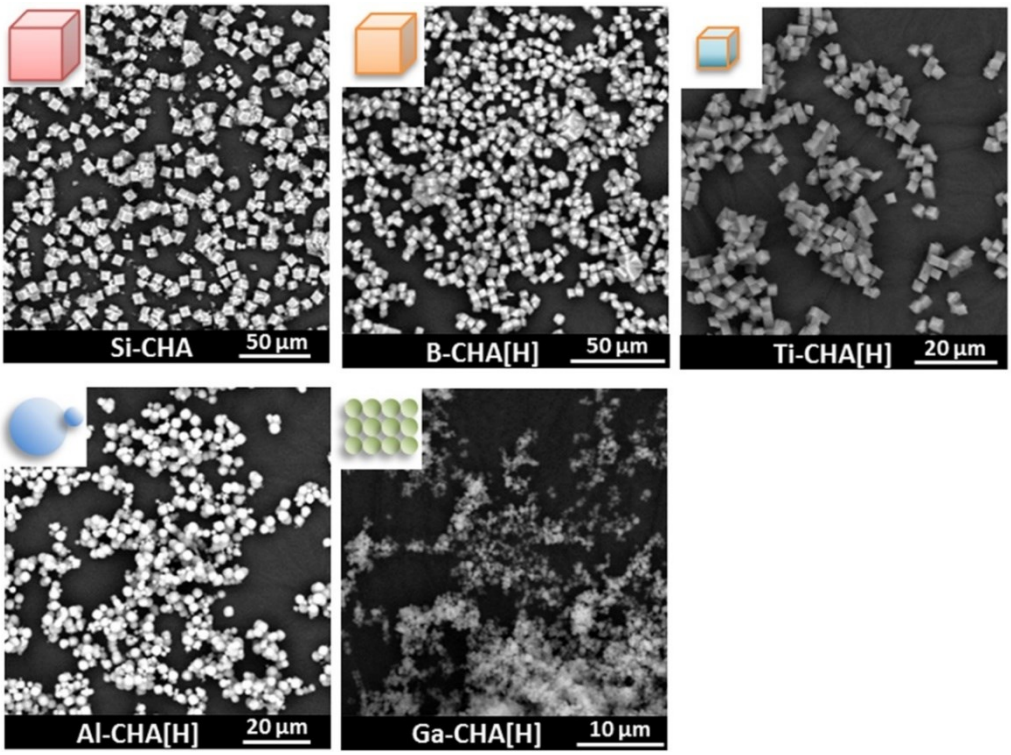


Figure 4. 26 SEM images of M-CHA (M = Si, B, Al, Ga, and Ti), insert diagram is the schematic presentative of crystal shapes.

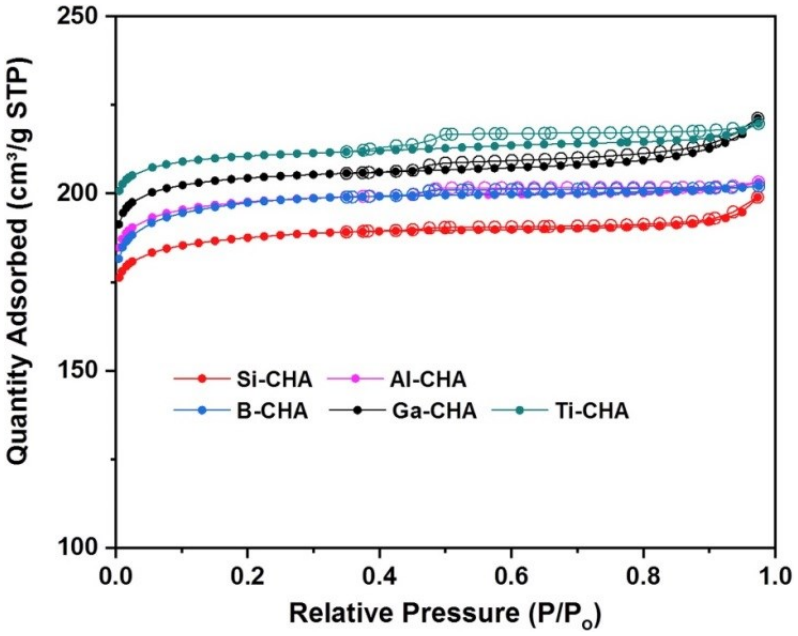


Figure 4.27 Nitrogen adsorption (●) and desorption (○) isotherms of M-CHA (M = Si, B, Al, Ga, and Ti).

### 4.3.1.3 FTIR spectroscopy

FTIR spectroscopy was employed to determine the state of heteroatoms in M-CHA zeolite according to the region of framework skeleton vibrations in the spectra (Figure 4.28 A).

In comparison with Si-CHA, Ga-CHA shows a red shift of asymmetric vibration bands (~ 1080 $cm^{-1}$) to lower frequencies, suggesting a successful substitution of Si with Ga atoms [203]. In the case of B-CHA, two new bands appeared at 913 and 1390 $cm^{-1}$, corresponding to the respective stretching vibration band of Si–O–B moiety and asymmetric stretching mode of B–O bonds of $BO_3$ units in $D_{3h}$ symmetry [204]. In addition, a stretching vibration band of Ti–O–Si moiety (~ 960 $cm^{-1}$) is also observed in Ti-CHA, indicating a tetrahedrally coordinated Ti [205].

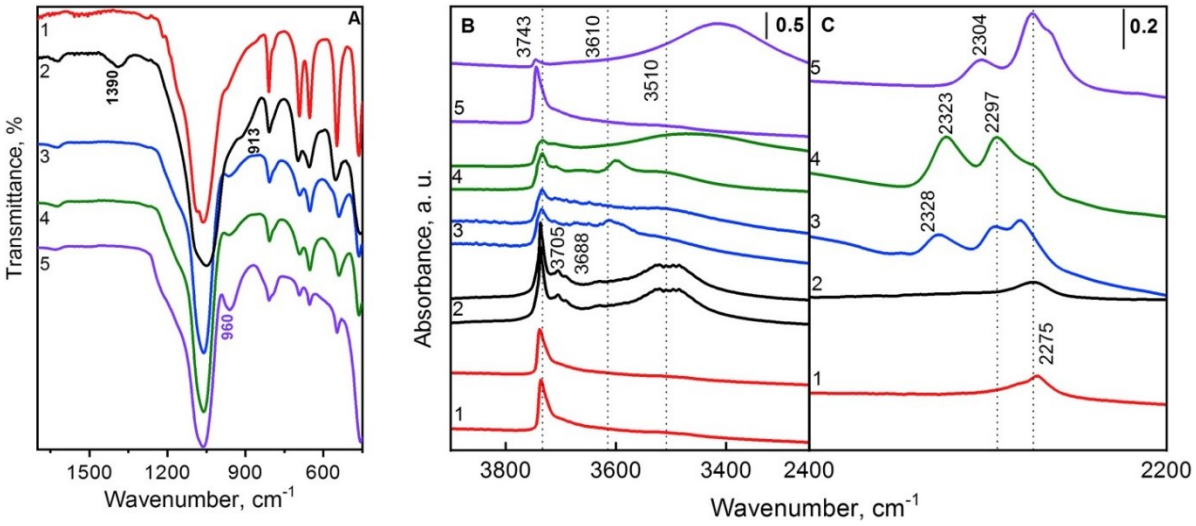


Figure 4.28 FTIR spectra of Si-CHA (1), B-CHA (2), Al-CHA (3), Ga-CHA (4), Ti-CHA (5) zeolites: (**A**) spectra region of the framework skeleton vibrations; (**B**) region of hydroxyl vibrations before (bottom) and after adsorption (top) of $d_3$-acetonitrile; (**C**) region of $d_3$-acetonitrile vibrations (the spectrum of Ti-CHA is shown after adsorption of an access of acetonitrile, while desorption of physically adsorbed probe molecule followed the adsorption step for Si-, B-, Ga-, Al-CHA).

The nature of OH groups in M-CHA zeolites, which reflects the state of incorporated heteroatoms, was also studied by recording the respective FTIR spectra through adsorption and desorption of $d_3$-acetonitrile (AN) (Figure 4.28B). Ti- and Si-CHA exhibit only one band at 3743 $cm^{-1}$ corresponding to the external silanol groups. In contrast, Ga-, and Al-CHA show an additional band at ~ 3600–3610 $cm^{-1}$, which disappears after adsorption of basic probe AN molecule, confirming the formation of bridging ≡Si ($OH^+$) $M^-$≡ (M = Al, Ga) groups and its acid character [206]. B-CHA shows 4 absorption bands in 3800–3200 $cm^{-1}$ region, in accordance with previous FTIR studies on borosilicate zeolites [204]. The band at ~ 3705 $cm^{-1}$ corresponds to the stretching vibrations of Si–(OH)···B, while ~ 3743 $cm^{-1}$ is assigned to the external silanol groups. Moreover, two other bands at ~ 3688 and ~ 3510 $cm^{-1}$ are confirmed to be related to the B species upon hydrolysis of Si–O–B bond [207-209].

Although the borosilicate zeolite exhibits an acid character upon the interaction with pyridine molecule [207], in our case no corresponding bands are traced after adsorption of AN, which is probably caused by weakly acidic strength of Si–(OH)···B groups, which are not sufficient for AN adsorption at room temperature.

In addition, a band at ~ 2304 $cm^{-1}$ relating to the Lewis acid sites is observed for Ti-CHA upon the dose-by-dose adsorption of AN, while 2 additional peaks at 2265 and 2275$cm^{-1}$ correspond to AN physisorbed and chemisorbed at silanol groups. Ti-CHA showed a lower Δυ(C≡N) than that for Ga- and Al-CHA, revealing a weaker interaction between AN and Ti-associated Lewis acid sites [210]. Furthermore, this weak strength is also evident from substantial decrease in the band intensity at 2304 $cm^{-1}$ when prolonging the degassing, while the intensities of respective bands for Ga- and Al-associated acid maintained.

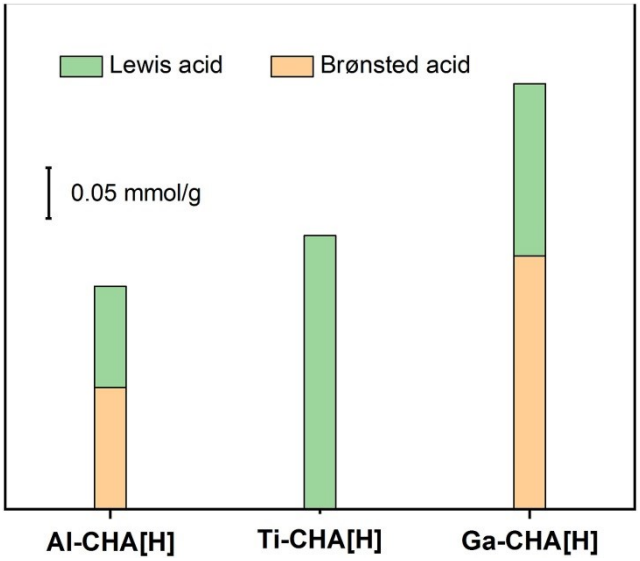


Figure 4.29 Concentration of acid sites in the Al-, Ti-, and Ga-CHA zeolites determined using FTIR spectroscopy of adsorbed $d_3$-acetonitrile.

Finally, the acidity in M-CHA was evaluated and it follows the sequence: Al-CHA < Ti-CHA < Ga-CHA (Figure 4.29). Only Lewis acid centers were observed in Ti-CHA (0.27 mmol $g^{-1}$), while both Al- and Ga-CHA showed Brønsted (0.12 and 0.25 mmol $g^{-1}$, respectively) and Lewis (0.10 and 0.17 mmol $g^{-1}$, respectively) acid centers. Therefore, based on analysis of the FTIR spectra measured for all samples, successful isomorphous substitution of Si by heteroatoms (Ti, Al, Ga, and B) in zeolite **CHA** is achieved.

#### 4.3.1.4 UV-vis spectroscopy

Direct hydrothermal synthesis of titanosilicate zeolites often leads to the formation of undesirable $TiO_2$ phase presented at extra-framework sites [202, 211]. The presence of $TiO_2$ was also observed in the direct synthesis of Ti-CHA [16], even at a very low Si/Ti ratio in the synthesis gel (Si/Ti = 50). Noticeably, no undesirable $TiO_2$ was observed upon the substitution of Si with Ti in the framework of **CHA** via direct hydrothermal synthesis by an assistance of seeds. As shown in Figure 4.30, the only adsorption band at ~ 220 nm was observed in Ti-CHA zeolite, which is indicative of charge transfer from oxygen to the empty *d* orbitals of $Ti^{4+}$ ions, indicating the existence of isolated tetrahedrally coordinated Ti in the framework [212]. In addition, no bands at ~ 330 nm relating to the penta- or hexacoordinated extra-framework Ti species were observed [213, 214]. These results indicate that Ti atoms has been successfully incorporated into the framework of **CHA** zeolite in our presented Ti-CHA synthesized using Si-CHA as crystal seeds.

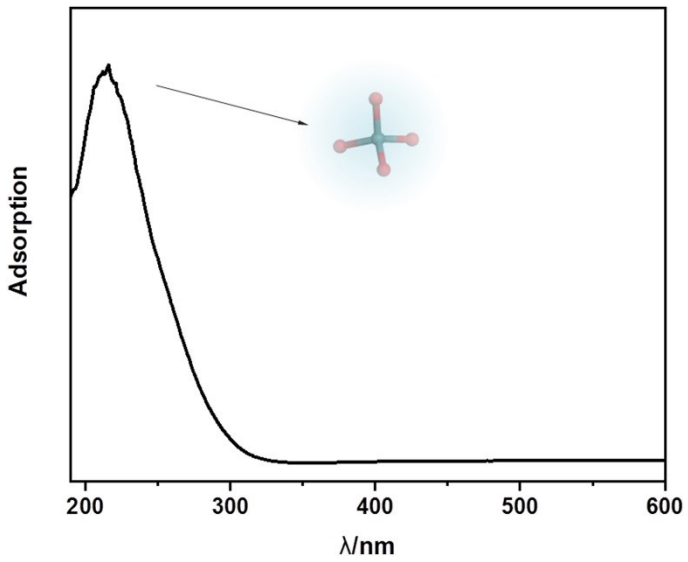


Figure 4.30 UV-vis spectrum of Ti-CHA, adsorption band at ~ 220 nm can be assigned to tetrahedrally coordinated framework Ti (insert diagram).

### 4.3.2 M-CHA for gas separation of $CO_2/CH_4$

#### 4.3.2.1 Geometry of 8-ring in M-CHA

The incorporation of heteroelements with different properties into **CHA** zeolite frameworks resulted in the alteration of zeolite frameworks and thereby affecting the gas molecules adsorption. Rietveld refinement (done by D. N. Rainer at U. St Andrews) against

the powder X-ray diffraction (PXRD) was employed to analyze the changes of structures (Figure 1-2 in Appendix I). The Rietveld refinement of PXRD patterns of M-CHA adopting the space group $R\bar{3}m$ confirmed that single-phase M-CHA zeolites were synthesized. Table 4.2 listed the unit cell and fitting parameters of each M-CHA before and after dehydration were found in. An increase in *a, c* lattice parameters and unit cell volume was observed in Si- and Al-CHA after dehydration, while B- and Ti-CHA show opposite patterns, suggesting the different influences of framework composition on the structure behavior under high temperature. In addition, Ga-CHA shows an increase in *a* parameter and a decrease in *c* parameter after dehydration. A decrease in *a* parameter and an increase in *c* parameter after dehydration were reported for nanosized aluminosilicate **CHA** zeolites with different extra-framework cations ($Na^+$, $K^+$, and $Cs^+$) [161]. This difference is probably related to the different mobility of the extra-framework cation, resulting in different behavior of unit cell parameters after removal of water in the zeolite cavity.

Table 4.2 Unit cell and Rietveld refinement parameters for M-CHA (M = Si, B, Al, Ga, and Ti) samples before (suffix -h) and after dehydration (suffix -d) at 573 K under $9\times10^{-4}$ mbar for 24 hours. Parameters of hydrated samples are obtained from Le Bail refinements; those of dehydrated samples from Rietveld refinements.

| Samples | *a* [Å] | *c* [Å] | Volume [Å$^3$] | $R_{exp}$, $R_{wp}$ | $\chi^2$ |
|---|---|---|---|---|---|
| Si-CHA-d | 13.54718(17) | 14.7562(2) | 2345.32(6) | 0.0466, 0.0890 | 3.647 |
| Si-CHA-h | 13.52205(17) | 14.7325(3) | 2332.88(6) | 0.0484, 0.0664 | 1.856 |
| B-CHA-d | 13.4765(2) | 14.6970(3) | 2311.60(7) | 0.0466, 0.960 | 4.253 |
| B-CHA-h | 13.4784(2) | 14.7272(3) | 2317.03(7) | 0.0679, 0.0888 | 1.766 |
| Al-CHA-d | 13.57632(18) | 14.8096(3) | 2363.95(6) | 0.0334, 0.0563 | 2.835 |
| Al-CHA-h | 13.56855(15) | 14.7635(2) | 2353.90(5) | 0.0337, 0.0455 | 1.715 |
| Ga-CHA-d | 13.5613(2) | 14.7479(3) | 2348.90(7) | 0.0326, 0.0492 | 2.270 |
| Ga-CHA-h | 13.55347(18) | 14.7553(3) | 2347.36(6) | 0.0305, 0.0400 | 1.357 |
| Ti-CHA-d | 13.54904(18) | 14.7454(3) | 2344.26(6) | 0.0455, 0.0957 | 4.423 |
| Ti-CHA-h | 13.5515(2) | 14.7539(3) | 2346.47(7) | 0.0693, 0.0925 | 1.594 |

Figure 4.31 shows the geometry of 8-ring pore windows in M-CHA considering that their eccentricity is not zero (i.e. considering that the aperture can be described as an ellipse

not circle and thus require two size parameters measured as O−O distances). Classical Al-CHA zeolite possesses a pore size of 3.84 × 3.89 Å almost without any distortion of the circle geometry (8-ring pore). Moreover, Al-CHA has the largest unit cell volume (0.8 % higher than that of Si-**CHA**) among the prepared zeolites.

Ti-CHA has a similar pore size (3.80 × 3.90 Å) to Si-CHA, which can be correlated with the low content of Ti (Si/Ti = 49 reflecting the average presence of less than one Ti atom in each unit cell). Among different zeolites, the distance of O−O in B-CHA zeolite along two aperture axes (3.76 × 3.86 Å) are the smallest because B has the smallest ionic radius, which is in line with the trend for the unit cell volume showing 1.4 % lower value than Si-CHA. Moreover, Ti-, Si-, and B-CHA show nearly the same differences (~ 0.1 Å) of O−O distances in two directions, indicating a similar elliptical distortion of 8- ring. In contrast, the distortion increases from 0.1 to 0.17 Å upon the introduction of Ga. The pore size in one direction decreases to 3.76 Å while the other increases to 3.93 Å compared with that of Si-CHA. Smaller distortions of the elliptical 8-ring pores and larger unit cell volume benefit the free diffusion of gas molecules.

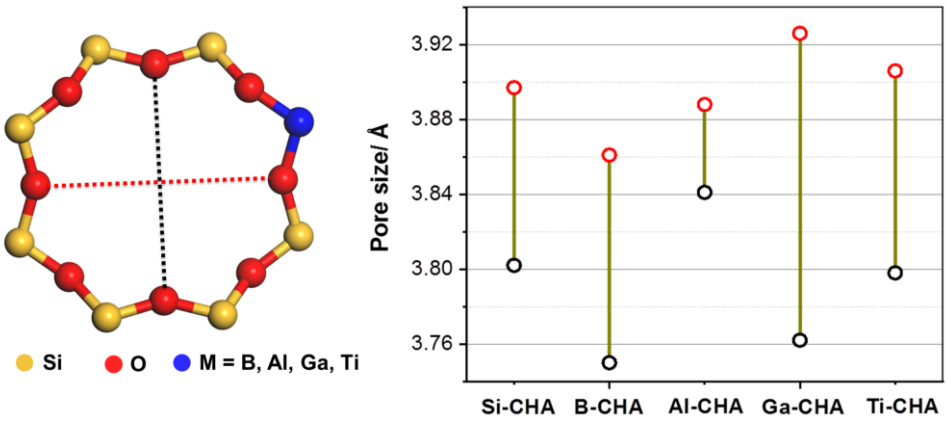


Figure 4.31 Distances between oxygen atoms in two nearly orthogonal directions in 8 MR in substituted **CHA**: (left) schematic representation of 8 MR and evaluated sizes; (right) distances obtained upon structure refinement. Two different kinds of pore sizes are shown by black and red colors (dotted lines on the left figure, circles – on the right).

### 4.3.2.2 Single component adsorption isotherms of $CO_2$ and $CH_4$ on M-CHA

In order to evaluate the zeolite separation ability for $CO_2$ and $CH_4$ mixture, single-component adsorption isotherms of the dehydrated M-CHA (M = Ga, B, Al, Ti, and Si) were measured (collaboration with Prof. R. Bulánek at University of Pardubice), meanwhile, Tóth model was used to fit the adsorption isotherms ($R^2$ = 0.99954 – 0.99999, Table 5 in Appendix

I). Figure 4.32 shows the adsorption isotherms of $CH_4$ and $CO_2$ for different samples at 298, 286 and 273 K in the pressure range of 0 ~ 800 Torr. Uptake of $CH_4$ is significantly lower than that of $CO_2$ for different materials under the same conditions (T, p), which is mainly related to the electron distribution in the molecules and size of the gas molecules. The kinetic diameter of $CO_2$ is smaller than that of the pore mouth (3.3 *vs.* 3.8 Å), allowing it to diffuse freely into the zeolite pores [215]. In addition, although $CO_2$ is a non-polar molecule, its quadrupole moment ($4.3\times10^{-26}$ esu·cm$^2$) allows a stronger electronic interaction between zeolite frameworks and $CO_2$ molecules, hence leading to a larger adsorption capacity of $CO_2$ than $CH_4$ [216, 217]. The strength of these interactions decreases at elevated temperatures. Thus, a drop of adsorption capacity with increasing temperature is observed for both $CO_2$ and $CH_4$ molecules (Figure 4.32). As shown in the literature, $CO_2$ is chemically bonded to the cations in the extra-framework of zeolites and the order of the strength is $H^+ << Li^+ < Na^+ < K^+$ [216, 218]. The adsorption capacity in the protonic form **CHA** samples is lower than the other cation-formed **CHA** [193], as expected.

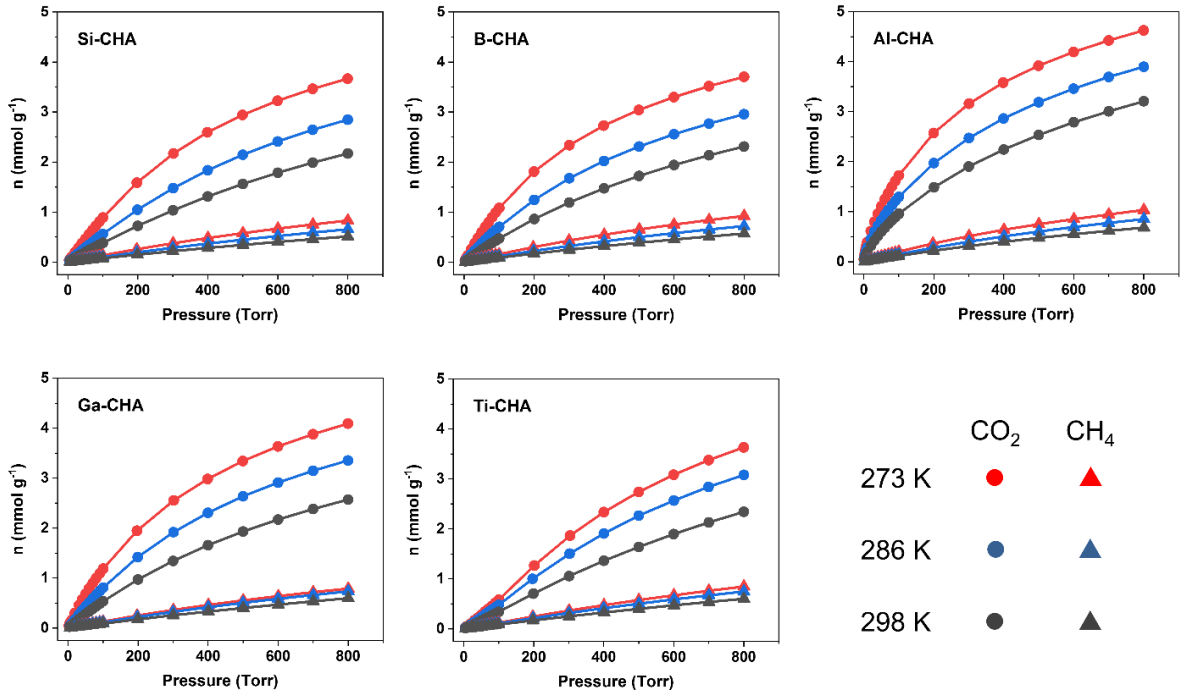


Figure 4.32 Single-component adsorption isotherms of $CO_2$ and $CH_4$ at 273, 286, and 298 K on M-CHA (M = Si, B, Al, Ga, Ti).

Si-CHA is a nonpolar adsorbent due to the absence of permanent framework charge. The incorporation of heteroelements into **CHA** framework can tune its polarity, and thereby

affect the adsorption capability. Thus, the maximum capacities for $CO_2$ adsorption at 800 Torr and 273 K increase from 3.7 (Si-CHA) to 4.6 (Al-CHA) and 4.1 mmol $g^{-1}$ (Ga-CHA). However, similar adsorption isotherms of $CH_4$ and $CO_2$ were observed in B-CHA and Si-CHA zeolites, which can be explained by a relative low loading of incorporated atoms, typical for B. Noticeably, Ti-CHA shows a lower adsorption capacity than Si-CHA sample, especially at low pressure. Therefore, the order of the overall uptake of $CO_2$ over **CHA** zeolites is Ti-CHA < Si-CHA ≈ B-CHA < Ga-CHA < Al-CHA. Moreover, the maximum uptakes for $CH_4$ and $CO_2$ decrease by ~ 40 % after increasing the temperature to 298 K.

#### 4.3.2.3 IAST-predicted $CO_2/CH_4$ selectivity

Ideal adsorbed solution theory (IAST) was used to estimate the selectivity of $CO_2/CH_4$ separation according to the single-component adsorption isotherms [185]. Simulations were performed on the gas mixture with the same amount of $CO_2$ and $CH_4$ at different temperatures (Figure 3 in Appendix I). The trend of IAST selectivity dependence on the temperature is consistent with that of the single-component adsorption, that is, the adsorption capacity and selectivity enhance with decreasing temperature. The estimated results of selectivity (273 K) over different zeolites are shown in Figure 4.33. Si-CHA has homogeneous surface within its channel system. Correspondingly, the selectivity of $CO_2$ over $CH_4$ steadily increases from 6.8 to 10.4 when the pressure goes from 5 up to 800 Torr at 273 K as a result of an increase in the adsorbate-adsorbate interaction strength. The incorporation of heteroelements into **CHA** framework results in the formation of heterogeneous adsorption sites. $CO_2$ molecules preferentially occupy the high-energy adsorption sites at low coverage. As a result, the selectivity of Al-CHA declines rapidly first from 23 to 19 at 0 – 100 Torr. Further increase in pressure to 800 Torr leads to a gradual increase in the selectivity back to 23 due to the increase in the adsorbate-adsorbate interaction strength. Moreover, the decrease in the selectivity is more obvious at high temperatures, indicating that the adsorption of $CO_2$ at high-energy sites is more sensitive to temperature due to the exothermic adsorption process (Figure 3 in Appendix I). In turn, such similar trend has not been observed in Ga-, Ti-, and B-CHA samples, suggesting different dependences of selectivity on the incorporated heteroatoms. This difference of selectivity in these five samples is probably caused by the interaction strength between the zeolite framework and gas molecules and the concentration of incorporated heteroatoms. The order of the overall selectivity is as follows: Ti-CHA < Si-CHA ≈ B-CHA < Ga-CHA < Al-CHA, which is in line with the trend for the single-components adsorption.

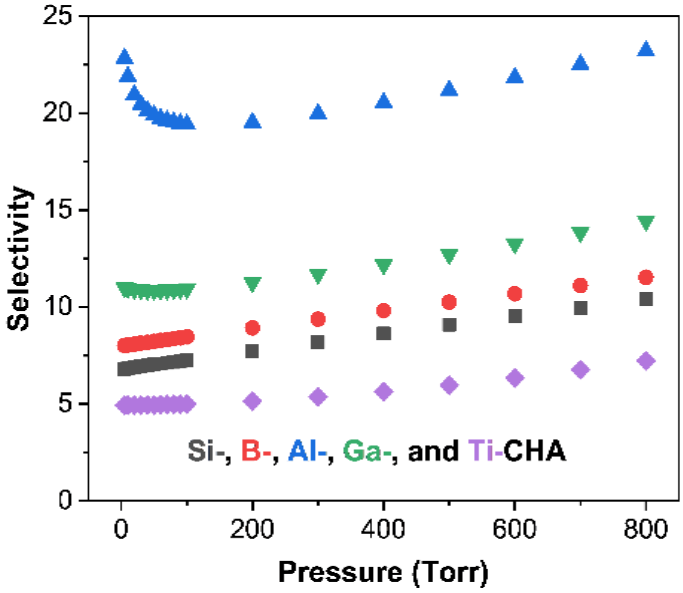


Figure 4.33 IAST predicted selectivity of Si-CHA, B-CHA, Al-CHA, Ga-CHA, and Ti-CHA for gas mixture with $CO_2/CH_4$ = 1.

#### 4.3.2.4 Heat of adsorption

The isosteric heats of adsorption ($Q_{st}$) represent the binding energy for the adsorbed gas molecule at a specific coverage, which can be used to evaluate the interaction between zeolites and gas molecules. A higher value of $Q_{st}$ reflects a stronger interaction between adsorbent and adsorbate. $Q_{st}$ of both $CH_4$ and $CO_2$ for different **CHA** materials are shown in (Figure 4 in Appendix I). $CH_4$ $Q_{st}$ shows almost constant values with ~ 16 kJ $mol^{-1}$ for all samples except for Ti-CHA, which is very similar to reported values for NaY (~ 15 kJ $mol^{-1}$) [219] and siliceous **CHA** (16.8 kJ $mol^{-1}$) [220, 221] zeolites. Figure 4.34 shows the $Q_{st}$ of $CO_2$ for those five samples. Both B- and Si-CHA zeolites exhibit nearly constant values for the $Q_{st}$ of $CO_2$ up to 800 Torr, suggesting a similar binding energy or single site for $CO_2$ adsorption [147]. The value of $CO_2$ $Q_{st}$ for Si-CHA zeolite is about 25 kJ $mol^{-1}$, this can be related to the dispersive interaction between the elements in zeolite frameworks and $CO_2$ molecule [218, 222, 223]. In contrast, Al-CHA shows a significant heterogeneity of adsorption sites indicated by a dramatic decrease in the $Q_{st}$ (31 → 25 kJ $mol^{-1}$) at low pressure range as the most active sites are gradually occupied by $CO_2$. This decline at low pressure is also observed in Ga-CHA (28.3 → 26.6 kJ $mol^{-1}$), while the decrease is not as prominent as in Al-CHA which is probably caused by a weaker acid strength and a lower concentration of Ga in the framework compared with the Al-CHA. Initial $Q_{st}$ (at low $CO_2$ loading) agrees very well with the interaction energies of $CO_2$ molecule with Brønsted acid

sites in various zeolites [224-227]. Noticeably, the values of $CO_2$ $Q_{st}$ achieved over Ti-CHA zeolite progressively increase by 7 kJ $mol^{-1}$ (17 → 24) after dropping to the lowest value at low coverage, suggesting a higher lateral interaction between $CO_2$ molecules than the interaction between adsorbate and adsorbent [216]. Besides, the $CO_2$ $Q_{st}$ for Ti-CHA shows the lowest value among them being in line with the lowest adsorption amount of $CO_2$ and selectivity for Ti-CHA mentioned during discussion of single component adsorption. The trend for $CO_2$ $Q_{st}$ at low coverage is following: Al-CHA > Ga-CHA > B-CHA ≈ Si-CHA > Ti-CHA, which is related to the interaction strength between the zeolite framework and adsorption molecules, recalling the order of M-CHA adsorption capacity.

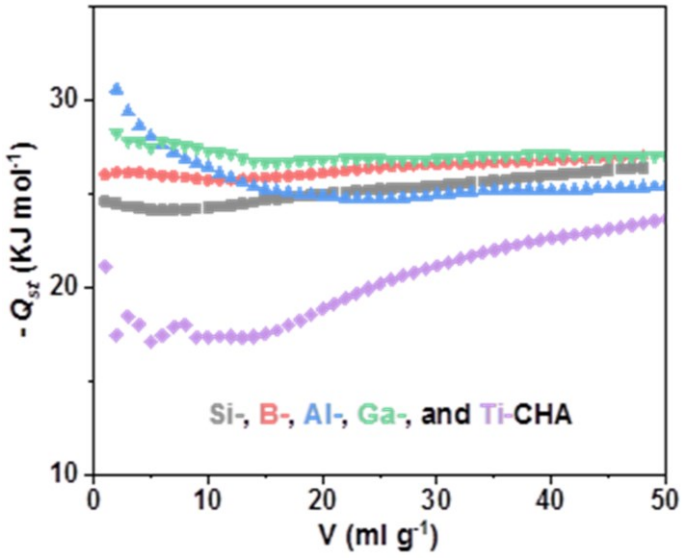


Figure 4.34 Heats of adsorption ($Q_{st}$) of $CO_2$ on proton-form Si-CHA, B-CHA, Al-CHA, Ga-CHA, and Ti-CHA.

#### 4.3.2.5 Host-guest interaction study by FTIR

To better understand the interaction between the adsorbed $CO_2$ molecules and zeolite frameworks, IR spectroscopy was applied. It should be noted prior to discussion of the IR results that in some cases, a surface carbonate ion (in spectral range 1400 – 1700 $cm^{-1}$) may be formed after the adsorption of $CO_2$, i.e. chemisorption occurs [132, 228-230]. In our case, only vibrational bands belonging to molecularly adsorbed $CO_2$ were observed in the spectra (especially vibrational band $\nu_3$ at about 2349 $cm^{-1}$ (asymmetric stretching vibration frequency of gaseous $CO_2$). By interaction with the adsorbent, the $\nu_3$ frequency of the $CO_2$ molecule shifts slightly depending on the type and strength of the interaction. It occurs in the range of about 2365 to 2340 $cm^{-1}$ [138, 231, 232].

Figure 4.35 shows the IR spectra of M-CHA as a function of $CO_2$ pressure in the spectroscopic region of $CO_2$ asymmetric stretching vibration ($\nu_3$). The $\nu_3$ vibrational band is found at 2346 $cm^{-1}$ in the case of Al-CHA and Ga-CHA. This is in very good agreement with the observations of molecularly interacting $CO_2$ with Brønsted acid sites in **FER** [224], MCM-22 [225], ***BEA** [233], and ZSM-5 [234] zeolites. Si-CHA and Ti-CHA not containing extra-framework cations exhibit band at 2341 $cm^{-1}$, which coincide well with the position of the $CO_2$ vibrational band observed in silicalite [232]. This band can be ascribed to the $CO_2$ interacting with the zeolite framework mainly via weak forces. The IR spectra of $CO_2$ adsorbed in B-CHA show the spectral features of the both previously described types of materials. The IR spectra clearly show the presence of both the band at 2346 and the band at 2341 $cm^{-1}$. This can be explained by the significantly smaller number of boron atoms incorporated in the zeolite framework generating Brønsted acid sites in combination with the weaker interaction of $CO_2$ molecules with these cationic sites (adsorption heats for B-CHA are almost the same as for Si-CHA). As a result, $CO_2$ molecules interacting dispersedly are then populated together with electrostatically interacting adsorption complexes ($CO_2$··· H−O≡) at Brønsted acid sites.

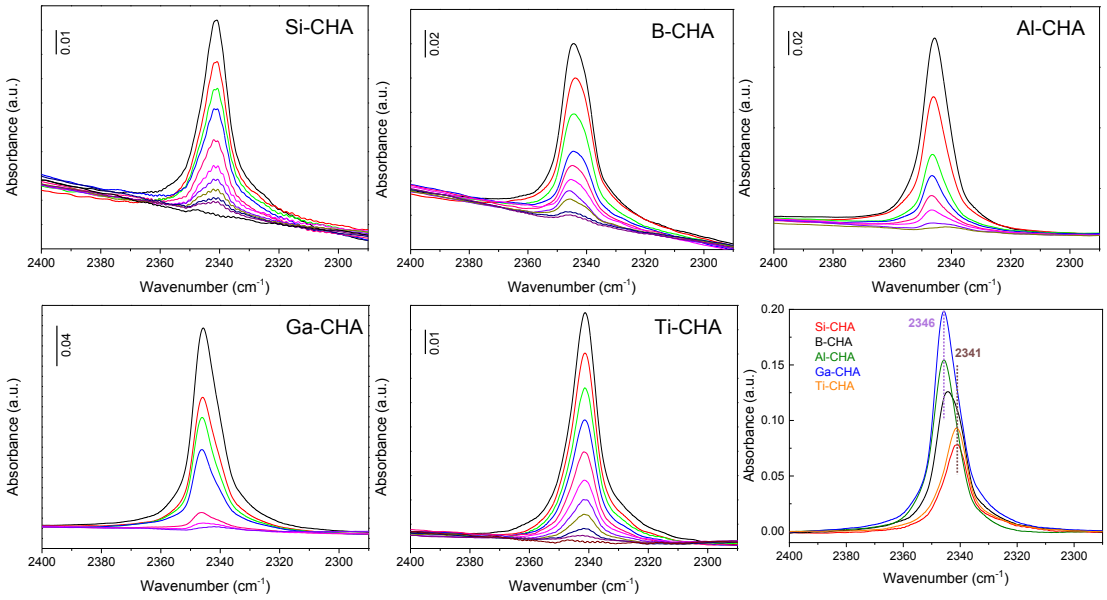


Figure 4.35 Representative spectra of $CO_2$ adsorbed on M-CHA (M = B, Al, Ga, Si, and Ti) as a function of $CO_2$ pressure (from 0.2 to 8 Torr from bottom to top presented by the colorful lines). Comparison of the adsorbed $CO_2$ asymmetric stretching vibration ($\nu_3$) at 8 Torr at room temperature on all M-CHA (bottom right).

The intensities of $\nu_3$ band increase with increasing $CO_2$ dosage (Figure 4.36a). The $\nu_3$ band intensity displayed against $CO_2$ equilibrium pressure (so-called "optical" isotherm) resembles the low-pressure part of volumetric isotherms. In accordance with volumetric measurements, the order of the samples according to their adsorbed amount of $CO_2$ at 10 Torr from the highest to the lowest is as follows: Al-CHA > Ga-CHA > B-CHA > Si-CHA ≈ Ti-CHA. The samples equilibrated with $CO_2$ (8 Torr) were then subjected to desorption at the same temperature (RT) by dynamic evacuation using turbomolecular pump. From the time-resolved IR spectra of individual samples it is evident that desorption of $CO_2$ proceeds very quickly and within 4 – 5 minutes $CO_2$ is completely removed from the samples (Figure 5 in the Appendix I). The band intensities decrease exponentially with time (Figure 4.36b), indicating a first-order kinetic. The rate constants determined from the dependence of the logarithm of the intensity vs. time (Figure 4.36c) have values ranging from $8\times10^{-3}$ $s^{-1}$ to $11\times10^{-3}$ $s^{-1}$. The order of the samples according to the increasing size of the rate constant is as follows: Al-CHA ($8.58\times10^{-3}$ $s^{-1}$) ≈ Ga-CHA ($7.96\times10^{-3}$ $s^{-1}$) < B-CHA ($10.66\times10^{-3}$ $s^{-1}$) ≈ Si-CHA ($10.99\times10^{-3}$ $s^{-1}$) ≈ Ti-CHA ($11.01\times10^{-3}$ $s^{-1}$), which is in accordance with the adsorption heats determined from volumetric measurements.

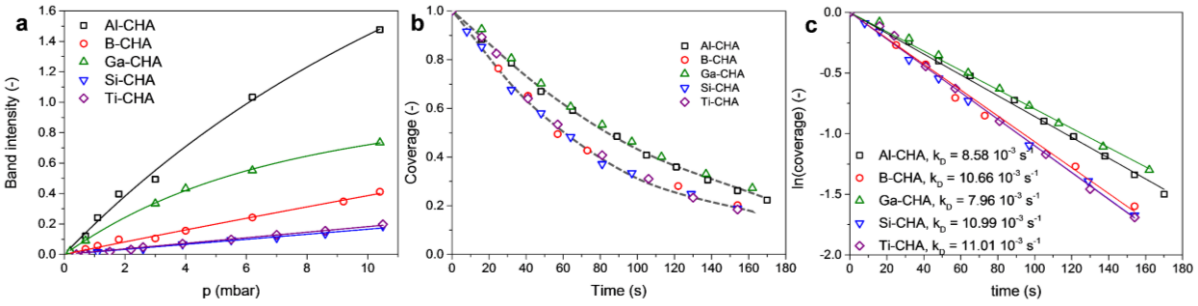


Figure 4.36 Adsorption isotherms of $CO_2$ on M-CHA (M = B, Al, Ga, Si, and Ti) at 298 K derived from IR spectra displayed in Figure 4.35 (**a**). Time dependence of the adsorbed $CO_2$ asymmetric stretching vibration ($\nu_3$) during evacuation at 298 K (**b**) derived from IR spectra displayed in Figure 5 in the Appendix I. First order kinetics plot derived from data in middle panel (**c**).

### 4.3.3 Summary and Perspectives

Direct hydrothermal synthesis of isomorphously substituted M-CHA (M = B, Al, Ga, and Ti) has been successfully performed in the presence of Si-CHA seeds. The crystallization kinetics for incorporation of heteroatoms into **CHA** is accelerated with the help of seeds additive and the required time for the preparation of M-CHA with high crystallinity was

greatly decreased without any textural changes. The successful incorporation of heteroelements in **CHA** framework was confirmed by FTIR and UV-vis spectroscopies.

The nature of the **CHA** framework is shown to affect its ability for gas separation, thus isomorphous substitution of Si with heteroatoms (Al, B, Ga, and Ti) allows tuning the framework-adsorbate interaction. The crystallographic structure of the corresponding M-CHA zeolites, in particular the geometry of the 8-ring, is altered when heteroatoms are incorporated into **CHA**. Al-CHA has pore size of 3.84×3.89 Å with nearly no distortion of 8-ring circle geometry, while Ga-CHA possesses largest distortion (3.76×3.93 Å). B- and Ti-CHA show almost the same 8-ring geometry as Si-CHA (3.80×3.90 Å). The resulting M-CHA zeolites exhibit notable $CO_2$ uptake capacity and selectivity. Largest adsorption amount of $CO_2$ and selectivity of $CO_2$ over $CH_4$ was observed in Al-CHA among these five samples. Contributed by both the geometry of 8-ring in **CHA** and interaction between zeolite hosts and guest molecules, the order of separation ability is Ti-CHA < Si-CHA ≈ B-CHA < Ga-CHA < Al-CHA. The separation ability of zeolites is expected to be further improved by optimization of both the framework composition and the type of extra-framework cations. Optimizing the chemical compositions of both the framework and extra-framework cations of **CHA** zeolite may open the way for further improvement in the separation ability of zeolites.

# 5. Conclusions

This thesis was devoted to the understanding of mechanistic features of zeolites formation and to the development or modification of synthetic protocols aimed in the controllable structural transformations of zeolites possessing anisotropic lability. These findings described in the thesis include the understanding of zeolite crystallization mechanism (studied in the **AST**-type zeolite systems), expansion of ADOR approach for synthesis of new zeolites (preliminary designated as IPC-17 and IPC-18 until being potentially approved by structural commission of International Zeolite Association), and tuning the framework compositions of zeolites of **CHA** topology for gas separation.

An unusual zeolite crystallization mechanism comprising the formation of bulk amorphous intermediate species and their crystallization (so-called reversed crystal growth as opposed to the classical crystal growth mechanism) was described for the first time; the fundamental factors that control the crystallization pathway and crystal growth rate were comprehensively investigated. If the concentration of structure-directing agent reaches a particular critical value, interaction of corresponding organic cations with silica precursors drives the agglomeration of small particles into large amorphous aggregates at the very early stage before crystallization starts. The concentration of F ions, another key factor, determines the rate of crystal growth. Thus, a zeolite crystallization mechanism was shown to be controllable under particular conditions providing the possibility to switch the direction of crystallization between the classical and reversed crystal growth mechanisms. In particular, for the synthesis of **AST** zeolite utilized as a model system, at low $x$ = SDA/$SiO_2$ ratio ($0.3 \leq x \leq 0.4$) the crystal growth follows the classical route, while it switches to the reversed crystal growth mechanism at high $x$ values ($0.5 \leq x \leq 0.7$).

Two new zeolites were prepared through the ADOR (*assembly-disassembly-organization-reassembly*) approach proven to be an efficient strategy for controllable structural transformation of zeolites. Modifications of the conventional ADOR protocols were carried out for the realization of the ideas that

i) particular types of zeolite frameworks, *e.g.* **IWR**, undergoes successfully (by means of the uniqueness of the final zeolite topology and high crystallinity of the material) structural transformation via ADOR mechanism only if certain features of the initial germanosilicate zeolites are implemented. In particular, the traditionally prepared **IWR** zeolite suffers from the layer instability under harsh conditions during the ADOR

transformation leading to a structural collapse. To improve the layer stability, five synthetic strategies, including variation of chemical composition, stabilization with fluoride groups, seeding method, alteration of the SDA structure, and their combinations were developed. As a result of optimized sequence of disassembly-reassembly transformations, a new IPC-17 zeolite with a 12×8×8-ring pore system was obtained.

ii) for zeolites suffering from undesired re-intercalation/reconstruction resulting in preservation of initial zeolite topology after application of conventional ADOR (*e.g.* in the case of **IWW** zeolite), control of the mass transport in the zeolite pores during the disassembly in the acid solution is decisive. As a consequence, the vapor-phase transport (VPT) technique was developed for accurate deconstruction of initial framework and selective removal of Ge atoms that was achieved through a vapor mode of operations typically performed in solutions, such as an interaction with acid and water molecules, removal of the atoms from the framework and their relocation from the interlayer space. Finally, a new zeolite IPC-18 was prepared starting from the **IWW** zeolite, while it was inaccessible by the conventional ADOR protocol up to now. Besides, the VPT method can also be applied for other germanosilicates, such as **UTL**, **UOV**, in order to obtain the products of structural transformations different to those of conventional ADOR approach.

To evaluate the influence of the zeolite framework nature on the performance in gas separation, a series of **CHA** materials with different framework compositions were prepared through the isomorphous substitution by heteroelements. M-CHA (M = Si, B, Al, Ga, and Ti) zeolites not containing metal ions in ion-exchange positions were prepared by the seeding method. The introduced heteroatoms are located in the **CHA** framework, which was confirmed by the diffraction and spectroscopy techniques (XRD, FTIR, UV-vis, and solid-state MAS NMR). The obtained materials showed distinct separation ability when applied for $CO_2/CH_4$ gas mixture (selectivity decreases in order Al-CHA > Ga-CHA > B-CHA ≈ Si-CHA > Ti-CHA) contributed by both the geometry of 8-ring pores in **CHA** and interaction between zeolite hosts and guest gas molecules.

All in all, in this thesis the fundamental features determining i) the zeolites crystallization pathway and crystal growth rate, ii) the success of ADOR transformation towards new zeolite structures, and iii) the application potential (i.e. selectivity in gas separation) of designed zeolites were revealed. I hope, the findings of this thesis will further help to move forward the fast-developing area of zeolite design and application. In particular, through the controlling the chemical composition in the reaction mixture (*e.g.* T atoms ratio,

SDA concentration, mineralizing agent, and water content), the crystal morphology, chemical composition and spatial distribution of atoms, textual properties of zeolites can be designed. Besides, the development of new techniques for the treatment of water-sensitive zeolites, particular for germanosilicate zeolites containing *d4r/d3r*s distributed in several directions such as ITT, IRR etc., in the ADOR approach is a challenge for the future.

# 6. References


[1] E.M. Flanigen, J.C. Jansen, H. van Bekkum, Introduction to zeolite science and practice, Elsevier 1991.

[2] R.M. Barrer, Zeolites and their synthesis, Zeolites 1 (1981) 130-140.

[3] C.S. Cundy, P.A. Cox, The hydrothermal synthesis of zeolites: history and development from the earliest days to the present time, Chem. Rev. 103 (2003) 663-702.

[4] R. Xu, W. Pang, J. Yu, Q. Huo, J. Chen, Chemistry of zeolites and related porous materials: synthesis and structure, John Wiley & Sons 2009.

[5] J. Čejka, R.E. Morris, P. Nachtigall, Zeolites in catalysis: properties and applications, Royal Society of Chemistry 2017.

[6] N. Kosinov, C. Liu, E.J.M. Hensen, E.A. Pidko, Engineering of transition metal catalysts confined in zeolites, Chem. Mater. 30 (2018) 3177-3198.

[7] W. Loewenstein, The distribution of aluminum in the tetrahedra of Silicates and aluminates, Am. Miner. 39 (1954) 92-96.

[8] A. Corma, M. Moliner, Á. Cantín, M.J. Díaz-Cabañas, J.L. Jordá, D. Zhang, J. Sun, K. Jansson, S. Hovmöller, X. Zou, Synthesis and structure of polymorph B of zeolite beta, Chem. Mater. 20 (2008) 3218-3223.

[9] C.S. Cundy, P.A. Cox, The hydrothermal synthesis of zeolites: precursors, intermediates and reaction mechanism, Microporous Mesoporous Mater. 82 (2005) 1-78.

[10] S.H. Ahn, S.B. Hong, Transformation control of a layered zeolite precursor by simple cation exchange, Chem. Mater. 32 (2020) 9740-9746.

[11] L.A. Villaescusa, P.S. Wheatley, I. Bull, P. Lightfoot, R.E. Morris, The location and ordering of fluoride ions in pure silica zeolites with framework types IFR and STF; implications for the mechanism of zeolite synthesis in fluoride media, J. Am. Chem. Soc. 123 (2001) 8797-8805.

[12] E.M. Flanigen, R.L. Patton, U.S. Patent 4,073,865, 1978.

[13] P.A. Barrett, M.J. Díaz-Cabañas, M.A. Camblor, R.H. Jones, Synthesis in fluoride and hydroxide media and structure of the extra-large pore pure silica zeolite CIT-5, J. Chem. Soc., Faraday Trans. 94 (1998) 2475-2481.

[14] O. Larlus, V.P. Valtchev, Control of the morphology of all-silica BEA-type zeolite synthesized in basic media, Chem. Mater. 17 (2005) 881-886.

[15] F. Testa, L. Pasqua, F. Crea, R. Aiello, K. Lazar, P. Fejes, P. Lentz, J.B. Nagy, Synthesis of Fe-MFI zeolites in fluoride-containing media, Microporous Mesoporous Mater. 57 (2003) 57-72.

[16] S. Imasaka, H. Ishii, J. Hayashi, S. Araki, H. Yamamoto, Synthesis of CHA-type titanosilicate zeolites using titanium oxide as Ti source and evaluation of their physicochemical properties, Microporous Mesoporous Mater. 273 (2019) 243-248.

[17] R.M. Barrer, P.J. Denny, Hydrothermal chemistry of the silicates. Part IX. nitrogenous aluminosilicates, J. Chem. Soc. (1961) 971-982.

[18] G.T. Kerr, K.G. T., Sodium zeolite ZK-4, a new synthetic crystalline aluminosilicate, J. Am. Chem. Soc. 83 (1961) 4675.

[19] R.L. Wadlinger, G.T. Kerr, E.J. Rosinski, U.S. Patent 3,308,069, 1967.

[20] R.J. Argauer, G.R. Landolt, U.S. Patent 3,702,886, 1972.

[21] L. Gómez-Hortigüela Sainz, Insights into the chemistry of organic structure-directing agents in the synthesis of zeolitic materials, Springer, Cham 2018.

[22] J. Čejka, J. Peréz-Pariente, W.J. Roth, Zeolites: from model materials to industrial catalysts, Transworld Research Network 2008.

[23] M. Miyamoto, T. Nakatani, Y. Fujioka, K. Yogo, Verified synthesis of pure silica CHA-type zeolite in fluoride media, Microporous Mesoporous Mater. 206 (2015) 67-74.

[24] A.E. Nielsen, Transport control in crystal growth from solution, Croat. Chem. Acta 53 (1980) 255-279.

[25] L. Ding, Y. Zheng, Z. Zhang, Z. Ring, J. Chen, Effect of agitation on the synthesis of zeolite beta and its synthesis mechanism in absence of alkali cations, Microporous Mesoporous Mater. 94 (2006) 1-8.

[26] N. Hanif, M.W. Anderson, V. Alfredsson, O. Terasaki, The effect of stirring on the synthesis of intergrowths of zeolite Y polymorphs, Phys. Chem. Chem. Phys. 2 (2000) 3349-3357.

[27] W. Xu, J. Dong, J. Li, J. Li, F. Wu, A novel method for the preparation of zeolite ZSM-5, J. Chem. Soc., Chem. Commun. (1990) 755-756.

[28] L. Ren, Q. Wu, C. Yang, L. Zhu, C. Li, P. Zhang, H. Zhang, X. Meng, F.-S. Xiao, Solvent-free synthesis of zeolites from solid raw materials, J. Am. Chem. Soc. 134 (2012) 15173-15176.

[29] Y. Jin, Q. Sun, G. Qi, C. Yang, J. Xu, F. Chen, X. Meng, F. Deng, F.-S. Xiao, Solvent-free synthesis of silicoaluminophosphate zeolites, Angew. Chem. Int. Ed. 52 (2013) 9172-9175.

[30] T. Pan, Z. Wu, A. Yip, Advances in the green synthesis of microporous and hierarchical zeolites: a short review, Catalysts 9 (2019) 274.

[31] Y.Q. Wang, Q. Wu, X. Meng, F.-S. Xiao, Insights into the organotemplate-free synthesis of zeolite catalysts, Engineering 3 (2017) 567-574.

[32] Q. Wu, X. Wang, G. Qi, Q. Guo, S. Pan, X. Meng, J. Xu, F. Deng, F. Fan, Z. Feng, C. Li, S. Maurer, U. Muller, F.-S. Xiao, Sustainable synthesis of zeolites without addition of both organotemplates and solvents, J. Am. Chem. Soc. 136 (2014) 4019-4025.

[33] C.S. Cundy, Microwave techniques in the synthesis and modification of zeolite catalysts. A review, Collect. Czech. Chem. Commun. 63 (1998) 1699-1723.

[34] G. Feng, P. Cheng, W. Yan, M. Boronat, X. Li, J. Su, J. Wang, Y. Li, A. Corma, R. Xu, J. Yu, Accelerated crystallization of zeolites via hydroxyl free radicals, Science 351 (2016) 1188-1191.

[35] Z. Liu, T. Wakihara, D. Nishioka, K. Oshima, T. Takewaki, T. Okubo, One-minute synthesis of crystalline microporous aluminophosphate (AlPO4-5) by combining fast heating with a seed-assisted method, Chem. Commun. 50 (2014) 2526-2528.

[36] Z. Liu, T. Wakihara, D. Nishioka, K. Oshima, T. Takewaki, T. Okubo, Ultrafast continuous-flow synthesis of crystalline microporous aluminophosphate AlPO4-5, Chem. Mater. 26 (2014) 2327-2331.

[37] Z. Liu, T. Wakihara, K. Oshima, D. Nishioka, Y. Hotta, S.P. Elangovan, Y. Yanaba, T. Yoshikawa, W. Chaikittisilp, T. Matsuo, T. Takewaki, T. Okubo, Widening synthesis bottlenecks: realization of ultrafast and continuous-flow synthesis of high-silica zeolite SSZ-13 for NOx removal, Angew. Chem. Int. Ed. 54 (2015) 5683-5687.

[38] Z. Liu, J. Zhu, T. Wakihara, T. Okubo, Ultrafast synthesis of zeolites: breakthrough, progress and perspective, Inorg. Chem. Front. 6 (2019) 14-31.

[39] K. Iyoki, K. Itabashi, T. Okubo, Progress in seed-assisted synthesis of zeolites without using organic structure-directing agents, Microporous Mesoporous Mater. 189 (2014) 22-30.

[40] N. Ren, Z.-J. Yang, X.-C. Lv, J. Shi, Y.-H. Zhang, Y. Tang, A seed surface crystallization approach for rapid synthesis of submicron ZSM-5 zeolite with controllable crystal size and morphology, Microporous Mesoporous Mater. 131 (2010) 103-114.

[41] R. Jain, J.D. Rimer, Seed-Assisted zeolite synthesis: the impact of seeding conditions and interzeolite transformations on crystal structure and morphology, Microporous Mesoporous Mater. 300 (2020) 110174.

[42] G. Chen, Q. Sun, J. Yu, Nanoseed-assisted synthesis of nano-sized SAPO-34 zeolites using morpholine as the sole template with superior MTO performance, Chem. Commun. 53 (2017) 13328-13331.

[43] G. Majano, A. Darwiche, S. Mintova, V. Valtchev, Seed-induced crystallization of nanosized Na-ZSM-5 crystals, Ind. Eng. Chem. Res. 48 (2009) 7084-7091.

[44] G. Majano, L. Delmotte, V. Valtchev, S. Mintova, Al-rich zeolite beta by seeding in the absence of organic template, Chem. Mater. 21 (2009) 4184-4191.

[45] B. Xie, H. Zhang, C. Yang, S. Liu, L. Ren, L. Zhang, X. Meng, B. Yilmaz, U. Muller, F.-S. Xiao, Seed-directed synthesis of zeolites with enhanced performance in the absence of organic templates, Chem. Commun. 47 (2011) 3945-3947.

[46] P. Wu, M. Yang, L. Sun, S. Zeng, S. Xu, P. Tian, Z. Liu, Synthesis of nanosized SAPO-34 with the assistance of bifunctional amine and seeds, Chem. Commun. 54 (2018) 11160-11163.

[47] Y. Kamimura, S. Tanahashi, K. Itabashi, A. Sugawara, T. Wakihara, A. Shimojima, T. Okubo, Crystallization behavior of zeolite beta in OSDA-free, seed-assisted synthesis, J. Phys. Chem. C 115 (2011) 744-750.

[48] G.T.M. Kadja, I.R. Kadir, A.T.N. Fajar, V. Suendo, R.R. Mukti, Revisiting the seed-assisted synthesis of zeolites without organic structure-directing agents: insights from the CHA case, RSC Adv. 10 (2020) 5304-5315.

[49] Y. Wang, X. Wang, Q. Wu, X. Meng, Y. Jin, X. Zhou, F.-S. Xiao, Seed-directed and organotemplate-free synthesis of TON zeolite, Catal. Today 226 (2014) 103-108.

[50] H. Jon, N. Ikawa, Y. Oumi, T. Sano, An insight into the process involved in hydrothermal conversion of FAU to *BEA zeolite, Chem. Mater. 20 (2008) 4135-4141.

[51] C.-T. Chen, K. Iyoki, H. Yamada, S. Sukenaga, M. Ando, H. Shibata, K. Ohara, T. Wakihara, T. Okubo, Zeolite crystallization triggered by intermediate stirring, J. Phys. Chem. C 123 (2019) 20304-20313.

[52] R. Li, A. Chawla, N. Linares, J.G. Sutjianto, K.W. Chapman, J.G. Martínez, J.D. Rimer, Diverse physical states of amorphous precursors in zeolite synthesis, Ind. Eng. Chem. Res. 57 (2018) 8460-8471.

[53] M. Shamzhy, M. Opanasenko, P. Concepcion, A. Martinez, New trends in tailoring active sites in zeolite-based catalysts, Chem. Soc. Rev. 48 (2019) 1095-1149.

[54] M. Houlleberghs, E. Breynaert, K. Asselman, E. Vaneeckhaute, S. Radhakrishnan, M.W. Anderson, F. Taulelle, M. Haouas, J.A. Martens, C.E.A. Kirschhock, Evolution of the crystal growth mechanism of zeolite W (MER) with temperature, Microporous Mesoporous Mater. 274 (2019) 379-384.

[55] J. Grand, H. Awala, S. Mintova, Mechanism of zeolites crystal growth: new findings and open questions, CrystEngComm 18 (2016) 650-664.

[56] X. Chen, M. Qiao, S. Xie, K. Fan, W. Zhou, H. He, Self-construction of core-shell and hollow zeolite analcime icositetrahedra: a reversed crystal growth process via oriented aggregation of nanocrystallites and recrystallization from surface to core, J. Am. Chem. Soc. 129 (2007) 13305-13312.

[57] F. Hasan, R. Singh, P.A. Webley, Formation of LTA zeolite crystals with multi-hollow polycrystalline core-shell structure via aggregation-recrystallization route in presence of emulsion droplets, Microporous Mesoporous Mater. 160 (2012) 75-84.

[58] Q. Wang, G. Chen, S. Xu, Hierarchical architecture observed in microspheres comprising microporous $AlPO_4$-11 nanocrystals, Microporous Mesoporous Mater. 119 (2009) 315-321.

[59] X. Yang, J. Fu, C. Jin, J. Chen, C. Liang, M. Wu, W. Zhou, Formation mechanism of $CaTiO_3$ hollow crystals with different microstructures, J. Am. Chem. Soc. 132 (2010) 14279-14287.

[60] M.L. Moreira, J. Andrés, V.R. Mastelaro, J.A. Varela, E. Longo, On the reversed crystal growth of $BaZrO_3$ decaoctahedron: shape evolution and mechanism, CrystEngComm 13 (2011) 5818-5824.

[61] K. Self, H. Zhou, H.F. Greer, Z.R. Tian, W. Zhou, Reversed crystal growth of ZnO microdisks, Chem. Commun. 49 (2013) 5411-5413.

[62] J. Chen, S. Macfarlane, C. Zhang, K. Yu, W. Zhou, Chemistry of Hydrolysis of $FeCl_3$ in the Presence of Phosphate to Form Hematite Nanotubes and Nanorings, Cryst. Growth Des. 17 (2017) 5975-5983.

[63] C. Zheng, H.F. Greer, C.-Y. Chiang, W. Zhou, Microstructural study of the formation mechanism of metal–organic framework MOF-5, CrystEngComm 16 (2014) 1064-1070.

[64] K. Self, M. Telfer, H.F. Greer, W. Zhou, Reversed crystal growth of RHO zeolitic imidazolate framework (ZIF), Chem. Eur. J. 21 (2015) 19090-19095.

[65] W. Zhou, Reversed crystal growth: implications for crystal engineering, Adv. Mater. 22 (2010) 3086-3092.

[66] Y. Wang, X. Li, Z. Xue, L. Dai, S. Xie, Q. Li, Preparation of zeolite ANA crystal from zeolite Y by in situ solid phase iso-structure transformation, J. Phys. Chem. B 114 (2010) 5747-5754.

[67] W. Zhou, Reversed crystal growth, Crystals 9 (2019) 7.

[68] J. Yao, D. Li, X. Zhang, C.H. Kong, W. Yue, W. Zhou, H. Wang, Cubes of zeolite A with an amorphous core, Angew. Chem. Int. Ed. 47 (2008) 8397-8399.

[69] H. Greer, P.S. Wheatley, S.E. Ashbrook, R.E. Morris, W. Zhou, Early stage reversed crystal growth of zeolite A and its phase transformation to sodalite, J. Am. Chem. Soc. 131 (2009) 17986-17992.

[70] Z.D. Wang, Y. Liu, J.-G. Jiang, M. He, P. Wu, Synthesis of ZSM-5 zeolite hollow spheres with a core/shell structure, J. Mater. Chem. 20 (2010) 10193-10199.

[71] A.W. Ritchie, M.I.T. Watson, R. Turnbull, Z. Lu, M. Telfer, J.E. Gano, K. Self, H.F. Greer, W. Zhou, Reversed crystal growth of rhombohedral calcite in the presence of chitosan and gum arabic, CrystEngComm 15 (2013) 10266-10271.

[72] O. Vasylkiv, O. Bezdorozhev, Y. Sakka, Synthesis of iron oxide nanoparticles with different morphologies by precipitation method with and without chitosan addition, J. Ceramic Soc. Jpn. 124 (2016) 489-494.

[73] S.J. Turner, J. Chen, A.M.Z. Slawin, W. Zhou, New mechanism for the nucleation and growth of large zeolite X crystals in the presence of triethanolamine, Chem. Commun. 55 (2019) 862-865.

[74] H.F. Greer, Non-classical crystal growth of inorganic and organic materials, Mater. Sci. Technol. 30 (2014) 611-626.

[75] R.E. Morris, J. Čejka, Exploiting chemically selective weakness in solids as a route to new porous materials, Nat. Chem. 7 (2015) 381-388.

[76] J. Li, A. Corma, J. Yu, Synthesis of new zeolite structures, Chem. Soc. Rev. 44 (2015) 7112-7127.

[77] J. Čejka, R. Millini, M. Opanasenko, D.P. Serrano, W.J. Roth, Advances and challenges in zeolite synthesis and catalysis, Catal. Today 345 (2020) 2-13.

[78] A. Corma, M.T. Navarro, F. Rey, J. Rius, S. Valencia, Pure polymorph C of zeolite beta synthesized by using framework isomorphous substitution as a structure-directing mechanism, Angew. Chem. Int. Ed. 40 (2001) 2277-2280.

[79] X. Liu, U. Ravon, F. Bosselet, G. Bergeret, A. Tuel, Probing Ge distribution in zeolite frameworks by post-synthesis introduction of fluoride in as-made materials, Chem. Mater. 24 (2012) 3016-3022.

[80] T. Blasco, A. Corma, M.J. Díaz-Cabañas, F. Rey, J.A. Vidal-Moya, C.M. Zicovich-Wilson, Preferential location of Ge in the double four-membered ring units of ITQ-7 zeolite, J. Phys. Chem. B 106 (2002) 2634-2642.

[81] A. Corma, M.J. Díaz-Cabañas, J.L. Jordá, C. Martínez, M. Moliner, High-throughput synthesis and catalytic properties of a molecular sieve with 18- and 10-member rings, Nature 443 (2006) 842-845.

[82] J. Jiang, J.L. Jorda, M.J. Diaz‐Cabanas, J. Yu, A. Corma, The synthesis of an extra‐large‐pore zeolite with double three‐ring building units and a Low framework density, Angew. Chem. Int. Ed. 122 (2010) 5106-5108.

[83] W.J. Roth, O.V. Shvets, M. Shamzhy, P. Chlubna, M. Kubu, P. Nachtigall, J. Cejka, Postsynthesis transformation of three-dimensional framework into a lamellar zeolite with modifiable architecture, J. Am. Chem. Soc. 133 (2011) 6130-6133.

[84] J.H. Kang, D. Xie, S.I. Zones, M.E. Davis, Transformation of extra-large pore germanosilicate CIT-13 molecular sieve into extra-large Pore CIT-5 molecular sieve, Chem. Mater. 31 (2019) 9777-9787.

[85] P. Chlubná, W.J. Roth, H.F. Greer, W. Zhou, O. Shvets, A. Zukal, J. Čejka, R.E. Morris, 3D to 2D routes to ultrathin and expanded zeolitic materials, Chem. Mater. 25 (2013) 542-547.

[86] W.J. Roth, P. Nachtigall, R.E. Morris, P.S. Wheatley, V.R. Seymour, S.E. Ashbrook, P. Chlubna, L. Grajciar, M. Polozij, A. Zukal, O. Shvets, J. Cejka, A family of zeolites with controlled pore size prepared using a top-down method, Nat. Chem. 5 (2013) 628-633.

[87] P. Eliasova, M. Opanasenko, P.S. Wheatley, M. Shamzhy, M. Mazur, P. Nachtigall, W.J. Roth, R.E. Morris, J. Čejka, The ADOR mechanism for the synthesis of new zeolites, Chem. Soc. Rev. 44 (2015) 7177-7206.

[88] M. Mazur, P.S. Wheatley, M. Navarro, W.J. Roth, M. Polozij, A. Mayoral, P. Eliasova, P. Nachtigall, J. Čejka, R.E. Morris, Synthesis of 'unfeasible' zeolites, Nat. Chem. 8 (2016) 58-62.

[89] N. Kasian, A. Tuel, E. Verheyen, C.E.A. Kirschhock, F. Taulelle, J.A. Martens, NMR evidence for specific germanium siting in IM-12 zeolite, Chem. Mater. 26 (2014) 5556-5565.

[90] P. Chlubná-Eliášová, Y. Tian, A.B. Pinar, M. Kubů, J. Čejka, R.E. Morris, The assembly-disassembly-organization-reassembly mechanism for 3D-2D-3D transformation of germanosilicate IWW zeolite, Angew. Chem. Int. Ed. 53 (2014) 7048-7052.

[91] M. Shamzhy, M. Opanasenko, Y. Tian, K. Konysheva, O. Shvets, R.E. Morris, J. Čejka, Germanosilicate precursors of ADORable zeolites obtained by disassembly of ITH, ITR, and IWR zeolites, Chem. Mater. 26 (2014) 5789-5798.

[92] S.E. Henkelis, M. Mazur, C.M. Rice, P.S. Wheatley, S.E. Ashbrook, R.E. Morris, Kinetics and mechanism of the hydrolysis and rearrangement processes within the assembly–disassembly–organization–reassembly synthesis of zeolites, J. Am. Chem. Soc. 141 (2019) 4453-4459.

[93] S.E. Henkelis, M. Mazur, C.M. Rice, G.P.M. Bignami, P.S. Wheatley, S.E. Ashbrook, J. Čejka, R.E. Morris, A procedure for identifying possible products in the assembly–disassembly–organization–reassembly (ADOR) synthesis of zeolites, Nat. Protoc. 14 (2019) 781-794.

[94] J. Zhang, O. Veselý, Z. Tošner, M. Mazur, M. Opanasenko, J. Čejka, M. Shamzhy, Toward controlling disassembly step within the ADOR process for the synthesis of zeolites, Chem. Mater. 33 (2021) 1228-1237.

[95] M. Mazur, A.M. Arévalo-López, P.S. Wheatley, G.P.M. Bignami, S.E. Ashbrook, Á. Morales-García, P. Nachtigall, J.P. Attfield, J. Čejka, R.E. Morris, Pressure-induced chemistry for the 2D to 3D transformation of zeolites, J. Mater. Chem. A (2018).

[96] M. Trachta, P. Nachtigall, O. Bludský, The ADOR synthesis of new zeolites: In silico investigation, Catal. Today 243 (2015) 32-38.

[97] E. Verheyen, L. Joos, K. Van Havenbergh, E. Breynaert, N. Kasian, E. Gobechiya, K. Houthoofd, C. Martineau, M. Hinterstein, F. Taulelle, V. Van Speybroeck, M. Waroquier, S. Bals, G. Van Tendeloo, C.E. Kirschhock, J.A. Martens, Design of zeolite by inverse sigma transformation, Nat. Mater. 11 (2012) 1059-1064.

[98] S.A. Morris, G.P.M. Bignami, Y. Tian, M. Navarro, D.S. Firth, J. Cejka, P.S. Wheatley, D.M. Dawson, W.A. Slawinski, D.S. Wragg, R.E. Morris, S.E. Ashbrook, In situ solid-state NMR and XRD studies of the ADOR process and the unusual structure of zeolite IPC-6, Nat. Chem. 9 (2017) 1012-1018.

[99] P.S. Wheatley, P. Chlubna-Eliasova, H. Greer, W. Zhou, V.R. Seymour, D.M. Dawson, S.E. Ashbrook, A.B. Pinar, L.B. McCusker, M. Opanasenko, J. Čejka, R.E. Morris, Zeolites with continuously tuneable porosity, Angew. Chem. Int. Ed. 53 (2014) 13210-13214.

[100] V. Kasneryk, M. Shamzhy, M. Opanasenko, P.S. Wheatley, S.A. Morris, S.E. Russell, A. Mayoral, M. Trachta, J. Cejka, R.E. Morris, Expansion of the ADOR strategy for the synthesis of zeolites: the synthesis of IPC-12 from zeolite UOV, Angew. Chem. Int. Ed. 56 (2017) 4324-4327.

[101] V. Kasneryk, M. Shamzhy, M. Opanasenko, P.S. Wheatley, R.E. Morris, J. Cejka, Insight into the ADOR zeolite-to-zeolite transformation: the UOV case, Dalton Trans. 47 (2018) 3084-3092.

[102] D.S. Firth, S.A. Morris, P.S. Wheatley, S.E. Russell, A.M.Z. Slawin, D.M. Dawson, A. Mayoral, M. Opanasenko, M. Polozij, J. Cejka, P. Nachtigall, R.E. Morris, Assembly-disassembly-organization-reassembly synthesis of zeolites based on *cfi*-type layers, Chem. Mater. 29 (2017) 5605-5611.

[103] C.J. Heard, J. Čejka, M. Opanasenko, P. Nachtigall, G. Centi, S. Perathoner, 2D oxide nanomaterials to address the energy transition and catalysis, Adv. Mater. 31 (2019) 1801712.

[104] C.J. Heard, L. Grajciar, F. Uhlík, M. Shamzhy, M. Opanasenko, J. Čejka, P. Nachtigall, Zeolite (In)stability under aqueous or steaming conditions, Adv. Mater. 32 (2020) 2003264.

[105] M. Opanasenko, M. Shamzhy, Y. Wang, W. Yan, P. Nachtigall, J. Čejka, Synthesis and post-synthesis transformation of germanosilicate zeolites, Angew. Chem. Int. Ed. 59 (2020) 19380-19389.

[106] R. Castaneda, A. Corma, V. Fornes, F. Rey, J. Rius, Synthesis of a new zeolite structure ITQ-24, with intersecting 10- and 12-membered ring pores, J. Am. Chem. Soc. 125 (2003) 7820-7821.

[107] A. Corma, F. Rey, S. Valencia, J.L. Jorda, J. Rius, A zeolite with interconnected 8-, 10- and 12-ring pores and its unique catalytic selectivity, Nat. Mater. 2 (2003) 493-497.

[108] A. Corma, M. Puche, F. Rey, G. Sankar, S.J. Teat, A zeolite structure (ITQ-13) with three sets of medium-pore crossing channels formed by 9- and 10-rings, Angew. Chem. Int. Ed. 42 (2003) 1156-1159.

[109] A. Corma, M.J. Diaz-Cabanas, J.L. Jorda, F. Rey, G. Sastre, K.G. Strohmaier, A zeolitic structure (ITQ-34) with connected 9- and 10-ring channels obtained with phosphonium cations as structure directing agents, J. Am. Chem. Soc. 130 (2008) 16482-16483.

[110] D.L. Dorset, G.J. Kennedy, K.G. Strohmaier, M.J. Diaz-Cabanas, F. Rey, A. Corma, P-derived organic cations as structure-directing agents: synthesis of a high-silica zeolite (ITQ-27) with a two-dimensional 12-ring channel system, J. Am. Chem. Soc. 128 (2006) 8862-8867.

[111] Y. Luo, S. Smeets, Z. Wang, J. Sun, W. Yang, Synthesis and structure determination of SCM-15: a 3D large pore zeolite with interconnected straight 12x12x10-ring channels, Chem. Eur. J. 25 (2019) 2184-2188.

[112] W. Hua, H. Chen, Z.B. Yu, X. Zou, J. Lin, J. Sun, A germanosilicate structure with 11x11x12-ring channels solved by electron crystallography, Angew. Chem. Int. Ed. 53 (2014) 5868-5871.

[113] M. Dodin, J.L. Paillaud, Y. Lorgouilloux, P. Caullet, E. Elkaim, N. Bats, A zeolitic material with a three-dimensional pore system formed by straight 12- and 10-ring channels synthesized with an imidazolium derivative as structure-directing agent, J. Am. Chem. Soc. 132 (2010) 10221-10223.

[114] D.L. Dorset, K.G. Strohmaier, C.E. Kliewer, A. Corma, M.J. Diaz-Cabanas, F. Rey, C.J. Gilmore, Crystal structure of ITQ-26, a 3D framework with extra-large pores, Chem. Mater. 20 (2008) 5325-5331.

[115] S.I. Zones, S.-J. Hwang, A novel approach to borosilicate zeolite synthesis in the presence of fluoride, Microporous Mesoporous Mater. 146 (2011) 48-56.

[116] X. Liu, J. Klinowski, Gallosilicate zeolite catalysts: structural features of [Si,Ga]-ZSM-5, J. Phys. Chem. 96 (1992) 3403-3408.

[117] M. Taramasso, G. Perego, B. Notari, U.S. Patent 4410501, 1983, (1996).

[118] G. Li, L. Gao, Z.Z. Sheng, Y.L. Zhan, C.Y. Zhang, J. Ju, Y.H. Zhang, Y. Tang, A Zr-Al-Beta zeolite with open Zr(iv) sites: an efficient bifunctional Lewis-Bronsted acid catalyst for a cascade reaction, Catal. Sci. Technol. 9 (2019) 4055-4065.

[119] Z. Zhu, H. Xu, J. Jiang, Y. Guan, P. Wu, Sn-Beta zeolite hydrothermally synthesized via interzeolite transformation as efficient Lewis acid catalyst, J. Catal. 352 (2017) 1-12.

[120] S. De, S. Duttab, B. Saha, Critical design of heterogeneous catalysts for biomass valorization: current thrust and emerging prospects, Catal. Sci. Technol. 6 (2016) 7364-7385.

[121] C.N. Soekiman, K. Miyake, Y. Hayashi, Y. Zhu, M. Ota, H. Al-Jabri, R. Inoue, Y. Hirota, Y. Uchida, S. Tanaka, C.Y. Kong, N. Nishiyama, Synthesis of titanium silicalite-1 (TS-1) zeolite with high content of Ti by a dry gel conversion method using amorphous $TiO_2$–$SiO_2$ composite with highly dispersed Ti species, Mater. Today Chem. 16 (2020) 100209.

[122] P. Ratnasamy, R. Kumar, Transition metal-silicate analogs of zeolites, Catal. Lett. 22 (1993) 227-237.

[123] P.S. Niphadkar, N.P. Tangale, P.N. Joshi, S.V. Awate, Crystallization kinetics of Sn-MFI molecular sieve formation by dry gel Cross Mark conversion method, Microporous Mesoporous Mater. 182 (2013) 73-80.

[124] W. Dai, Q. Lei, G. Wu, N. Guan, M. Hunger, L. Li, Spectroscopic signature of lewis acidic framework and extraframework Sn sites in beta zeolites, ACS Catal. 10 (2020) 14135-14146.

[125] P. Li, G. Liu, H. Wu, Y. Liu, J.-G. Jiang, P. Wu, Postsynthesis and selective oxidation properties of nanosized Sn-beta zeolite, J. Phys. Chem. C 115 (2011) 3663-3670.

[126] J. Zhang, Q.D. Yue, M. Mazur, M. Opanasenko, M.V. Shamzhy, J. Čejka, Selective recovery and recycling of germanium for the design of sustainable zeolite catalysts, ACS Sustainable Chem. Eng. 8 (2020) 8235-8246.

[127] X. Cao, D. Guo, W. Sun, P. Zhang, G. Ding, J. Bian, Supersonic separation technology for carbon dioxide and hydrogen sulfide removal from natural gas, J. Cleaner Prod. 288 (2021) 125689.

[128] R.L. Siegelman, P.J. Milner, E.J. Kim, S.C. Weston, J.R. Long, Challenges and opportunities for adsorption-based $CO_2$ capture from natural gas combined cycle emissions, Energy Environ. Sci. 12 (2019) 2161-2173.

[129] Y. Li, H. Yi, X. Tang, F. Li, Q. Yuan, Adsorption separation of $CO_2/CH_4$ gas mixture on the commercial zeolites at atmospheric pressure, Chem. Eng. J. 229 (2013) 50-56.

[130] O. Cheung, N. Hedin, Zeolites and related sorbents with narrow pores for $CO_2$ separation from flue gas, RSC Adv. 4 (2014) 14480-14494.

[131] M. Moliner, C. Martinez, A. Corma, Synthesis strategies for preparing useful small pore zeolites and zeotypes for gas separations and catalysis, Chem. Mater. 26 (2014) 246-258.

[132] P. Rzepka, Z. Bacsik, A.J. Pell, N. Hedin, A. Jaworski, Nature of chemisorbed $CO_2$ in zeolite A, J. Phys. Chem. C 123 (2019) 21497-21503.

[133] X. Cui, K. Chen, H. Xing, Q. Yang, R. Krishna, Z. Bao, H. Wu, W. Zhou, X. Dong, Y. Han, B. Li, Q. Ren, M.J. Zaworotko, B. Chen, Pore chemistry and size control in hybrid porous materials for acetylene capture from ethylene, Science 353 (2016) 141-144.

[134] L. Li, R. Lin, R. Krishna, H. Li, S. Xiang, H. Wu, J. Li, W. Zhou, B. Chen, Ethane/ethylene separation in a metal-organic framework with iron-peroxo sites, Science 362 (2018) 443-446.

[135] M. Lee, S. Hong, D. Kim, E. Kim, K. Lim, J.C. Jung, H. Richter, J.-H. Moon, N. Choi, J. Nam, J. Choi, Chabazite-type zeolite membranes for effective $CO_2$ separation: the role of hydrophobicity and defect structure, ACS Appl. Mater. Interfaces 11 (2019) 3946-3960.

[136] N. Kosinov, C. Auffret, C. Gucuyener, B.M. Szyja, J. Gascon, F. Kapteijn, E.J.M. Hensen, High flux high-silica SSZ-13 membrane for $CO_2$ separation, J. Mater. Chem. A 2 (2014) 13083-13092.

[137] T.-H. Bae, M.R. Hudson, J.A. Mason, W.L. Queen, J.J. Dutton, K. Sumida, K.J. Micklash, S.S. Kaye, C.M. Brown, J.R. Long, Evaluation of cation-exchanged zeolite adsorbents for post-combustion carbon dioxide capture, Energy Environ. Sci. 6 (2013) 128-138.

[138] A. Zukal, A. Pulido, B. Gil, P. Nachtigall, O. Bludský, M. Rubeš, J. Čejka, Experimental and theoretical determination of adsorption heats of $CO_2$ over alkali metal exchanged ferrierites with different Si/Al ratio, Phys. Chem. Chem. Phys. 12 (2010) 6413-6422.

[139] P.J. Bereciartua, A. Cantin, A. Corma, J.L. Jorda, M. Palomino, F. Rey, S. Valencia, E.W. Corcoran, Jr., P. Kortunov, P.I. Ravikovitch, A. Burton, C. Yoon, Y. Wang, C. Paur, J. Guzman, A.R. Bishop, G.L. Casty, Control of zeolite framework flexibility and pore topology for separation of ethane and ethylene, Science 358 (2017) 1068-1071.

[140] S.M. Kuznicki, V.A. Bell, S. Nair, H.W. Hillhouse, R.M. Jacubinas, C.M. Braunbarth, B.H. Toby, M. Tsapatsis, A titanosilicate molecular sieve with adjustable pores for size-selective adsorption of molecules, Nature 412 (2001) 720-724.

[141] J.B. Parise, L. Abrams, T.E. Gier, D.R. Corbin, J.D. Jorgensen, E. Prince, Flexibility of the framework of zeolite Rho - structural variation from 11 to 573-K - a study using neutron powder diffraction data, J. Phys. Chem. 88 (1984) 2303-2307.

[142] F.N. Ridha, P.A. Webley, Anomalous Henry's law behavior of nitrogen and carbon dioxide adsorption on alkali-exchanged chabazite zeolites, Sep. Purif. Technol. 67 (2009) 336-343.

[143] J. Shang, G. Li, R. Singh, Q. Gu, K.M. Nairn, T.J. Bastow, N. Medhekar, C.M. Doherty, A.J. Hill, J.Z. Liu, P.A. Webley, Discriminative separation of gases by a "molecular trapdoor" mechanism in chabazite zeolites, J. Am. Chem. Soc. 134 (2012) 19246-19253.

[144] V.M. Georgieva, E.L. Bruce, M.C. Verbraeken, A.R. Scott, W.J. Casteel, Jr., S. Brandani, P.A. Wright, Triggered gate opening and breathing effects during selective $CO_2$ adsorption by merlinoite zeolite, J. Am. Chem. Soc. 141 (2019) 12744-12759.

[145] J. Čejka, H. Van Bekkum, A. Corma, F. Schueth, Introduction to zeolite molecular sieves, 3rd edition, Elsevier 2007.

[146] Y. Nakazaki, Y. Tanaka, N. Goto, T. Inui, Mechanisms of $CO_2$ separation by microporous crystals estimated by computational chemistry, Catal.Today 23 (1995) 391-396.

[147] M.R. Hudson, W.L. Queen, J.A. Mason, D.W. Fickel, R.F. Lobo, C.M. Brown, Unconventional, highly selective CO2 adsorption in zeolite SSZ-13, J. Am. Chem. Soc. 134 (2012) 1970-1973.

[148] Y. Yu, X. Li, R. Krishna, Y. Liu, Y. Cui, J. Du, Z. Liang, X. Song, J. Yu, Enhancing $CO_2$ adsorption and separation properties of aluminophosphate zeolites by isomorphous heteroatom substitutions, ACS Appl. Mater. Interfaces 10 (2018) 43570-43577.

[149] P. Caullet, J.L. Guth, J. Hazm, J.M. Lamblin, H. Gies, ChemInform abstract: synthesis, characterization, and crystal structure of the new clathrasil phase octadecasil, ChemInform 22 (1991).

[150] J. Michael Bennett, R.M. Kirchner, The structure of as-synthesized $AlPO_4$-16 determined by a new framework modeling method and Rietveld refinement of synchrotron powder diffraction data, Zeolites 11 (1991) 502-506.

[151] H. Li, O.M. Yaghi, Transformation of germanium dioxide to microporous germanate 4-connected nets, J. Am. Chem. Soc. 120 (1998) 10569-10570.

[152] Y. Wang, J. Song, H. Gies, The substitution of germanium for silicon in AST-type zeolite, Solid State Sci. 5 (2003) 1421-1433.

[153] C.A. Fyfe, A.R. Lewis, J.M. Chézeau, H. Grondey, $^{19}F/^{29}Si$ distance determinations in fluoride-containing octadecasil from solid-state NMR measurements, J. Am. Chem. Soc. 119 (1997) 12210-12222.

[154] M.W. Sun, H.K. Hunt, C.M. Lew, R. Cai, Y. Liu, Y. Yan, A Dynamic Organic Structuring-Directing Agent for Pure-Silica-Zeolite AST and LTA Syntheses, Chin. J. Catal. 33 (2012) 85-91.

[155] L.A. Villaescusa, P.A. Barrett, M.A. Camblor, Calcination of octadecasil: Fluoride removal and symmetry of the pure SiO2 host, Chem. Mater. 10 (1998) 3966-3973.

[156] L.A. Villaescusa, M.A. Camblor, Time evolution of an aluminogermanate zeolite synthesis: segregation of two closely similar phases with the same structure type, Chem. Mater. 28 (2016) 3090-3098.

[157] L.A. Villaescusa, P.A. Barrett, M.A. Camblor, Calcination of octadecasil: fluoride removal and symmetry of the pure $SiO_2$ host, Chem. Mater. 10 (1998) 3966-3973.

[158] E. Dib, M. Freire, V. Pralong, T. Mineva, B. Alonso, Intermolecular interactions in AST zeolites through $^{14}N$ NMR and DFT calculations, Acta Crystallogr., Sect. C: Struct. Chem. 73 (2017) 202-207.

[159] M. Sun, R. Cai, Y. Liu, Y. Yan, A dynamic organic structuring-directing agent for pure-silica-zeolite AST and LTA syntheses, Chin. J. Catal. 33 (2012) 85-91.

[160] J. Zhou, F. Gao, K. Sun, X. Jin, Y. Zhang, B. Liu, R. Zhou, Green synthesis of highly $CO_2$-selective CHA zeolite membranes in all-silica and fluoride-free solution for $CO_2/CH_4$ separations, Energy Fuels 34 (2020) 11307-11314.

[161] M. Debost, P.B. Klar, N. Barrier, E.B. Clatworthy, J. Grand, F. Laine, P. Brazda, L. Palatinus, N. Nesterenko, P. Boullay, S. Mintova, Synthesis of discrete CHA zeolite nanocrystals without organic templates for selective $CO_2$ capture, Angew. Chem. Int. Ed. 59 (2020) 23491-23495.

[162] K.A. Lomachenko, E. Borfecchia, C. Negri, G. Berlier, C. Lamberti, P. Beato, H. Falsig, S. Bordiga, The Cu-CHA deNOx catalyst in action: temperature-dependent $NH_3$-assisted selective catalytic reduction monitored by operando XAS and XES, J. Am. Chem. Soc. 138 (2016) 12025-12028.

[163] G. Yang, J. Han, Y. Huang, X. Chen, V. Valtchev, Busting the efficiency of SAPO-34 catalysts for the methanol-to-olefin conversion by post-synthesis methods, Chin. J. Chem. Eng. 28 (2020) 2022-2027.

[164] C.J. Heard, L. Grajciar, C.M. Rice, S.M. Pugh, P. Nachtigall, S.E. Ashbrook, R.E. Morris, Fast room temperature lability of aluminosilicate zeolites, Nat. Commun. 10 (2019) 4690.

[165] L.X. Tang, K.G. Haw, Y.Y. Zhang, Q.R. Fang, S.L. Qiu, V. Valtchev, Fast and efficient synthesis of SSZ-13 by interzeolite conversion of Zeolite Beta and Zeolite L, Microporous Mesoporous Mater. 280 (2019) 306-314.

[166] H.L. Geng, G. Li, D. Liu, C.Y. Liu, Rapid and efficient synthesis of CHA-type zeolite by interzeolite conversion of LTA-type zeolite in the presence of N, N, N-trimethyladamantammonium hydroxide, J. Solid State Chem. 265 (2018) 193-199.

[167] K. Muraoka, Y. Sada, A. Shimojima, W. Chaikittisilp, T. Okubo, Tracking the rearrangement of atomic configurations during the conversion of FAU zeolite to CHA zeolite, Chem. Sci. 10 (2019) 8533-8540.

[168] N.A. Khan, D.K. Yoo, B.N. Bhadra, J.W. Jun, T.W. Kim, C.-U. Kim, S.H. Jhung, Preparation of SSZ-13 zeolites from beta zeolite and their application in the conversion of ethylene to propylene, Chem. Eng. J. 377 (2019) 119546.

[169] B.N. Bhadra, P.W. Seo, N.A. Khan, J.W. Jun, T.W. Kim, C.U. Kim, S.H. Jhung, Conversion of Y into SSZ-13 zeolite in the presence of tetraethylammonium hydroxide and ethylene-to-propylene reactions over SSZ-13 zeolites, Catal. Today 298 (2017) 53-60.

[170] M. Sarker, N.A. Khan, D.K. Yoo, B.N. Bhadra, J.W. Jun, T.W. Kim, C.-U. Kim, S.H. Jhung, Synthesis of SSZ-13 zeolite in the presence of dimethylethylcyclohexyl ammonium ion and direct conversion of ethylene to propylene with the SSZ-13, Chem. Eng. J. 377 (2019) 120116.

[171] H. Imai, N. Hayashida, T. Yokoi, T. Tatsumi, Direct crystallization of CHA-type zeolite from amorphous aluminosilicate gel by seed-assisted method in the absence of organic-structure-directing agents, Microporous Mesoporous Mater. 196 (2014) 341-348.

[172] G. Sastre, A. Pulido, R. Castaneda, A. Corma, Effect of the germanium incorporation in the synthesis of EU-1, ITQ-13, ITQ-22, and ITQ-24 zeolites, J. Phys. Chem. B 108 (2004) 8830-8835.

[173] R.T. Yuan, N. Claes, E. Verheyen, A. Tuel, S. Bals, E. Breynaert, J.A. Martens, C.E.A. Kirschhock, Synthesis of an IWW-type germanosilicate zeolite using 5-azonia-spiro[4,4] nonane as a structure directing agent, New J. Chem. 40 (2016) 4319-4324.

[174] K. Lu, J. Huang, M. Jiao, Y. Zhao, Y. Ma, J. Jiang, H. Xu, Y. Ma, P. Wu, Topotactic conversion of Ge-rich IWW zeolite into IPC-18 under mild condition, Microporous Mesoporous Mater. 310 (2021) 110617.

[175] X. Hong, W. Chen, G. Zhang, Q. Wu, C. Lei, Q. Zhu, X. Meng, S. Han, A. Zheng, Y. Ma, A.N. Parvulescu, U. Muller, W. Zhang, T. Yokoi, X. Bao, B. Marler, D.E. De Vos, U. Kolb, F.-S. Xiao, Direct synthesis of aluminosilicate IWR zeolite from a strong interaction between zeolite framework and organic template, J. Am. Chem. Soc. 141 (2019) 18318-18324.

[176] A. Cantín, A. Corma, M.J. Diaz-Cabanas, J.L. Jordá, M. Moliner, Rational Design and HT Techniques Allow the Synthesis of New IWR Zeolite Polymorphs, J. Am. Chem. Soc. 128 (2006) 4216-4217.

[177] A.B. Pinar, L.B. McCusker, C. Baerlocher, J. Schmidt, S.-J. Hwang, M.E. Davis, S.I. Zones, Location of Ge and extra-framework species in the zeolite ITQ-24, Dalton Trans. 44 (2015) 6288-6295.

[178] H. Xu, J.-G. Jiang, B. Yang, L. Zhang, M. He, P. Wu, Post-synthesis treatment gives highly stable siliceous zeolites through the isomorphous substitution of silicon for germanium in germanosilicates, Angew. Chem. Int. Ed. 53 (2014) 1355-1359.

[179] M.-J. Díaz-Cabañas, P.A. Barrett, Synthesis and structure of pure $SiO_2$ chabazite: the $SiO_2$ polymorph with the lowest framework density, Chem. Commun. (1998) 1881-1882.

[180] O.V. Shvets, M.V. Shamzhy, P.S. Yaremov, Z. Musilová, D. Procházková, J. Čejka, Isomorphous introduction of boron in germanosilicate zeolites with UTL topology, Chem. Mater. 23 (2011) 2573-2585.

[181] M.V. Shamzhy, O.V. Shvets, M.V. Opanasenko, P.S. Yaremov, L.G. Sarkisyan, P. Chlubná, A. Zukal, V.R. Marthala, M. Hartmann, J. Čejka, Synthesis of isomorphously substituted extra-large pore UTL zeolites, J. Mater. Chem. 22 (2012) 15793-15803.

[182] L. Zhang, Y. Chen, J.-G. Jiang, L. Xu, W. Guo, H. Xu, X.-D. Wen, P. Wu, Facile synthesis of ECNU-20 (IWR) hollow sphere zeolite composed of aggregated nanosheets, Dalton Trans. 46 (2017) 15641-15645.

[183] F. Zernike, How I discovered phase contrast, Science 121 (1955) 345-349.

[184] V. Petříček, M. Dušek, L. Palatinus, Crystallographic computing system JANA2006: general features, Z. Kristallogr. 229 (2014) 345-352.

[185] A.L. Myers, J.M. Prausnitz, Thermodynamics of mixed-gas adsorption, AIChE J. 11 (1965) 121-127.

[186] E. Zschech, M. Löffler, P. Krüger, J. Gluch, K. Kutukova, I. Zgłobicka, J. Silomon, R. Rosenkranz, Y. Standke, E. Topal, Laboratory computed X-ray tomography–a nondestructive technique for 3D microstructure analyis of materials, Pract. Metallogr. 55 (2018) 539-555.

[187] G. Sastre, A. Pulido, A. Corma, Pentacoordinated germanium in AST zeolite synthesised in fluoride media. A $^{19}F$ NMR validated computational study, Chem. Commun. (2005) 2357-2359.

[188] X. Yang, Synthesis and crystal structure of tetramethylammonium fluoride octadecasil, Mater. Res. Bull. 41 (2006) 54-66.

[189] X. Liu, W. Mao, J. Jiang, X. Lu, M. Peng, H. Xu, L. Han, S.-a. Che, P. Wu, Topotactic conversion of alkali-treated Intergrown germanosilicate CIT-13 into single-crystalline ECNU-21 zeolite as shape-selective catalyst for ethylene oxide hydration, Chem. Eur. J. 25 (2019) 4520-4529.

[190] J. Zhang, Q. Yue, M. Mazur, M. Opanasenko, M.V. Shamzhy, J. Cejka, Selective recovery and recycling of germanium for the design of sustainable zeolite catalysts, ACS Sustainable Chem. Eng. 8 (2020) 8235-8246.

[191] J.L. Jordá, A. Cantín, A. Corma, M.J. Diaz-Cabañas, S. Leiva, M. Moliner, F. Rey, M.J. Sabater, S. Valencia, Structural study of pure silica and Gecontaining zeolite ITQ-24, Z. Kristallogr. Suppl. (2015) 393-398.

[192] M.M. Lozinska, E. Mangano, J.P. Mowat, A.M. Shepherd, R.F. Howe, S.P. Thompson, J.E. Parker, S. Brandani, P.A. Wright, Understanding carbon dioxide adsorption on univalent cation forms of the flexible zeolite Rho at conditions relevant to carbon capture from flue gases, J. Am. Chem. Soc. 134 (2012) 17628-17642.

[193] Y. Guo, T. Sun, Y. Gu, X. Liu, Q. Ke, X. Wei, S. Wang, Rational synthesis of chabazite (CHA) zeolites with controlled Si/Al ratio and their $CO_2/CH_4/N_2$ adsorptive separation performances, Chem. Asian J. 13 (2018) 3222-3230.

[194] C. Wen, L. Geng, L. Han, J. Wang, L. Chang, G. Feng, D. Kong, J. Liu, A comparative first principles study on trivalent ion incorporated SSZ-13 zeolites, Phys. Chem. Chem. Phys. 17 (2015) 29586-29596.

[195] J. Liang, J. Su, Y. Wang, Z.J. Lin, W.J. Mu, H. Zheng, R. Zou, F. Liao, J. Lin, CHA-type zeolites with high boron content: synthesis, structure and selective adsorption properties, Microporous Mesoporous Mater. 194 (2014) 97-105.

[196] G.A. Nasser, O. Muraza, T. Nishitoba, Z. Malaibari, Z.H. Yamani, T.K. Al-Shammari, T. Yokoi, Microwave-assisted hydrothermal synthesis of CHA zeolite for methanol-to-olefins reaction, Ind. Eng. Chem. Res. 58 (2019) 60-68.

[197] K. Itabashi, Y. Kamimura, K. Iyoki, A. Shimojima, T. Okubo, A working hypothesis for broadening framework types of zeolites in seed-assisted synthesis without organic structure-directing agent, J. Am. Chem. Soc. 134 (2012) 11542-11549.

[198] L.V. Sousa, A.O.S. Silva, B.J.B. Silva, C.M. Teixeira, A.P. Arcanjo, R. Frety, J.G.A. Pacheco, Fast synthesis of ZSM-22 zeolite by the seed-assisted method of crystallization with methanol, Microporous Mesoporous Mater. 254 (2017) 192-200.

[199] J. Zhang, X. Liu, M. Li, C. Liu, D. Hu, G. Zeng, Y. Zhang, Y. Sun, Fast synthesis of submicron all-silica CHA zeolite particles using a seeding method, RSC Adv. 5 (2015) 27087-27090.

[200] J.R. Di Iorio, R. Gounder, Controlling the isolation and pairing of auminum in cabazite zolites uing mxtures of oganic and inorganic structure-directing agent, Chem. Mater. 28 (2016) 2236-2247.

[201] Q. Zhu, M. Hinode, T. Yokoi, J.N. Kondo, Y. Kubota, T. Tatsumi, Methanol-to-olefin over gallosilicate analogues of chabazite zeolite, Microporous Mesoporous Mater. 116 (2008) 253-257.

[202] J. Přech, Catalytic performance of advanced titanosilicate selective oxidation catalysts – a review, Catal. Rev. 60 (2018) 71-131.

[203] R. Fricke, H. Kosslick, G. Lischke, M. Richter, Incorporation of gallium into zeolites: Syntheses, properties and catalytic application, Chem. Rev. 100 (2000) 2303-2405.

[204] R. Millini, G. Perego, G. Bellussi, Synthesis and characterization of boron - containing molecular sieves, Top. Catal. 9 (1999) 13-34.

[205] G. Ricchiardi, A. Damin, S. Bordiga, C. Lamberti, G. Spano, F. Rivetti, A. Zecchina, Vibrational structure of titanium silicate catalysts. A spectroscopic and theoretical study, J. Am. Chem. Soc. 123 (2001) 11409-11419.

[206] S. Bordiga, C. Lamberti, F. Bonino, A. Travert, F. Thibault-Starzyk, Probing zeolites by vibrational spectroscopies, Chem. Soc. Rev. 44 (2015) 7262-7341.

[207] J. Datka, Z. Piwowarska, OH Groups in Boralites, J. Chem. Soc., Faraday Trans. 1 85 (1989) 837-841.

[208] M.V. Shamzhy, O.V. Shvets, M.V. Opanasenko, L. Kuřfirtová, D. Kubička, J. Čejka, Extra-large-pore zeolites with UTL topology: control of the catalytic activity by variation in the nature of the active sites, ChemCatChem 5 (2013) 1891-1898.

[209] N. Žilková, M.V. Shamzhy, O.V. Shvets, J. Čejka, Transformation of aromatic hydrocarbons over isomorphously substituted UTL: Comparison with large and medium pore zeolites, Catal. Today 204 (2013) 22-29.

[210] P.E. Escalona, M.M. Peñarroya, C. Morterra, Fourier transform infrared spectroscopy study of $CD_3CN$ adsorbed on pure and doped γ-alumina, Langmuir 15 (1999) 5079-5087.

[211] P. Wu, T. Tatsumi, T. Komatsu, T. Yashima, A novel titanosilicate with MWW structure. I. Hydrothermal synthesis, elimination of extraframework titanium, and characterizations, J. Phys. Chem. B 105 (2001) 2897-2905.

[212] C. Li, G. Xiong, J. Liu, P. Ying, Q. Xin, Z. Feng, Identifying framework titanium in TS-1 zeolite by UV resonance Raman spectroscopy, J. Phys. Chem. B 105 (2001) 2993-2997.

[213] Y. Kunitake, T. Takata, Y. Yamasaki, N. Yamanaka, N. Tsunoji, Y. Takamitsu, M. Sadakane, T. Sano, Synthesis of titanated chabazite with enhanced thermal stability by hydrothermal conversion of titanated faujasite, Microporous Mesoporous Mater. 215 (2015) 58-66.

[214] G. Xiong, Y. Cao, Z. Guo, Q. Jia, F. Tian, L. Liu, The roles of different titanium species in TS-1 zeolite in propylene epoxidation studied by in situ UV Raman spectroscopy, Phys. Chem. Chem. Phys. 18 (2016) 190-196.

[215] J. Yang, Q. Zhao, H. Xu, L. Li, J. Dong, J. Li, Adsorption of $CO_2$, $CH_4$, and $N_2$ on gas diameter grade ion-exchange small pore zeolites, J. Chem. Eng. Data 57 (2012) 3701-3709.

[216] T.D. Pham, Q. Liu, R.F. Lobo, Carbon dioxide and nitrogen adsorption on cation-exchanged SSZ-13 zeolites, Langmuir 29 (2013) 832-839.

[217] T.C. Golden, S. Sircar, Gas adsorption on silicalite, J. Colloid Interface Sci. 162 (1994) 182-188.

[218] R. Bulánek, K. Frolich, E. Frýdová, P. Čičmanec, Study of adsorption sites heterogeneity in zeolites by means of coupled microcalorimetry with volumetry, J. Therm. Anal. Calorim. 105 (2011) 443-449.

[219] L. Feng, Y. Shen, T. Wu, B. Liu, D.K. Zhang, Z. Tang, Adsorption equilibrium isotherms and thermodynamic analysis of $CH_4$, $CO_2$, CO, $N_2$ and $H_2$ on NaY Zeolite, Adsorption 26 (2020) 1101-1111.

[220] T.D. Pham, R.F. Lobo, Adsorption equilibria of $CO_2$ and small hydrocarbons in AEI-, CHA-, STT-, and RRO-type siliceous zeolites, Microporous Mesoporous Mater. 236 (2016) 100-108.

[221] M. Rubeš, M. Trachta, E. Koudelková, R. Bulánek, V. Kasneryk, O. Bludský, Methane adsorption in ADOR zeolites: a combined experimental and DFT/CC study, Phys. Chem. Chem. Phys. 19 (2017) 16533-16540.

[222] L. Grajciar, J. Čejka, A. Zukal, C. Otero Areán, G. Turnes Palomino, P. Nachtigall, Controlling the adsorption enthalpy of $CO_2$ in zeolites by framework topology and composition, ChemSusChem 5 (2012) 2011-2022.

[223] C. Otero Areán, M. Rodríguez Delgado, G. Fiol Bibiloni, O. Bludský, P. Nachtigall, Variable-temperature IR spectroscopic and theoretical studies on $CO_2$ adsorbed in zeolite K-FER, ChemPhysChem 12 (2011) 1435-1443.

[224] A. Pulido, M.R. Delgado, O. Bludský, M. Rubeš, P. Nachtigall, C.O. Areán, Combined DFT/CC and IR spectroscopic studies on carbon dioxide adsorption on the zeolite H-FER, Energy Environ. Sci. 2 (2009) 1187-1195.

[225] C.O. Arean, M.R. Delgado, R. Bulánek, K. Frolich, Combined microcalorimetric and IR spectroscopic study on carbon dioxide adsorption in H-MCM-22, Appl. Surf. Sci. 316 (2014) 532-536.

[226] T. Yamazaki, M. Katoh, S. Ozawa, Y. Ogino, Adsorption of $CO_2$ over univalent cation-exchanged ZSM-5 zeolites, Mol. Phys. 80 (1993) 313-324.

[227] S.K. Wirawan, D. Creaser, CO2 adsorption on silicalite-1 and cation exchanged ZSM-5 zeolites using a step change response method, Microporous Mesoporous Mater. 91 (2006) 196-205.

[228] P. Galhotra, J.G. Navea, S.C. Larsen, V.H. Grassian, Carbon dioxide ($C^{16}O_2$ and $C^{18}O_2$) adsorption in zeolite Y materials: effect of cation, adsorbed water and particle size, Energy Environ. Sci. 2 (2009) 401-409.

[229] T. Montanari, G. Busca, On the mechanism of adsorption and separation of $CO_2$ on LTA zeolites: An IR investigation, Vib. Spectrosc. 46 (2008) 45-51.

[230] J.C. Lavalley, Infrared spectrometric studies of the surface basicity of metal oxides and zeolites using adsorbed probe molecules, Catal. Today 27 (1996) 377-401.

[231] R. Bulánek, K. Frolich, E. Frýdová, P. Čičmanec, Microcalorimetric and FTIR study of the adsorption of carbon dioxide on alkali-metal exchanged FER zeolites, Top. Catal. 53 (2010) 1349-1360.

[232] B. Bonelli, B. Civalleri, B. Fubini, P. Ugliengo, C.O. Areán, E. Garrone, Experimental and quantum chemical studies on the adsorption of carbon dioxide on alkali-metal-exchanged ZSM-5 zeolites, J. Phys. Chem. B 104 (2000) 10978-10988.

[233] M.R. Delgado, C.O. Arean, Carbon monoxide, dinitrogen and carbon dioxide adsorption on zeolite H-Beta: IR spectroscopic and thermodynamic studies, Energy 36 (2011) 5286-5291.

[234] C. Zanzottera, M. Armandi, S. Esposito, E. Garrone, B. Bonelli, $CO_2$ adsorption on aluminosilicate single-walled nanotubes of imogolite type, J. Phys. Chem. C 116 (2012) 20417-20425.

# 7. Appendix I

Table 1 Crystallographic details and Le Bail profile parameters of hydrated M-CHA-h samples (M= Si, B, Al, Ga, and Ti).

| | Si-CHA-h | B-CHA-h | Al-CHA-h | Ga-CHA-h | Ti-CHA-h |
|---|---|---|---|---|---|
| Unit cell formula | $Si_{36}O_{72}$ | $Si_{32.4}B_{3.6}O_{72}$ | $Si_{33.96}Al_{2.05}O_{72}$ | $Si_{34.65}Ga_{1.35}O_{72}$ | $Si_{35.28}Ti_{0.72}O_{72}$ |
| Space group (#) | R-3m (166) | R-3m (166) | R-3m (166) | R-3m (166) | R-3m (166) |
| X-ray source | Cu | Cu | Cu | Cu | Cu |
| Diffractometer | STOE STADI-P | STOE STADI-P | STOE STADI-P | STOE STADI-P | STOE STADI-P |
| Wavelength (Å) | 1.54059 | 1.54059 | 1.54059 | 1.54059 | 1.54059 |
| Temperature (K) | 298 | 298 | 298 | 298 | 298 |
| *a* (Å) | 13.52205(17) | 13.4784(2) | 13.56855(15) | 13.55347(18) | 13.5515(2) |
| *c* (Å) | 14.7325(3) | 14.7272(3) | 14.7635(2) | 14.7553(3) | 14.7539(3) |
| V (Å) | 2332.88(6) | 2317.03(7) | 2353.90(5) | 2347.36(6) | 2346.47(7) |
| $R_p$ | 0.0484 | 0.0679 | 0.0337 | 0.0305 | 0.0693 |
| $R_{wp}$ | 0.0664 | 0.0888 | 0.0455 | 0.0400 | 0.0925 |
| $R_{exp}$ | 0.0488 | 0.0668 | 0.0348 | 0.0344 | 0.0733 |
| $\chi^2$ | 1.856 | 1.766 | 1.715 | 1.357 | 1.594 |

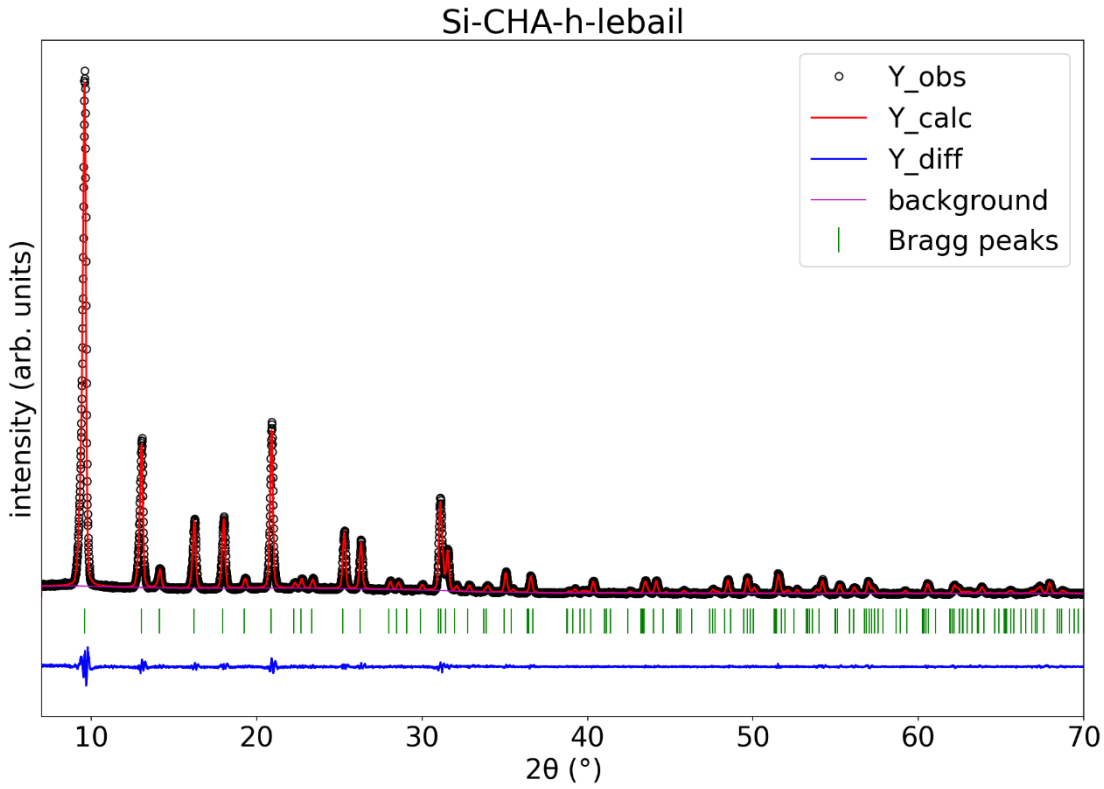

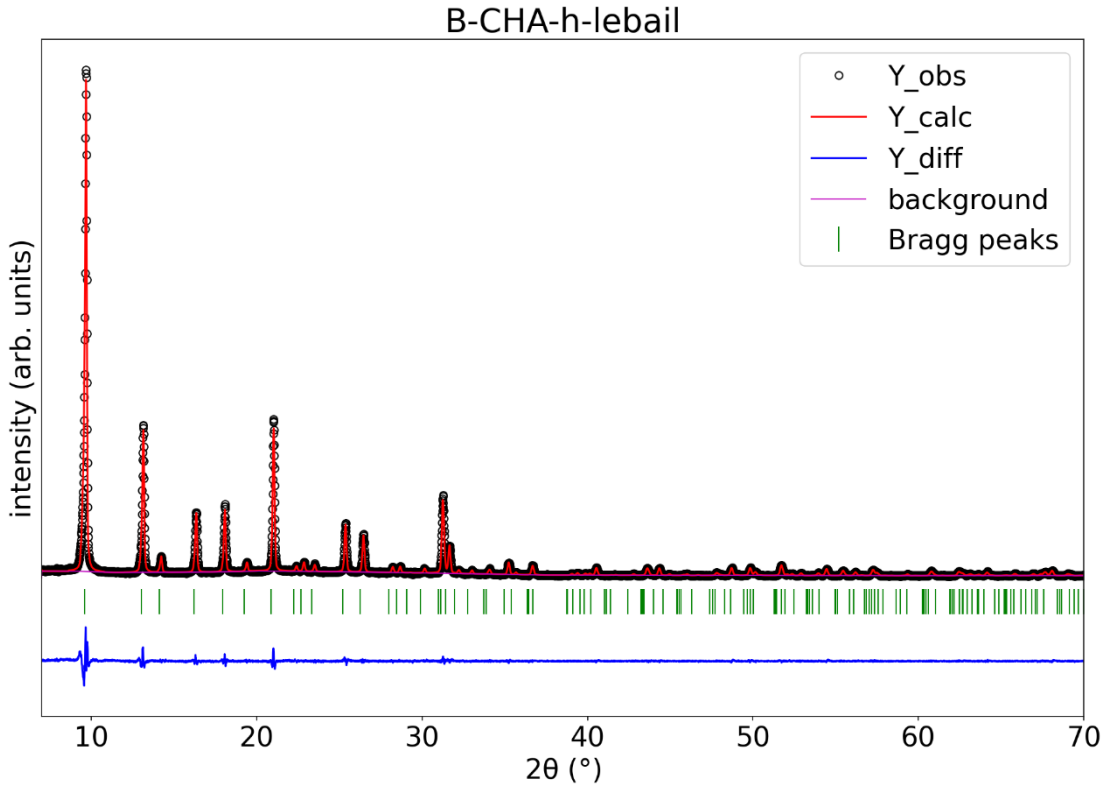
B-CHA-h-lebail
Y_obs
Y_calc
Y_diff
background
Bragg peaks
intensity (arb. units)
10
20
30
40
50
60
70
2θ (°)

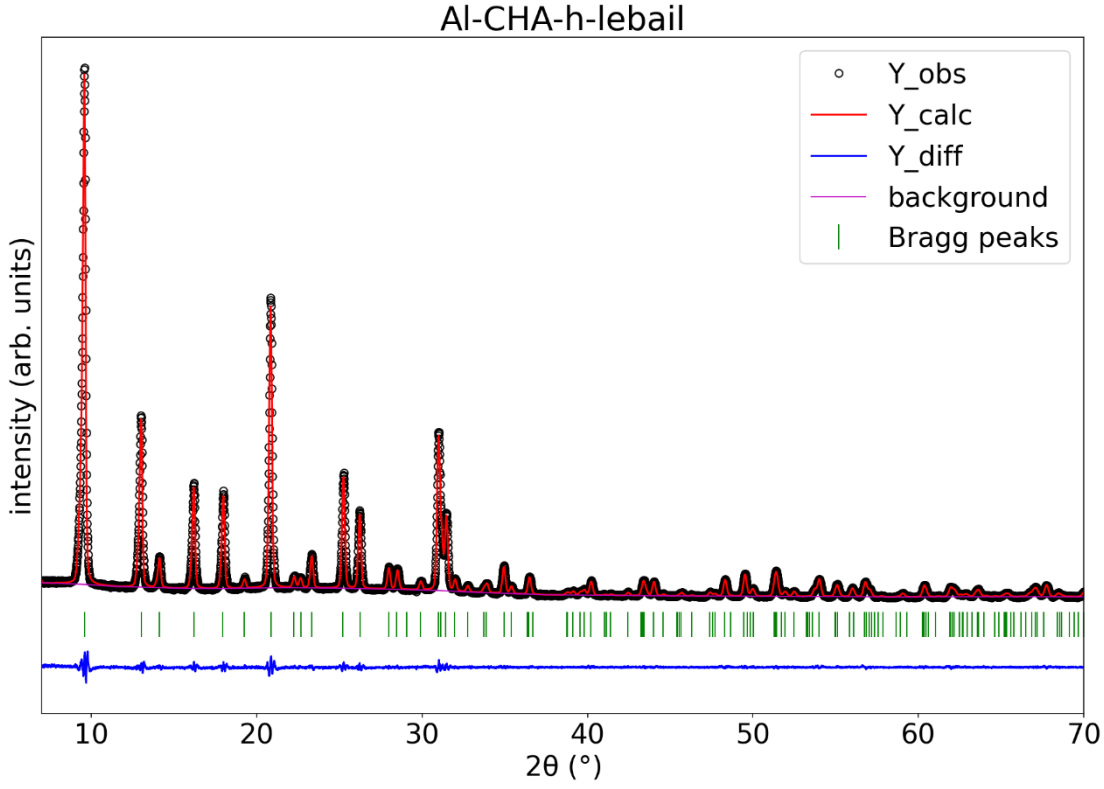
Al-CHA-h-lebail
Y_obs
Y_calc
Y_diff
background
Bragg peaks
intensity (arb. units)
10
20
30
40
50
60
70
2θ (°)

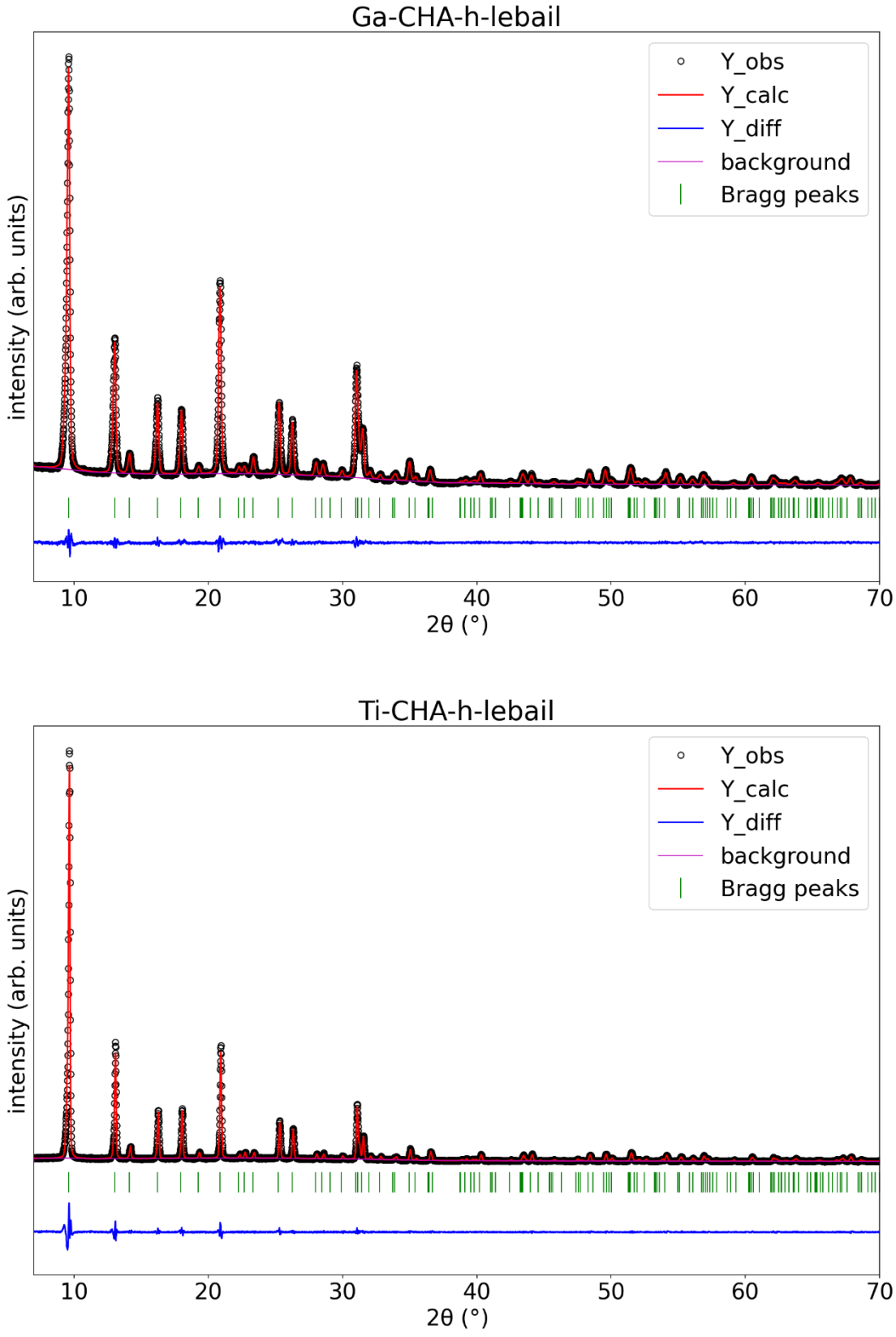


Figure 1 Le Bail refinement plots of M-CHA-h (M = Si, B, Al, Ga, and Ti).

Table 2 Crystallographic details and Rietveld profile parameters of M-CHA-d samples (M= Si, B, Al, Ga, Ti), dehydrated at 573 K under $9\times10^{-4}$ mbar for 24 h.

| | Si-CHA-d | B-CHA-d | Al-CHA-d | Ga-CHA-d | Ti-CHA-d |
|---|---|---|---|---|---|
| Unit cell formula | $Si_{36}O_{72}$ | $Si_{32.4}B_{3.6}O_{72}$ | $Si_{33.96}Al_{2.05}O_{72}$ | $Si_{34.65}Ga_{1.35}O_{72}$ | $Si_{35.28}Ti_{0.72}O_{72}$ |
| Space group (#) | R-3m (166) | R-3m (166) | R-3m (166) | R-3m (166) | R-3m (166) |
| X-ray source | Cu | Cu | Cu | Cu | Cu |
| Diffractometer | STOE STADI-P | STOE STADI-P | STOE STADI-P | STOE STADI-P | STOE STADI-P |
| Wavelength (Å) | 1.54059 | 1.54059 | 1.54059 | 1.54059 | 1.54059 |
| Temperature (K) | 298 | 298 | 298 | 298 | 298 |
| *a* (Å) | 13.54718(17) | 13.4765(2) | 13.57632(18) | 13.5613(2) | 13.54904(18) |
| *c* (Å) | 14.7562(2) | 14.6970(3) | 14.8096(3) | 14.7479(3) | 14.7454(3) |
| V (Å) | 2345.32(6) | 2311.60(7) | 2363.95(6) | 2348.90(7) | 2344.26(6) |
| $R_p$ | 0.0708 | 0.0714 | 0.0411 | 0.0372 | 0.0745 |
| $R_{wp}$ | 0.0890 | 0.0960 | 0.0563 | 0.0492 | 0.0957 |
| $R_{exp}$ | 0.0466 | 0.0466 | 0.0334 | 0.0326 | 0.0455 |
| $\chi^2$ | 3.647 | 4.253 | 2.835 | 2.270 | 4.423 |

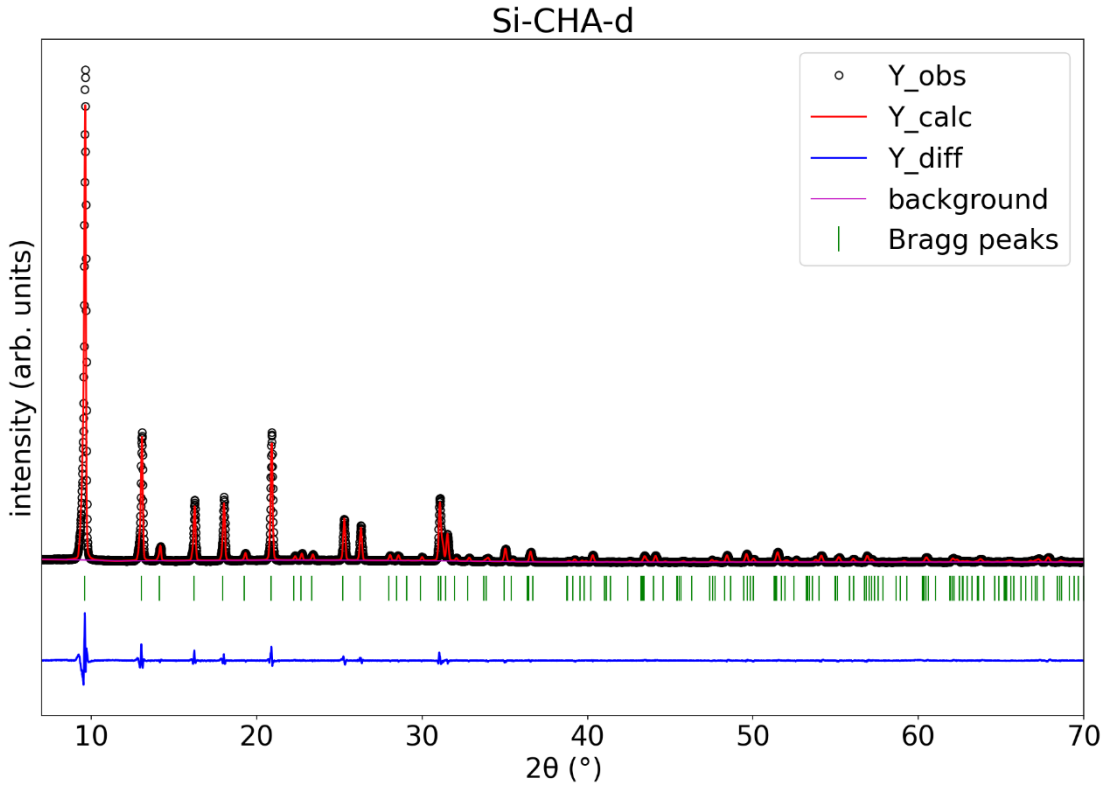

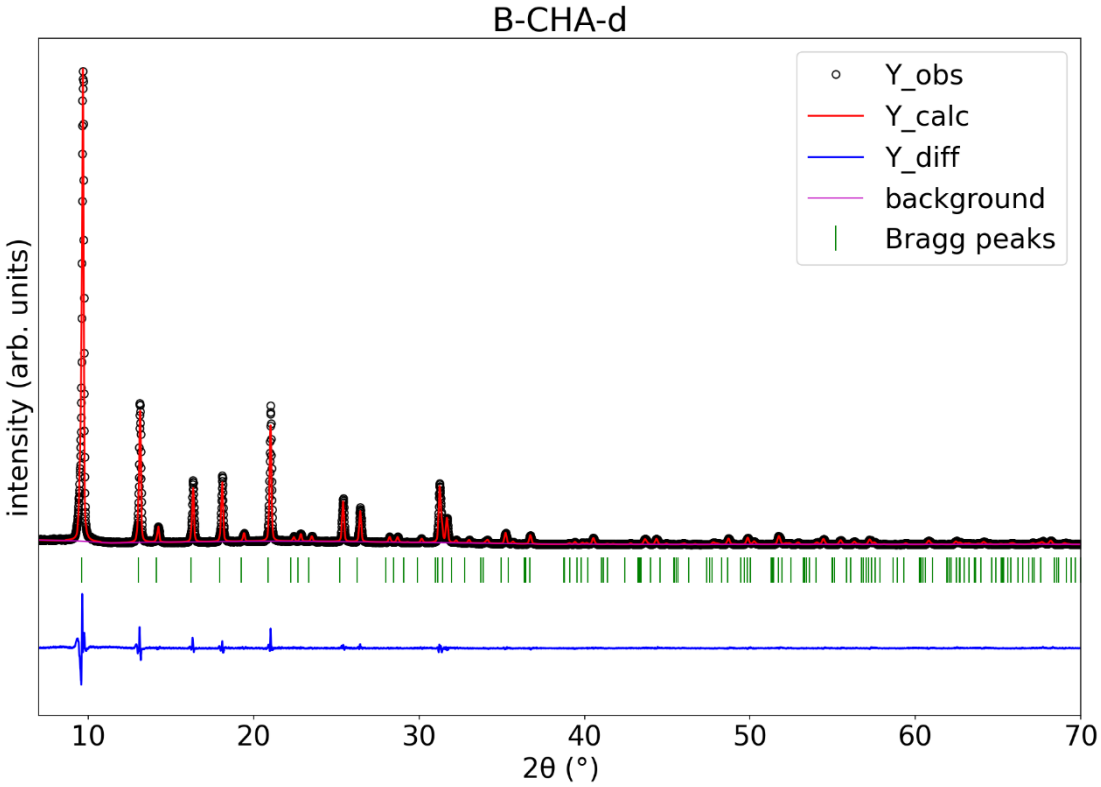
B-CHA-d
Y_obs
Y_calc
Y_diff
background
Bragg peaks
intensity (arb. units)
10
20
30
40
50
60
70
2θ (°)

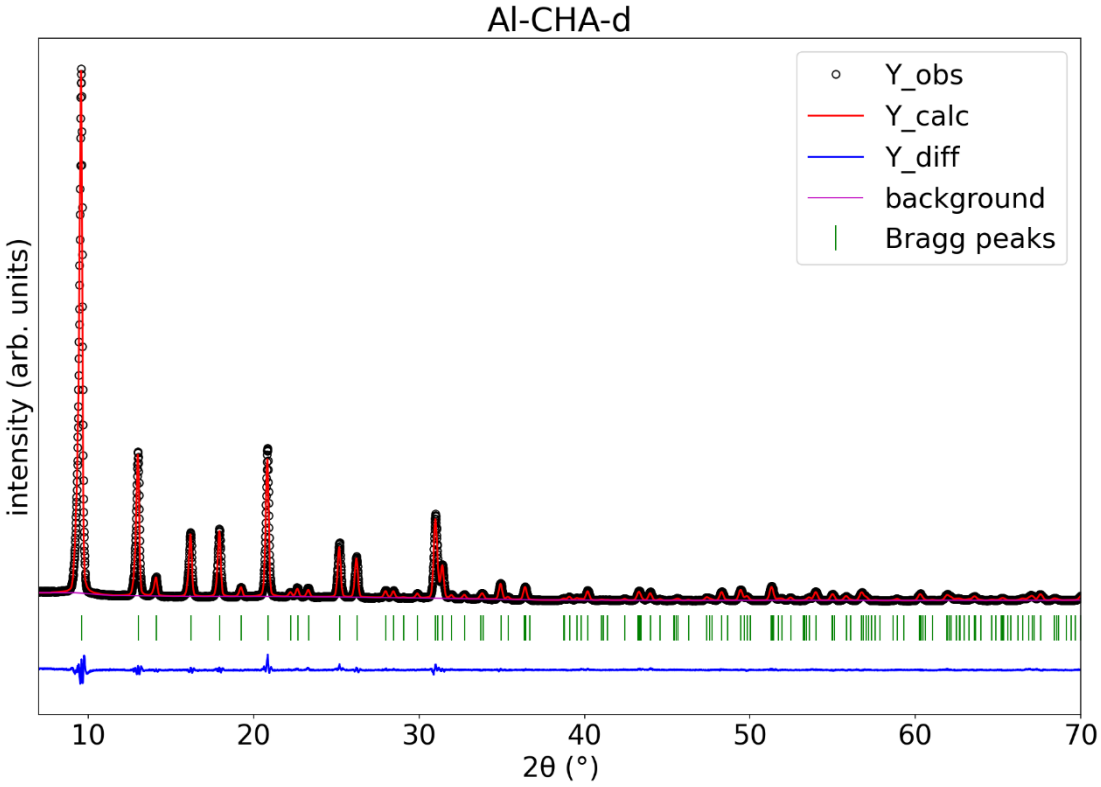
Al-CHA-d
Y_obs
Y_calc
Y_diff
background
Bragg peaks
intensity (arb. units)
10
20
30
40
50
60
70
2θ (°)

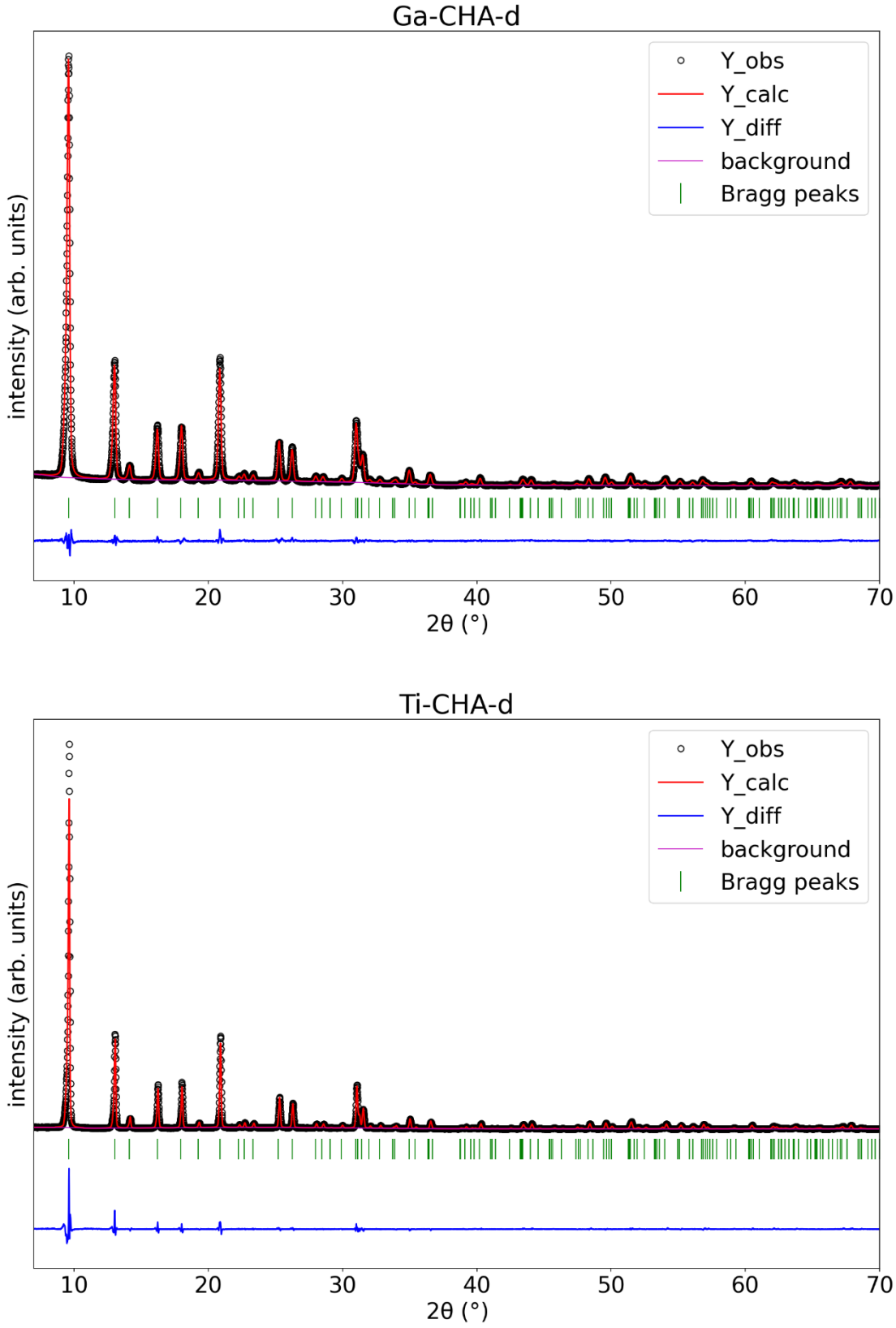


Figure 2 Rietveld plots of M-CHA-d sample (M = Si, B, Al, Ga, and Ti), dehydrated at 573 K under $9\times10^{-4}$ mbar for 24 hours.

Table 3 Fractional atomic coordinates, occupancies, and isotropic displacement parameters of Rietveld refinements of M-CHA-d (M = Si, B, Al, Ga, and Ti) samples, dehydrated at 573 K under $9\times10^{-4}$ mbar for 24 h.

| Si-CHA-d | x | y | z | occ | mult | Uiso |
|---|---|---|---|---|---|---|
| Si1 | 0.10504(16) | 0.43789(14) | 0.06252(10) | 1 | 36 | 0.0165(6) |
| O1 | 0 | 0.3537(3) | 0 | 1 | 18 | 0.0107(9) |
| O2 | 0.0702(3) | 0.4036(3) | 0.166667 | 1 | 18 | 0.0107(9) |
| O3 | 0.1357(3) | 0.56787(17) | 0.0449(3) | 1 | 18 | 0.0107(9) |
| O4 | 0.21297(17) | 0.4259(3) | 0.0345(3) | 1 | 18 | 0.0107(9) |

| B-CHA-d | x | y | z | occ | mult | Uiso |
|---|---|---|---|---|---|---|
| Si1 | 0.1048(2) | 0.4370(2) | 0.06229(15) | 0.9 | 36 | 0.0275(8) |
| B1 | 0.1048(2) | 0.4370(2) | 0.06229(15) | 0.1 | 36 | 0.0275(8) |
| O1 | 0 | 0.3533(4) | 0 | 1 | 18 | 0.0330(13) |
| O2 | 0.0701(4) | 0.4034(4) | 0.166667 | 1 | 18 | 0.0330(13) |
| O3 | 0.1365(4) | 0.5682(2) | 0.0445(4) | 1 | 18 | 0.0330(13) |
| O4 | 0.2121(2) | 0.4242(4) | 0.0345(4) | 1 | 18 | 0.0330(13) |

| Al-CHA-d | x | y | z | occ | mult | Uiso |
|---|---|---|---|---|---|---|
| Si1 | 0.10543(12) | 0.43819(11) | 0.06268(8) | 0.9432 | 36 | 0.0165(4) |
| Al1 | 0.10543(12) | 0.43819(11) | 0.06268(8) | 0.0568 | 36 | 0.0165(4) |
| O1 | 0 | 0.3543(2) | 0 | 1 | 18 | 0.0134(7) |
| O2 | 0.0693(2) | 0.4027(2) | 0.166667 | 1 | 18 | 0.0134(7) |
| O3 | 0.1378(2) | 0.56892(12) | 0.0460(2) | 1 | 18 | 0.0134(7) |
| O4 | 0.21267(12) | 0.4253(2) | 0.0353(2) | 1 | 18 | 0.0134(7) |

| Ga-CHA-d | x | y | z | occ | mult | Uiso |
|---|---|---|---|---|---|---|
| Si1 | 0.10507(13) | 0.43806(12) | 0.06253(8) | 0.9625 | 36 | 0.0319(5) |
| Ga1 | 0.10507(13) | 0.43806(12) | 0.06253(8) | 0.0375 | 36 | 0.0319(5) |
| O1 | 0 | 0.3541(3) | 0 | 1 | 18 | 0.0296(9) |
| O2 | 0.0709(3) | 0.4042(3) | 0.166667 | 1 | 18 | 0.0296(9) |
| O3 | 0.1375(3) | 0.56875(14) | 0.0449(3) | 1 | 18 | 0.0296(9) |
| O4 | 0.21270(14) | 0.4254(3) | 0.0333(2) | 1 | 18 | 0.0296(9) |

| Ti-CHA-d | x | y | z | occ | mult | Uiso |
|---|---|---|---|---|---|---|
| Si1 | 0.10515(17) | 0.43807(15) | 0.06269(11) | 0.9801 | 36 | 0.0173(6) |
| Ti1 | 0.10515(17) | 0.43807(15) | 0.06269(11) | 0.0199 | 36 | 0.0173(6) |
| O1 | 0 | 0.3533(3) | 0 | 1 | 18 | 0.0096(10) |
| O2 | 0.0705(3) | 0.4038(3) | 0.166667 | 1 | 18 | 0.0096(10) |
| O3 | 0.1358(4) | 0.56789(18) | 0.0449(3) | 1 | 18 | 0.0096(10) |
| O4 | 0.21329(18) | 0.4266(4) | 0.0343(3) | 1 | 18 | 0.0096(10) |

Table 4 Bond lengths and angles from Rietveld refinements of M-CHA-d (M = Si, B, Al, Ga, and Ti) samples, dehydrated at 573 K under $9\times10^{-4}$ mbar for 24 h.

| **Bond length [Å]** | **Si-CHA-d** | **B-CHA-d** | **Al-CHA-d** | **Ga-CHA-d** | **Ti-CHA-d** |
|---|---|---|---|---|---|
| T-O1 | 1.5983(19) | 1.585(3) | 1.6053(14) | 1.5983(16) | 1.602(2) |
| T-O2 | 1.6068(18) | 1.602(2) | 1.6149(13) | 1.6036(14) | 1.6028(18) |
| T-O3 | 1.615(3) | 1.619(4) | 1.620(2) | 1.620(3) | 1.614(4) |
| T-O4 | 1.604(4) | 1.593(6) | 1.602(3) | 1.611(4) | 1.604(5) |
| O1-O2 | 2.6013(11) | 2.5904(15) | 2.6059(8) | 2.6027(9) | 2.6011(12) |
| O1-O3 | 2.628(4) | 2.621(5) | 2.646(3) | 2.638(3) | 2.632(4) |
| O1-O4 | 2.592(3) | 2.571(3) | 2.5993(19) | 2.590(2) | 2.593(3) |
| O2-O3 | 2.645(4) | 2.640(6) | 2.656(3) | 2.647(4) | 2.643(5) |
| O2-O4 | 2.655(5) | 2.642(6) | 2.658(3) | 2.664(4) | 2.655(5) |
| O3-O4 | 2.613(6) | 2.609(8) | 2.615(5) | 2.614(5) | 2.608(7) |
| **Bond angle [°]** | | | | | |
| T-O1-T | 148.8(3) | 149.2(4) | 149.5(2) | 149.1(3) | 148.4(3) |
| T-O2-T | 146.1(2) | 146.6(3) | 144.95(16) | 146.56(18) | 146.1(2) |
| T-O3-T | 148.1(3) | 147.6(4) | 147.4(2) | 146.9(2) | 148.2(3) |
| T-O4-T | 148.4(3) | 148.3(4) | 148.7(2) | 147.1(3) | 148.0(3) |
| | | | | | |
| O1-T-O2 | 108.51(14) | 108.7(2) | 108.04(10) | 108.76(12) | 108.51(15) |
| O1-T-O3 | 109.7(2) | 109.8(3) | 110.23(18) | 110.1(2) | 109.8(3) |
| O1-T-O4 | 108.1(2) | 108.0(3) | 108.25(15) | 107.60(17) | 108.0(2) |
| O2-T-O3 | 110.4(3) | 110.1(3) | 110.41(18) | 110.4(2) | 110.5(3) |
| O2-T-O4 | 111.6(3) | 111.6(4) | 111.4(2) | 111.9(2) | 111.8(3) |
| O3-T-O4 | 108.5(2) | 108.6(3) | 108.47(17) | 107.99(19) | 108.3(2) |

Table 5 Fitting parameters from Tóth modelling for single-component adsorption of $CO_2$ and $CH_4$.

| | T[K] | $CO_2$ | | | | $CH_4$ | | | |
|---|---|---|---|---|---|---|---|---|---|
| | | $n_m$[mmol $g^{-1}$] | B[1/torr] | t[-] | $R^2$[-] | $n_m$[mmol $g^{-1}$] | B[1/torr] | t[-] | $R^2$[-] |
| **Si-CHA** | 273 | 5.41 | 0.00179 | 1.260 | 0.99999 | 2.92 | 0.00049 | 1.019 | 0.99999 |
| | 286 | 5.23 | 0.00113 | 1.244 | 0.99999 | 3.33 | 0.00032 | 0.930 | 0.99999 |
| | 298 | 5.63 | 0.00072 | 1.097 | 0.99999 | 3.32 | 0.00024 | 0.903 | 0.99999 |
| **B-CHA** | 273 | 5.82 | 0.00232 | 0.968 | 0.99999 | 3.01 | 0.00056 | 0.982 | 0.99999 |
| | 286 | 5.55 | 0.00146 | 0.984 | 0.99999 | 2.93 | 0.00042 | 0.962 | 0.99999 |
| | 298 | 5.51 | 0.00094 | 0.967 | 0.99999 | 2.55 | 0.00035 | 1.023 | 0.99999 |
| **Al-CHA** | 273 | 14.07 | 0.00458 | 0.417 | 0.99954 | 3.98 | 0.00059 | 0.756 | 0.99999 |
| | 286 | 22.70 | 0.00254 | 0.332 | 0.99981 | 3.66 | 0.00045 | 0.824 | 0.99999 |
| | 298 | 32.64 | 0.00119 | 0.302 | 0.99995 | 2.92 | 0.00042 | 0.877 | 0.99999 |
| **Ga-CHA** | 273 | 7.68 | 0.00216 | 0.795 | 0.99995 | 2.85 | 0.00053 | 1.114 | 0.99999 |
| | 286 | 6.17 | 0.00151 | 0.988 | 0.99999 | 2.64 | 0.00045 | 1.083 | 0.99999 |
| | 298 | 5.76 | 0.00102 | 0.989 | 0.99999 | 2.92 | 0.00032 | 1.028 | 0.99999 |
| **Ti-CHA** | 273 | 4.36 | 0.00142 | 2.820 | 0.99956 | 1.86 | 0.00067 | 1.723 | 0.99995 |
| | 286 | 3.98 | 0.00126 | 2.605 | 0.99973 | 2.04 | 0.00054 | 1.503 | 0.99999 |
| | 298 | 3.47 | 0.00101 | 2.496 | 0.99983 | 2.36 | 0.00037 | 1.277 | 0.99999 |

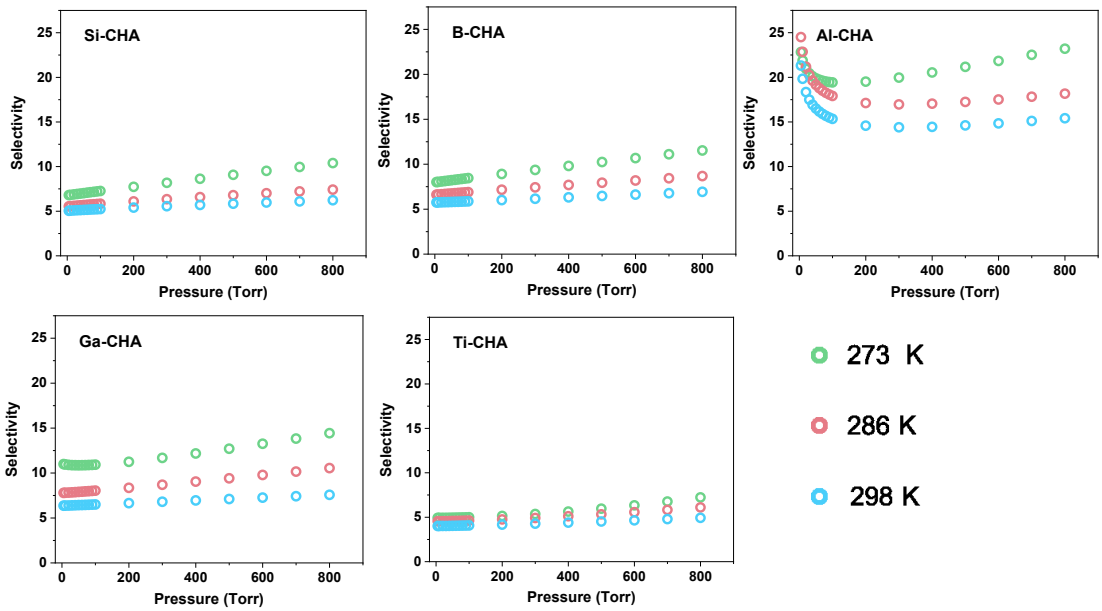


Figure 3 IAST predicted selectivities at 273, 286, and 298 K for M-CHA (M = Si, B, Al, Ga, and Ti).

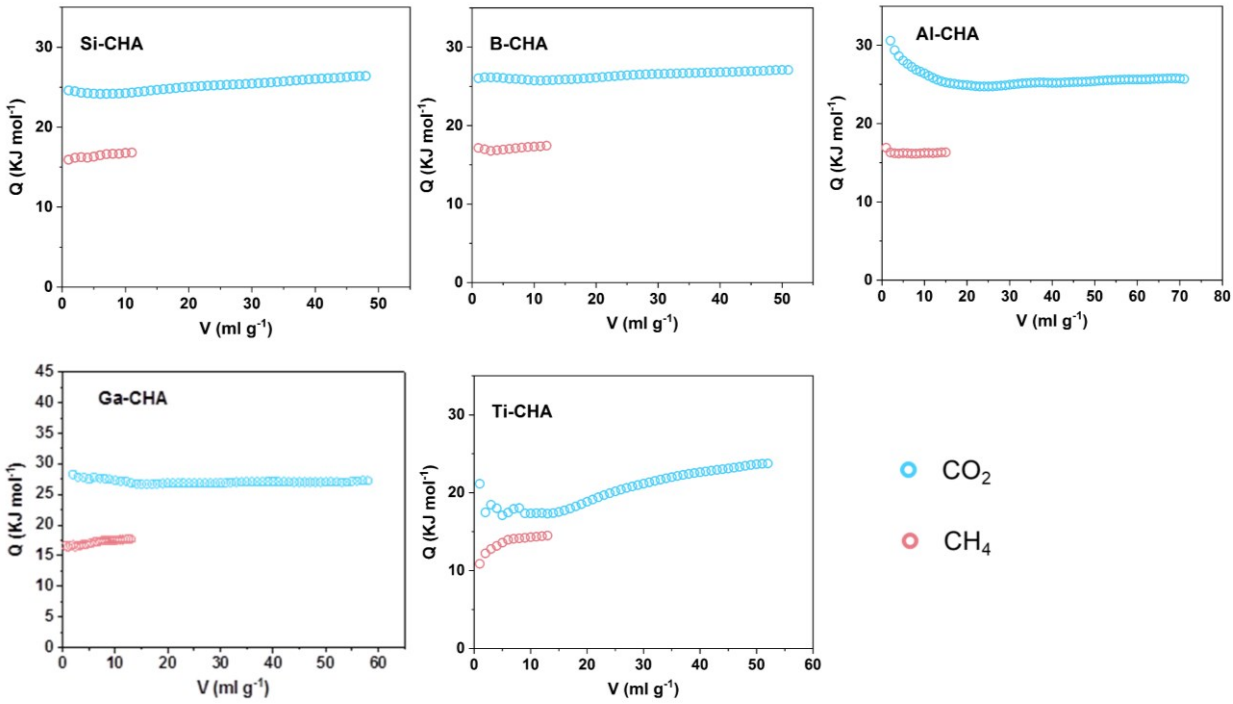


Figure 4 Heats of adsorption of $CO_2$ and $CH_4$ on proton-form Si-CHA, B-CHA, Al-CHA, Ga-CHA, and Ti-CHA.

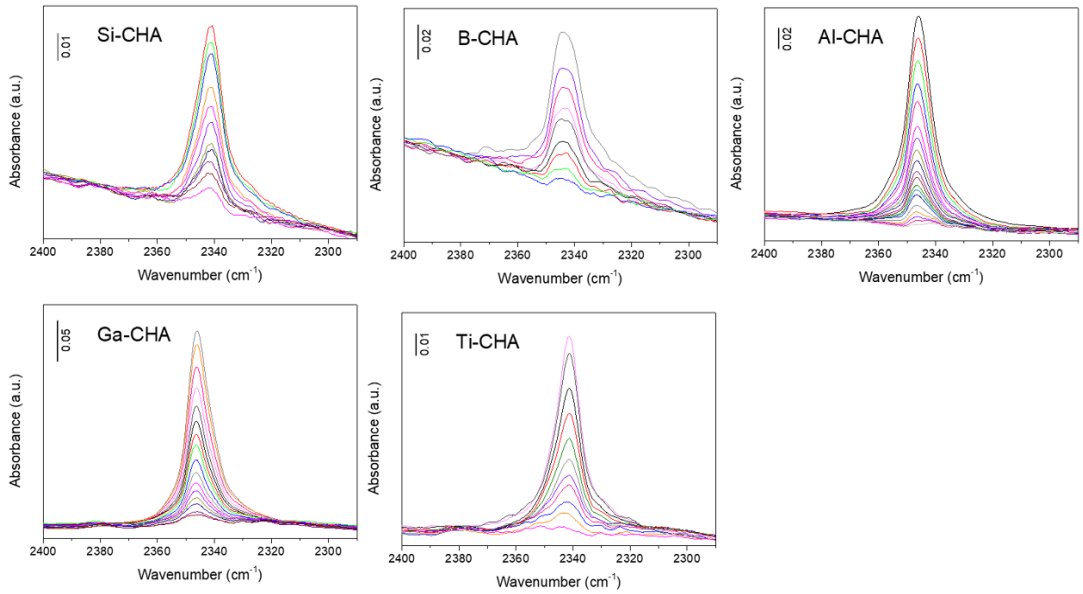


Figure 5 Time-resolved IR spectra of $CO_2$ adsorbed on M-CHA measured during evacuation of the samples at 298 K. Spectra were collected in fast scans in the time period 0 - 6 min.

# 8. Enclosures

1. V. Kasneryk, M. Shamzhy, J. Zhou, **Q. Yue**, M. Mazur, A. Mayoral, Z. Luo*, R. E. Morris, J. Čejka, M. Opanasenko*. Vapour-phase-transport rearrangement technique for the synthesis of new zeolites. **Nat. Commun.** 2019, 10, 5129.
2. **Q. Yue**, J. Zhang, M. Shamzhy, M. Opanasenko*. Seeded growth of isomorphously substituted chabazites in proton-form. **Microporous Mesoporous Mater.** 2019, 280, 331-336.